

Bangor University

DOCTOR OF PHILOSOPHY

A study into the growth kinetics and properties of thin film zinc oxide deposited by MOCVD

Lamb, D. A.

Award date:
2004

Awarding institution:
Bangor University

[Link to publication](#)

General rights

Copyright and moral rights for the publications made accessible in the public portal are retained by the authors and/or other copyright owners and it is a condition of accessing publications that users recognise and abide by the legal requirements associated with these rights.

- Users may download and print one copy of any publication from the public portal for the purpose of private study or research.
- You may not further distribute the material or use it for any profit-making activity or commercial gain
- You may freely distribute the URL identifying the publication in the public portal ?

Take down policy

If you believe that this document breaches copyright please contact us providing details, and we will remove access to the work immediately and investigate your claim.

A Study into the Growth Kinetics and Properties of Thin Film Zinc Oxide Deposited by MOCVD

A thesis submitted to the University of Wales
in candidature for the degree of

Doctor of Philosophy

By

D. A. Lamb

University of Wales Bangor 2004



Contents

<u>Title</u>	<u>Page</u>
Acknowledgements	IV
Summary	V

Chapter One: Introduction

1.1	Background	1
1.2	Aims	1
1.3	Transparent Conducting Electrodes	3
1.4	Properties of a Semiconductor	3
1.5	The Photovoltaic Effect	5
1.6	Thin Film Photovoltaic Cell	7
1.7	Zinc Oxide	8
1.8	MOCVD	10
1.9	Zinc Oxide Precursors	11
1.10	Photoassisted MOCVD	12
1.11	Analysis of Thin Films	13
1.12	Structure of Thesis	15
1.13	References	16

Chapter Two: Literature Review

2.1	Introduction	17
2.2	History of MOCVD	17
2.3	The MOCVD Technique	20
2.4	Precursors	24
2.5	TCOs	25

2.6	Deposition of ZnO by Various Techniques	30
2.7	MOCVD of ZnO	32
2.8	MOCVD of ZnO Using Alcohol Precursors	39
2.9	Alkylzinc Alkoxides	45
2.10	Growth Modes of MOCVD	48
2.11	Photoassisted MOCVD	49
2.12	Photoassisted MOCVD of ZnO	55
2.13	References	61

Chapter Three: Design and Construction of MOCVD System

3.1	Introduction	65
3.2	Designing the MOCVD System	65
3.3	Correcting for Substrate Temperature	72
3.4	Calculating the Precursor Partial Pressures	73
3.5	The UV/Vis Light Source	74
3.6	<i>In situ</i> Interferometry	77
3.7	Data Logging	80
3.8	Experimental Procedures	81
3.9	References	83

Chapter Four: Techniques for Thin Film Analysis

4.1	Introduction	84
4.2	UV/Vis Measurements	84
4.3	Measuring Growth Rate by <i>in situ</i> Interferometry	86
4.4	Using AFM for Thin Film Analysis	91
4.5	Using SEM for Thin Film Analysis	93
4.6	X-ray Diffraction	95
4.7	Electrical Measurements of Thin Films	99
4.8	References	101

Chapter Five: Results and Discussion

5.1	Introduction	102
5.2	Thin Film Profile	102
5.3	Growth Properties and Kinetics	106
5.4	Optical and Electrical Properties	120
5.5	Thin Film Morphology	143
5.6	References	156

Chapter Six: Conclusions

7.1	Introduction	157
7.2	Conclusions	157
7.3	Further Work	159

Appendix

Paper: Growth properties of thin film ZnO deposited by MOCVD with n-butyl alcohol as the oxygen precursor.

Acknowledgements

I would like to thank my supervisor Stuart Irvine for his continuous support and enthusiasm over the course of the PhD. I extend especial thanks to my fiancée Louise without whose help, motivation and encouragement I would have been lost.

My thanks go out to my colleges in the chemistry department for their help especially Steve Jones for his technical assistance, support and motivation, also many thanks to Duarte, Vincent and Andy.

I would also very gratefully like to acknowledge the support of the chemistry department technical staff John Charles, Mike Lewis and the late John Sandbrook. Thanks are extended to the academic staff Dr Kalaji, Dr Holliman and Dr Butler for their advice and recommendations throughout the PhD.

Summary

A study of the deposition of thin film ZnO from diethylzinc (DEZn) and a novel oxygen precursor n-butanol (n-BuOH) has been carried out, using atmospheric metal organic chemical vapour deposition (MOCVD). ZnO thin films have been identified as candidates for transparent conducting oxides (TCOs) for solar cells. The n-BuOH precursor is suggested to be a viable alternative to the more commonly used alcohol t-BuOH having the process-simplifying advantage of being liquid at room temperature. No prereaction was observed using these precursors. The purpose-designed and built MOCVD reactor incorporated *in situ* monitoring of the thin film growth via laser interferometry. Growth rates as high as 0.6 nm/s were achieved at temperatures below 250°C and precursor ratio II/VI = 4. Polycrystalline zinc oxide thin films were deposited at temperatures as low as 67°C.

The II/VI precursor ratio was found to strongly influence the growth rate of the zinc oxide films. A rate equation has been proposed which identifies two rate constants; the first, k_A a slow step that relates to the decomposition of the alkylzinc alkoxide intermediate via a radical mechanism, and the second faster step k_B that occurs under higher than equimolar II/VI ratios. The mechanism proposed in the second step identifies mono-ethylzinc radicals, physisorbed on the surface, as initiators for the decomposition of the alkylzinc alkoxide. It is proposed that when deposition takes place at above equimolar VI/II ratios excess n-BuOH acts as a site blocking molecule lowering the thin film growth rate.

A nucleation delay in film growth was measured via *in situ* interferometry. This delay was found to be independent of temperature but decreased two fold when moving from equimolar partial pressures to zinc rich conditions. A UV/Vis lamp, filtered to exclude gas phase photolysis, was also employed to study the photoassisted deposition of zinc oxide. The photo-energy, supplied to the growing film via a flexible liquid light guide, was selected to promote a surface photocatalytic reaction. An increase in the bandgap energy, compared to non-photoassisted films, was observed when films were deposited at 308°C and 36.8 mW/cm² irradiation.

A rapid change in surface morphology was noted between macro-smooth, below 260°C, to a rough textured film above 260°C. The average transmission in the visible wavelengths for the macro-smooth films was shown to be above 90%. A shift to lower bandgap energies was observed as deposition temperature increased indicating the possibility of a change in stoichiometry within the thin film. From the transmission data, a well-defined and sharp absorption edge was shown to begin at around 360 nm. The films generally displayed high transmission of wavelengths from 360 nm and through the visible spectrum to 900 nm (the limit of the spectrometer). For use in thin film photovoltaics the ZnO films would allow a large range of energy (<3.3 eV) through to the *p-n* junction.

Chapter One: Introduction

1.1 Background

The following study arises from an interest in the use of thin film semiconductors for transparent conducting oxides. Thin film semiconductors play an essential role in today's technology driven climate. The high demand from industry for these thin film semiconductors has lead to a blinkered approach to their production. As long as the required properties are produced there is not the drive for the underlying chemistry of the crystal growth to be thoroughly understood.

Recently, as semiconductor devices ever increase in complexity, the need for a fundamental understanding of the crystal growth process and its direct relationship to the final materials properties has been recognized. This study brings a chemistry perspective to a field dominated by material physics and intends to describe reaction mechanisms and how they relate to the crystal growth process and ultimately the materials physical properties.

1.2. Aims

The aims of this research were; to investigate the deposition properties of thin film zinc oxide, using a novel oxygen precursor and to explore the influence of photoassistance on the growth process. The target application of these deposited zinc oxide films was for use as the front contact for thin film photovoltaic (PV) cells.

The method employed for producing the zinc oxide thin films is the crystal growth technique metal organic chemical vapour deposition (MOCVD). To this end a MOCVD system was designed and constructed specifically to carry out this research. The system incorporated a UV/Vis light source for photoassisted studies and *in situ* laser monitoring giving real-time information on properties of the growing film.

Growth kinetics and materials properties of zinc oxide were studied using a novel oxygen precursor n-butanol. Further to this a photoassisted deposition technique, not reported in the literature for zinc oxide, was employed specifically to promote surface reactions.

This chapter sets out to provide a background to the research undertaken; briefly describing the field of study, the choice of material, the technique employed and the methods of thin film analysis carried out.

1.3 Transparent Conducting Electrodes

A semiconductor is described as an element or compound having higher resistivity than a conductor, but lower resistivity than an insulator. Many metal oxides display these semiconducting characteristics and when deposited as thin films have the added material property of optical transparency. These thin films are known as Transparent conducting oxides (TCOs) and their electrical and optical properties can be engineered to suit various device applications.

TCOs have found a number of applications in today's high technology climate from heated windows and invisible antennas to flat panel displays. The TCO application considered for this research is as a front contact for thin film photovoltaics. The criteria when depositing a TCO for use as a front contact for photovoltaics is that it be highly transparent in the wavelength range absorbed by the PV cell, and that it efficiently conducts the photocurrent produced. Currently, tin doped indium oxide is the favoured TCO for this application as it offers high transparency, greater than 90 % in the visible wavelength region, and has a low sheet resistance of about $6 \Omega/\square$.

The two leading markets for TCOs are in architectural applications and flat panel displays (FPDs). Fluorine doped tin oxide is used as a coating on windows to prevent radiative heat loss in cold or moderate climates. Tin oxide is used for PV

cells, touch screens and plasma displays. However, it is tin doped indium oxide (ITO) that is most often used for FPD and PV applications.

There are a number of reasons why a competitive alternative to ITO for PV cells is necessary; it is essential to drive down the production costs in order to compete with more traditional fossil-fuel based energy sources. Also as the PV cells themselves increase in efficiency, the role of the TCO in transmitting the light and conducting current away, becomes a determining factor for the output of the cell.

The TCO must also be thought of as the superstrate, acting as a template, for the deposition of the photovoltaic producing material. To this end the effects the crystalline structure and surface morphology of the TCO have on subsequently deposited layers are important factors when designing a PV cell.

1.4 Properties of a Semiconductor

The electrical properties of semiconductors arise from the covalent nature of the bonds in which the atoms are held together within the crystal. At low temperatures the individual atom's electrons cannot move through the solid crystal. As the temperature is increased and, under the influence of an applied electric field, some valence electrons gain enough energy to escape the covalent bonds. These are known as 'free' electrons and are responsible for the *n*-type (negative charge) conducting nature of a semiconductor.

For every free electron created a 'hole' is left behind. These holes also contribute to the conductivity of the semiconductor. An electron may move from one bond to occupy the hole in an adjacent bond, itself leaving a hole behind. This hole is filled by another electron and thus a positive hole can be seen to be moving in the opposite direction of the current. These holes are responsible for the *p*-type (positive charge) conducting nature of a semiconductor. This type of semiconductor is known as an intrinsic semiconductor.

Further to the intrinsic semiconductor there is the extrinsic semiconductor. The semiconductivity in these materials arises from the presence of small amounts of impurities. Controlled amounts of these impurities are often added to a material, to enhance certain electrical properties, in a process known as doping. Donor impurities are atoms that will replace a native atom, occupying its site in the crystal lattice. These donor atoms contain an extra electron to the native atom they replace.

The extra electron is weakly bound and can easily be ionised, forming a positive ion, the electron is then released into the conduction band. The remaining electrons of the positive ion are strongly bound, so hole (*p*-type) conductivity does not occur.

In this case the main part of the current is carried by electrons, known as the majority carriers, and the remainder of the current is transported by holes known as minority carriers. The opposing situation is one where the impurity atom requires an extra electron, to the native atom it replaces, to form a bond within the crystal lattice. The ionisation of the acceptor produces positive holes, which can carry current. In this case the majority carriers would be holes and the minority carriers' electrons.

As well as by the type and concentration of carriers within the ZnO their freedom to move unimpeded also governs the level of resistivity of the material. An electron in a perfect crystal lattice at 0 K may move freely without being deflected. This would imply that the material had zero resistance. However the idea of a perfect crystal lattice is far from reality. Any imperfections in the crystal lattice will cause electrons to be deflected or scattered consequently an imperfect crystal will have non-zero resistance.

There are effectively three different types of imperfection which produce scattering and hence give rise to electrical resistance. Firstly, ions in a crystal lattice cannot be thought of as occupying a stationary position. These ions are in a state of continuous thermal vibration about their equilibrium positions. Therefore at any

moment in time the ions do not occupy the sites of the perfect lattice and will give rise to electrical resistance.

Secondly, the presence of impurities incorporated within the crystal lattice gives rise to the scattering of conduction electrons. The effects of these impurity ions are greater if they are significantly larger or smaller, or if they have a different valence, to the native ions.

Thirdly, any imperfections within the crystal lattice will act to scatter electrons. When considering a missing native atom (vacancy), the conduction electron is free to alter its direction at these vacancies; if the atoms in the lattice are thought of as containing the path of the electron. An extra native atom (interstitial) in the lattice will also act to increase scattering of the conduction electrons.

Grain boundaries are another important factor giving rise to electrical resistance in polycrystalline thin films. The grain boundary is a zone formed at the junction between single crystals in a polycrystalline material. Impurities, increasing resistance, tend to accumulate at the grain boundary by being excluded from the normal growth of each crystal.

The grain boundary is also an area of dangling bonds; in order for one crystallite to end and another begin, it is necessary for the atoms at the edges to have unpaired electrons known as dangling bonds. Electron or hole charge carriers may be trapped by dangling bonds and cannot take any further part in electrical conduction. This effect is known as recombination; the neutralisation of free electron and hole current carriers.

1.5 The Photovoltaic Effect

When designing a TCO layer for a photovoltaic device it is important to understand the role it plays within that device. The photovoltaic effect can be described as the production of a voltage between two layers of different materials when the surface is irradiated by light or other electromagnetic radiation. The p - n junction in the

solar cell is formed when a *p*-type material is placed in contact with an *n*-type material resulting in a discontinuity in electron concentration.

The Fermi energies (E_F) of the two materials are different, in an *n*-type semiconductor the Fermi energy is near to the conduction band edge, whereas in a *p*-type material it is close to the valence band edge. Figure 1.5.1. is a schematic of the *p-n* junction.

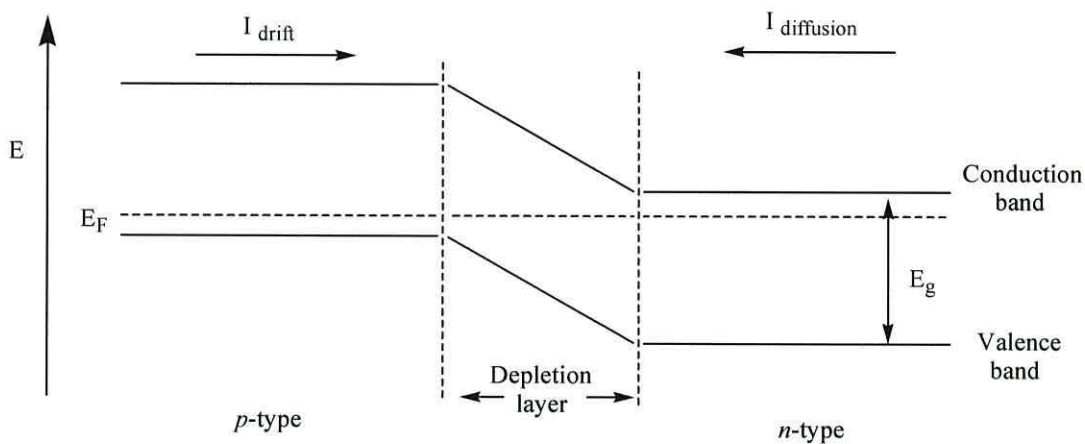


Fig 1.5.1. The distribution of charge at a *p-n* junction produces a contact potential across the junction so that the conduction band edge on the *p*-type side of the junction is at higher energy than that on the *n*-type side. After R. Turton [1].

Initially when the two layers are placed in contact with each other virtually all of the conduction electrons are on one side of the junction and most of the holes are on the other side. This imbalance does not last for long as the conduction electrons move about at random; some of them diffuse into the *p*-type material as some of the holes diffuse into the *n*-type material until a state of equilibrium is reached. The process is further complicated in that some of the electrons and holes can recombine with each other.

When the photovoltaic cell is in the dark the diffusion of electrons from *n*-type to *p*-type (diffusion current) is in equilibrium with the electrons moving from *p*-type to *n*-type (drift current). The process of photoconductivity relies on the fact that a photon of wavelength equal to or greater than the band gap energy (E_g) of the *p*-

type layer can be used to excite an electron from the valence band into the conduction band of this layer.

Once promoted to the conduction band the electron becomes a minority carrier and is attracted across to the *n*-type region by the strong electric field in the depletion layer thus contributing to the drift current. The drift current is now greater than the diffusion current and there is a net flow of electrons from *p*-type to *n*-type the magnitude of which is proportional to the intensity of the light. This arrangement converts light energy into electrical current and is the basis for the solar cell.

1.6 Thin Film Photovoltaic Cell

In the case of a thin film cell, the different layers are *p*-type and *n*-type semiconductors which, when in contact form a *p-n* junction, the source of the photocurrent. Using the CdTe/CdS cell as an example the CdS, known as the window layer, is doped *n*-type with chlorine atoms, which have an extra valence electron, compared to the sulphur. When Cl is substituted into the CdS lattice the increased conductivity is related to extra electrons entering the conduction band.

The CdTe, known as the absorber layer, is doped *p*-type with As, the arsenic atoms have one less valence electron compared to the tellurium and when substituted into the CdTe lattice the conductivity is related to the number of positive holes created. A typical CdTe/CdS solar cell is shown in figure 1.6.1.

The solar cell is produced on a glass substrate whose qualities depend on the environment the solar cell is to be used in. Typically around 2-4mm thick the glass substrate provides the entire device's mechanical strength and protects the active layers from the environment. The glass is effectively the substrate onto which the front contact TCO and further layers are deposited. Finally a gold or aluminum layer of a few tens of nanometers in thickness is added to the cell to provide the back contact.

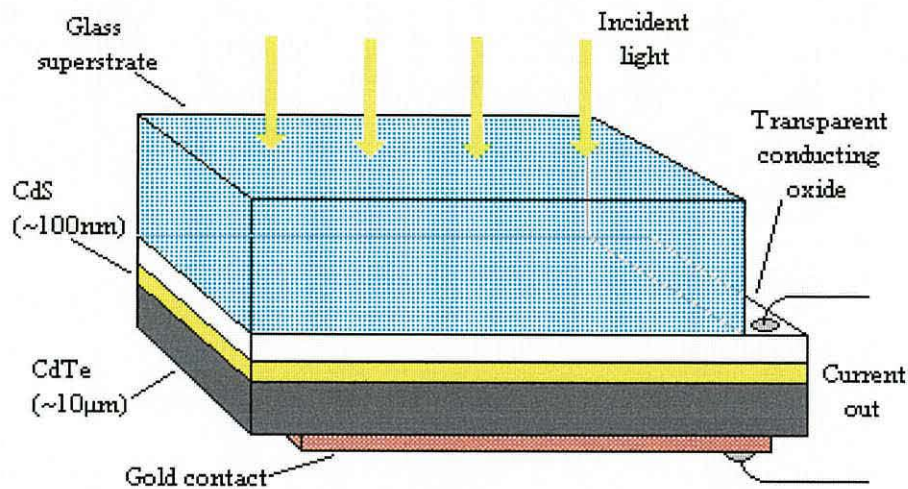


Figure 1.6.1. Example Of CdTe/CdS Thin Film Solar Cell [2]

1.7 Zinc Oxide

Zinc oxide, its archaic name being philosophers' wool, occurs naturally as the reddish orange ore zincite. It is synthesized by oxidizing zinc in hot air and, when cold, is a white powder turning yellow when heated. The powder form has many and varied uses from the paint pigment known as Chinese white to an astringent in creams and ointments.

The world consumption of zinc oxide can be divided up as follows; an activator for vulcanization (36%), flux in ceramics (26%), chemical industry (20%), a trace element in animal feed (12%), paint pigment (3%) and finally 3% in the electronics industry. It is the electronics industry which takes advantage of zinc oxides semiconductor properties.

Zinc oxide can be considered as an old semiconductor as it has received research attention for a long time due to its applications in areas such as gas sensors, piezoelectric transducers, varistors and optical waveguides. Thin film zinc oxide is Wurtzite in structure; films commonly being oriented with the *c*-axis perpendicular to the substrate due to this being the lowest surface free energy for (0002) plane.

The main properties of zinc oxide that make it such a versatile material are its wide and direct band gap of 3.37 eV at RT; a large exciton binding energy of 60 meV (compared to GaN 30 meV); a distinctive combination of optical, electrical, thermal and piezoelectric properties.

Research into single crystal zinc oxide has mainly been driven by the hope that it can out perform GaN for devices such as blue light emitting diodes (LEDs). To this end, high quality zinc oxide substrates can be used for homoepitaxy and, considering the small lattice mismatch (<1.8%) with GaN, as substrates for high quality GaN. *p*-doping has proven to be the major technical difficulty needed to be overcome for zinc oxide to take its place as a leading optoelectronic material.

The specific properties of thin film zinc oxide that make it so attractive a candidate for TCOs are its wide band gap which effectively makes it transparent to wavelengths as short as 400 nm and its almost exclusive *n*-type conductivity. This conductivity is easily enhanced by extrinsic doping; replacing zinc or oxygen atoms with electron donors such as aluminium or fluorine respectively.

Zinc oxide has a high melting point (1975 °C) which indicates that it is a very stable compound which is important, one for its device lifetime and, more critically, that further semiconductor layers deposited onto it at much higher growth temperatures must not affect its TCO characteristics.

Zinc oxide has been used as a TCO for thin film photovoltaics and is the choice for the Cu(InGa)Se₂ (CIGS) system where it also acts as the window layer. The selected technique for the deposition of the zinc oxide thin film was metal organic chemical vapor deposition (MOCVD) and to this aim an experimental apparatus was designed and built specifically for this research.

1.8 MOCVD

There are a number of methods used to form thin films, these include electrochemical deposition, r.f. magnetron sputtering, spray pyrolysis and molecular beam epitaxy (MBE). These techniques all have their strengths and weaknesses for example MBE does not require very volatile reactants and can produce thin films of nanometer layers but would be too expensive a technique for mass producing TCOs for commercial applications. CVD on the other hand is a relatively simple and low cost method that can produce very good quality thin films on a large scale, as demonstrated by the coating of float glass with ITO by Pilkington Glass. It is for these reasons that the variant of CVD, where organometallics are used for the metal precursors, MOCVD has been chosen as the technique of deposition for this research.

MOCVD systems are designed to precisely control the concentrations of all of the species in the reaction zone and provide uniform deposition characteristics. Electronic mass flow controllers regulate the concentration of gaseous precursors. The metalorganics, which are generally liquids, are transported by bubbling an inert carrier gas such as nitrogen through an especially designed container called a bubbler. Adjusting the flow rate of the carrier gas and maintaining steady temperature and pressure controls the precursor concentrations. Abrupt changes in composition and dopant concentration can be achieved by the use of a vent-run manifold, which can quickly direct the precursors either into the reactor for growth (run) or the exhaust (vent).

Semiconductor films grown by MOCVD are the basis of many modern devices from light emitting diodes to solar cells. MOCVD owes its beginnings to two gentlemen of the 19th century who demonstrated the possibility of vapor transport of metals using organic compounds. The first was Edward Frankland who in 1849 discovered organometallic compounds. He was studying methyl and ethyl radical groups and hoped to isolate the ethyl group by treating ethyl iodide with Zinc. However when he heated the Zinc with the organic compound, ethyl iodide, he

produced a foul smelling liquid that readily formed a vapor and caught fire. The compound was diethylzinc.

The second development leading to MOCVD was demonstrated by Mond and Langer who found that crude nickel could easily be purified by heating it at 50 °C in carbon monoxide to form nickel carbonyl and then transporting and decomposing it at a 100 °C. The foundations for using organometallic vapors to transport metals to a reaction zone had been laid.

It was not until the 1960s that MOCVD really began to be developed as a technique for depositing semiconductors. The main protagonist for this technique was Manasevit [3] who showed that MOCVD was applicable to deposition of III-V compounds. In 1968 he deposited gallium arsenide on sapphire substrates. This was the impetus for the growth of MOCVD of III-VI materials. The first manufactured product was probably the photocathode in the early eighties and now MOCVD is the choice technique for a whole host of devices including visible laser, IR laser and high brightness LEDs. The commercial reactors of today are designed to produce many uniform and reproducible wafers and are run 24 hours a day to keep up with demand from the semiconductor industry.

1.9 Zinc Oxide Precursors

In this research, zinc oxide was deposited from the common MOCVD zinc precursor diethylzinc (DEZn) and a novel oxygen source n-butyl alcohol. The main reasons for which precursors are selected for the MOCVD of zinc oxide have been their cost, purity, safety and ease of synthesis. The deposition of zinc oxide suffers from one main problem, a premature reaction in which a white powder ZnO is formed on first contact of the precursors in the gas phase. This white powder pollutes the reactor upstream of the reaction zone blocking inlets and coating reactor walls. The precursors are mostly consumed before reaching the reaction zone reducing the efficiency of the process.

Solutions have been sought to overcome this pre-reaction including mixing the precursors just before the reaction zone, using single source precursors and using less reactive oxygen sources. The latter solution involves the use of precursors such as heterocyclic oxygen sources, N_2O , NO , CO_2 and alcohols, mainly t -BuOH and i -PrOH. Of these, alcohol sources are the most promising showing little or no pre-reaction along with competitive growth rates and good crystalline structure, t -BuOH being favored over i -PrOH.

For this research an alcohol oxygen precursor was used, the obvious choice would have been the well documented t -BuOH; however its melting point of $25^\circ C$ would have required the heating of the bubbler and lines to allow its transport as a vapor to the reaction zone. This fact lead to the investigation for this research, of a novel alcohol precursor, an isomer of t -BuOH; n -BuOH. n -BuOH, a liquid at room temperature, could reasonably be expected to behave similarly to t -BuOH.

1.10 Photoassisted MOCVD

Photoassisted growth of zinc oxide will be examined by irradiating the growing material with a light source of greater energy than the materials band gap ($\lambda < 360nm$). In MOCVD volatile precursors are mixed in a reactor at a suitable temperature and the solid product crystallizes out. The deposition temperature for different compound semiconductors varies dramatically. This fact on its own is not a problem as reactors can be dedicated to producing just one semiconductor compound. However a lower thin film growth temperature would be beneficial for depositing onto low melting point substrates such as plastics.

More importantly, for manufactured devices which usually consist of multiple layers of different semiconductors deposited onto one another, the deposition temperature of one can affect the properties of the other. Low temperature growth tends to give low growth rates and poor crystallinity in thin films. The photoassisted approach allows the thermal energy supplied to the substrate to be reduced whilst maintaining the required properties of the film. Photoassisted

growth has the added benefit of allowing selective area growth where growth only occurs where the surface is irradiated.

Photoassisted growth in MOCVD can follow a number of routes; the photons can be absorbed by the precursors in the gas phase leading to photolysis, the photons can act as a heat source as in photothermal-assisted crystal growth and finally the photons can catalyze the growth at the thin film surface. For this research into ZnO thin films the MOCVD process will be subject to photostimulation designed to promote a surface catalytic reaction. In order to avoid a gas phase reaction the absorption spectrum of the zinc and oxygen precursor must be studied and absorbing wavelengths filtered out from the UV light source.

Surface photocatalysed growth depends upon an initial absorbing layer of the material to be grown via pyrolytic growth. This layer will then absorb photons of energy higher than its band gap. On absorption of these photons an electron hole/pair is created. Diffusion of charge to the surface of the material then catalyses desorption of the organic products, depending on whether oxidation or reduction is required a hole or electron takes part.

This technique has been shown to give the following advantages; the growth temperature can be significantly reduced, selective area growth can be achieved, the materials properties such as dopant incorporation and conductivity can be enhanced, the substrate temperature and precursor dissociation can be controlled and the deposition rate can be increased. Disadvantages of photoassisted growth are that the process of deposition becomes more complex and there is relatively little knowledge of the fundamental mechanisms.

1.11 Analysis of Thin Films

In situ interferometry will be used to monitor the deposition process in real time giving information on growth rate, roughening and film absorption. *In situ* monitoring of thin films is currently a hot topic of research in itself. In the early

days of thin film growth it was accepted that the process was one in which, the experimental parameters were set, the deposition carried out and material properties such as growth rate calculated *ex situ*.

The ability to monitor the deposition process in real-time allows the cause and affect of manipulating experimental parameters to be investigated. Growth rate is shown, by *in situ* monitoring, not to be a constant throughout deposition, although the *ex situ* method of dividing film thickness by growth run duration would ignore this.

On a research level *in-situ* monitoring can reveal important information about reaction kinetics observing nucleation times, changing deposition rates, surface roughening and absorption. From a commercial aspect *in situ* monitoring makes the deposition process more efficient by the early identification of problems in a particular growth run. It is used to precisely control the thickness of the films grown allowing multiple layered devices to be built-up.

Many systems have been successfully employed such as reflectance anisotropy spectroscopy (RAS), spectroscopic ellipsometry, reflectance high electron energy diffraction (RHEED) and laser reflectance.

In the case of *in situ* laser reflectance, a single wavelength laser is reflected by the substrate surface and the signal then collected by a photodetector. Any transparent film deposited on the substrate will itself reflect a certain amount of the laser light; this secondary signal will then interfere with the substrates reflection via a destructive or constructive method depending on the distance, giving rise to an interferogram. Information about the film thickness and growth rate as well as the film roughening and optical properties, such as the refractive index and absorption coefficient can be gained from this interferogram.

This *in-situ* monitoring along with *ex-situ* techniques such as X-ray diffraction (XRD), scanning electron microscopy (SEM) and atomic force microscopy (AFM), was used attempting to elucidate the growth kinetics of the zinc oxide thin film. It is this understanding of how changes in experimental parameters affect the properties of the thin film that will enable the optimization of TCO characteristics. Some of the areas to be investigated during this research are for example; the affects of deposition temperature, II/VI ratio and the influence of photocatalytic stimulation on TCO properties such as growth rate, percentage transmission, conductivity, crystallinity and surface morphology.

1.12 Structure of Thesis

Chapter two provides a survey of the relevant current and historical literature in the field of MOCVD thin films and their application as TCOs. The history of the chosen crystal growth technique is described along with the role the technique plays in semiconductor production and the importance of precursor chemistry. The literature on photoassisted thin film semiconductors is presented along with specific cases of photoassisted zinc oxide deposition and how these differ from the method carried out within this research.

Chapter three describes the design and construction of the experimental equipment carried out to produce a fully functioning thin film deposition system. The reasoning behind the various choices in specification is explained including considerations in choosing a light source for the photoassisted experiments and the setup of the *in situ* laser reflectance.

Chapter four describes the analytical techniques carried out on the thin films deposited during the research. The methodology of measuring the optical, electrical, morphological and crystalline properties of the thin films is given.

Chapter five presents the results from series of experiments carried out on the purpose built MOCVD system. The optical and electrical properties of the films are shown followed by the surface morphology and crystallinity results as given by

AFM, SEM and XRD. Chapter six sets out a detailed discussion of the results presented in chapter five. A comparison of the results with those of similar studies from the literature is made. Chapter seven offers conclusions and further research.

1.13 References

- [1] R. Turton, The Physics of Solids, Oxford University Press, (2000) 154.
- [2] Image with kind permission of P. Edwards, <http://www.dur.ac.uk/~dph0www5/solar.html>, University of Durham website (accessed 06/03/2001).
- [3] H. M. Manasevit, J. Cryst. Growth **55** (1981) 1-9

Chapter Two: Literature Review

2.1 Introduction

This chapter provides a survey of the relevant current and historical literature in the field of MOCVD thin films and their application as TCOs. The history of the chosen crystal growth technique is described along with the role the technique plays in semiconductor production and the importance of precursor design.

More specifically the MOCVD literature of zinc oxide, the use of alcohol precursors with alkylzinc and the relevant chemistry is discussed. Finally the literature on photoassisted thin film growth is presented.

2.2 History of MOCVD

MOCVD was born out of a desire to find a crystal growth technique that could deposit gallium arsenide (GaAs) on single crystal insulators. The MOCVD process developed in the early sixties through a type of parallel evolution. H. M. Manasevit, who is widely thought of as the father of MOCVD, states in his paper, "Recollections and Reflections of MOCVD" [1]; he had recalled from his PhD thesis work on Lewis acid properties of trimethylgallium (TMGa) (acceptor) with selected silylamines (donors of electrons through the N atom) and wondered if this knowledge could be applied to the reaction shown in figure 2.2.1.



Fig. 2.2.1. The reaction between trimethylgallium and arsine.

By parallel evolution it is meant that there were three laboratories working on the MOCVD technique without knowledge of each others work. Harrison and Tompkins [2] were studying the GaAs reaction under low pressure conditions and Didchenko *et al.* [3] prepared indium phosphide (InP) from trimethylindium (TMIn) and phosphine (PH₃).

For Manasevit's part he did deposit GaAs on sapphire, germanium and GaAs itself [4, 5], using triethylgallium (TEGa) at first and later TMGa along with arsine (AsH_3). He then went on to deposit GaAs on many different orientations of sapphire and observed the affects this had on the orientation of the GaAs film. By replacing AsH_3 with PH_3 and mixing TMGa AsH_3 and PH_3 Manasevit produced gallium phosphide (GaP) and gallium arsenide phosphide ($\text{GaAs}_x\text{P}_{1-x}$). Then replacing PH_3 with NH_3 led to the formation of GaN. The use of the MOCVD technique for all kinds of compounds built from the work on these important semiconductors.

One of the earliest problems of MOCVD was the availability of high purity metalorganic precursors or rather lack of them. TMGa manufacturers needed to be educated to prepare their product to the highest standards by additional purification steps and in some cases a supplied precursor would be further purified by the MOCVD laboratories themselves. Today very high purity precursors are available specifically for the MOCVD industry from companies such as Epichem Ltd.

Manasevit [1] also notes that alternative designations have been used to describe the MOCVD growth process namely; organometallic vapor phase epitaxy (OMVPE) and metalorganic vapor phase epitaxy (MOVPE). Manasevit rationalizes his choice of the MOCVD nomenclature by stating that "the emphasis is on the Group III and or V metalorganic constituent rather than on organometallics which encompasses a very broad class of compounds. The process is one that depends upon chemical vapor deposition (CVD) to form the desired product, whereas VPE is also applied to physical methods such as PVD and MBE".

From the very beginning of MOCVD the emphasis has been on achieving device quality material. Initially, with industry pushing the development of MOCVD, many fundamentals were not thoroughly explored leaving many unanswered questions about the growth process. During the 80's papers began to appear exploring the various aspects of the MOCVD process. G. B. Stringfellow [6]

discusses, using III/V compounds, the various zones of reaction within a MOCVD reactor: the source or input zone, the mixing zone where the precursors come together in the gas phase, and the boundary layer where the gases diffuse towards the heated substrate and the substrate surface itself. Around the same time J. Van De Ven *et al.* [7] performed a comprehensive study of flow and temperature profiles within a horizontal MOCVD reactor.

R. L. Moon [8] provides a graph, figure 2.2.2, charting the development of MOCVD through, the number of papers published, devices manufactured and attendees to the biennial International MOVPE conference. This graph illustrates just how established MOCVD has become, making a major contribution to the optoelectronics industry. Moon also states that in 1997 MOCVD contributed about 15% of the material for devices in the optoelectronics industry. This figure continues to grow.

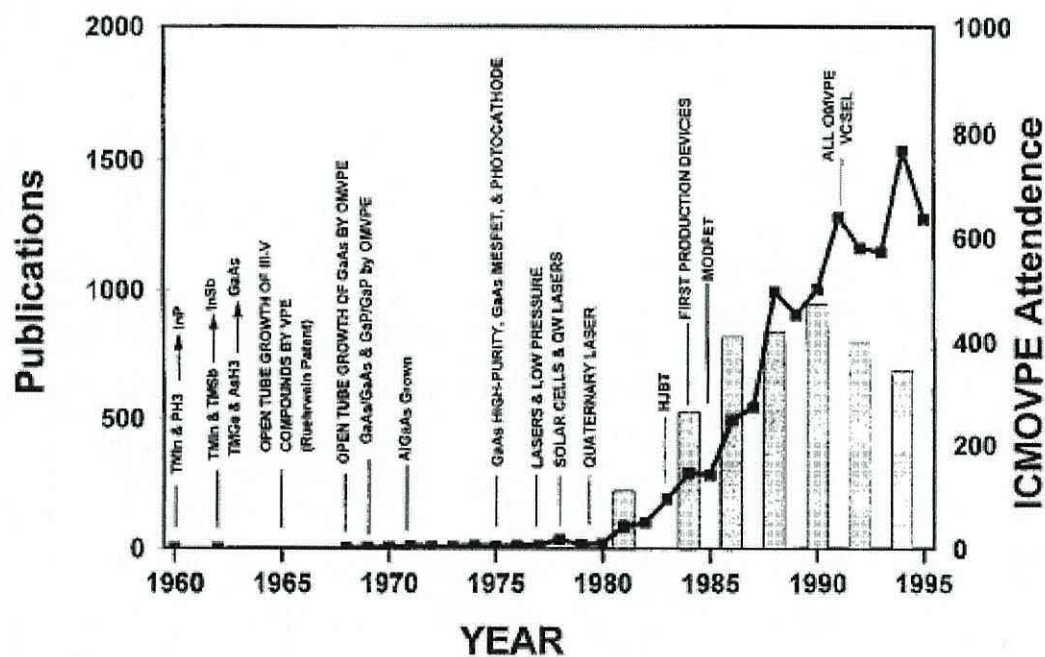


Fig. 2.2.2. History of MOVPE since 1960. Number of publications and ICMOVPE attendees versus year. After R. L. Moon [8].

2.3 The MOCVD Technique

M. R. Leys [9] gives a general outline of the MOCVD process presenting the various reactor designs, shown in figure 2.3.1, and discussing decomposition mechanisms. For research it is not necessary to produce more than one wafer for each growth run, therefore, more traditional single wafer reactors are employed. These reactors are manufactured using quartz glass to resist the high temperatures. A graphite susceptor on which the substrate is mounted is held within this cell and growth generally takes place from atmospheric pressure down to 0.1 atm.

In figure 2.3.1. reactor (a) employs a rotating susceptor to obtain good homogeneity in layer thickness. Reactor (b) is a horizontal reactor and is the selected reactor type for this research; it provides a high degree of homogeneity in epitaxial layer thickness and composition. Reactor (c) the horizontal 'T' reactor is similar to (b) but includes a rotating susceptor. The horizontal reactor with the inverted substrate mounting (d) has also proven to grow very high quality films. Reactor (e) is similar to (a) but placed horizontally and in (f), the chimney reactor, the gases are introduced at the bottom of the tube and flow upwards through a hollow susceptor on the inside of which the substrates are positioned.

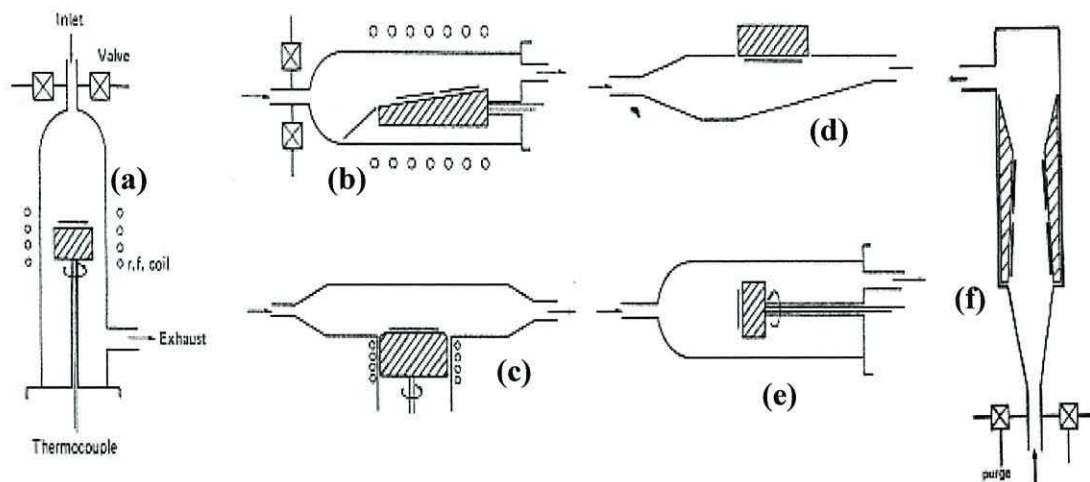


Fig. 2.3.1. Various MOCVD Reactors. (a) Rotating disc reactor, gas inlet at the top; (b) horizontal reactor; (c) 'T' reactor, horizontal with rotating susceptor; (d) reactor with inverted wafer mounting; (e) horizontal perpendicular reactor and (f) chimney reactor. After M. R. Leys [9].

Commercial reactors today are designed to produce many uniform and reproducible wafers in one reaction chamber and are run 24 hours a day to keep up with demand from the optoelectronics industry. The two main manufacturers of MOCVD equipment are Aixtron based in Germany and Emcore based in the USA (see figures 2.3.2. a and b). Aixtron employ a horizontal reactor design in which; the precursor gases are introduced into the middle of a rotating platform containing further small rotating platforms, within which single wafers rotating are located. The system is known as the Planetary Reactor as its motion resembles the orbits of the moons and planets around the sun.

Emcore follow a vertical reactor setup. The precursor gases enter a barrel shaped reaction chamber from the top. A disc onto which a number of wafers are placed is revolved at high speed within the reaction chamber and this spinning action draws the precursors over the surface of the wafers. The reactor is known as the Turbo Disc system and the exhaust gases exit beneath this spinning disc. Both systems claim to be efficient and provide reproducible results and indeed both have a large share of the market.

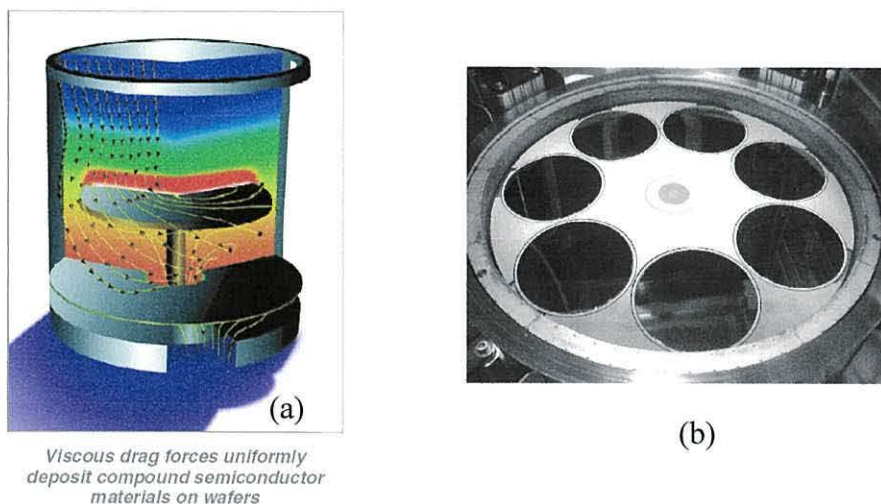


Fig.2.3.2. The Emcore Turbo Disc (a) and Aixtron Planetary Horizontal reactors (b). [10].

M. Leys [9] gives an outline of the MOCVD process for the growth of GaAs in a horizontal research reactor. This outline was used as a guide for the design of the

equipment and experimental parameters used within this thesis. A carrier gas (usually H_2 for GaAs) is purified by a diffusion treatment before passing through the precursors contained in stainless steel vessels known as bubblers. The bubblers are temperature controlled to give the desired vapor pressures. The partial pressure (concentration) of the precursors is mostly in the order of 10^{-4} atm. Figure 2.3.3. shows a schematic of a typical GaAs MOCVD reactor system.

It is interesting to outline the comments made on the horizontal reactor, in figure 2.3.2. (b), which most closely relates to the reactor used for this research. Leys states that “the flow of the carrier gas was visualised by making use of small particles of TiO_2 as markers of the streamline patterns”. From these studies, a model was developed in which two regions were distinguished in the reactor. The boundary region just above the susceptor was an area of slow moving gases over which a steep thermal gradient exists. In the region above this a free flowing layer with a less pronounced temperature difference and high gas velocity.

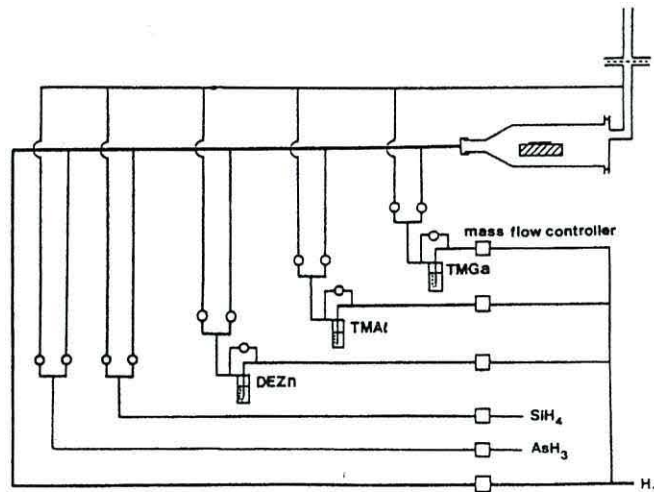


Figure 2.3.3. Schematic diagram of a MOCVD growth system. The metalorganic compounds TMGa, TMAI and DEZn are liquids stored in stainless steel bubblers. The gases AsH_3 and SiH_4 are stored in cylinders. H_2 is used as carrier gas. The amount of component which is to be transported is regulated by a mass flow controller. Sets of valves are used to introduce the components into the reactor or to vent them to the exhaust line. Substrates are placed on the susceptor which is heated to $\sim 700^\circ C$. After M. Leys [9].

The mass transfer controlled process would then be diffusion of precursors from the free flowing layer into the boundary layer. Changes in growth rate over the susceptor would then be attributed to variations in the boundary layer thickness and depletion of the gases along the length of the substrate. Leys [9] makes the point that this is a simplistic view of the flow dynamics of the reactor as it does not include convection flows from the susceptor. These free convection forces can cause slow moving spirals or longitudinal rolls through the reactor disturbing the uniformity of the gas flow resulting in non-uniform growth.

For the research into ZnO the carrier gas used was nitrogen which Leys [9] describes as “a gas with a low heat conductivity and high density”. In the case of nitrogen carrier gas the flow pattern is very strongly influenced by free convection movement. This leads to, in a horizontal reactor, a very thin laminar boundary layer close to the susceptor surface and an upper region which shows a nearly turbulent character.

Thompson *et al.* [11] raises an important factor in any semiconductor manufacturing technique, that of reproducibility. The authors outline the factors affecting reproducibility: “bubbler level and temperature, mass flow and pressure controller drift, and wafer temperature and growth rate fluctuations due to reactor wall coating and changing emissivity”. Without high reproducibility of materials a great cost is incurred due to wasted resources during calibration and unsuccessful runs.

The authors also discuss the use of *in situ* monitoring for real-time control of growth rate and composition which was shown to achieve, using the virtual interface technique, reproducibility within the first few nm of layer growth and to better than 0.1%. The *in situ* monitoring of the MOCVD process has now become commonplace. Techniques such as RAS, spectroscopic ellipsometry and laser reflectance are used to monitor the growing layers. The information gained is generally used to make film-thickness related changes during the growth process.

By this it is meant that at predetermined thicknesses changes can be made such as; composition, substrate temperature or to a layer of different compound. In this fashion precise thickness multi-layer devices can be built-up within one growth run.

On a research level *in situ* monitoring of the MOCVD technique provides essential information on the real-time growth process, complimenting *ex situ* analysis, and allowing a fuller understanding of the thin film deposition.

2.4 Precursors

MOCVD was slow to become established after the early studies of Manasevit [4, 5]. One of the main reasons was the choice of source molecules: only compounds manufactured for other purposes were considered. The common precursors used were of the type MR_n where M is the Group II, III, V, or VI element and R is methyl or ethyl radicals. However once the importance of precursor chemistry was realized, by the MOCVD community, research was undertaken to widen the choice. It is now not unusual, when contemplating the deposition of a compound, to design and investigate new or novel precursors. A high-purity precursor manufacturing industry has grown hand-in-hand with the MOCVD technique.

The major problem with the growth of II-VI compounds is the instability of the commonly available group II metal precursors. These generally decompose at low temperatures and even, in the case of dimethyl Group II metalorganics, at room temperature. This fact brings into play two problems: that of prereaction condensation and secondly premature reaction. J. B. Mullin *et al.* [12] describe premature condensation as “occurring when the temperature during transport T_{trans} falls below the source temperature T_s . Premature condensation can be avoided by suitably heating the passageway between the source and substrate so that $T_{trans} \geq T_s$ ”. Premature reaction is described by the same authors as occurring “on mixing the source elements whence supersaturation can lead to heterogeneous nucleation on surfaces in the reactor or homogeneous nucleation in the gas phase”.

The system designed for this research avoided the problem of condensation by operating the Group II source at 0°C and the Group VI source at room temperature $T_{\text{trans}} \geq T_s$. The problem of premature reaction can be somewhat avoided by a number of approaches: by mixing the precursors as late as possible, by operating at reduced pressure or by using less reactive source molecules.

Effective mixing of the source molecules can be achieved by reactor geometry and inlet design. Operating at reduced pressure is most often adopted but increases the complexities and hence costs of deposition. Choosing less reactive source molecules can be very effective at reducing or removing premature reactions. When moving to a less reactive source molecule a decrease in growth rate and an increase in reaction complexity due to larger molecules can be expected. However this is often offset by an increase in the deposited materials quality and a decrease in reactor maintenance where products of prereaction can foul the reactor.

2.5 TCOs

The first reported TCO was in 1907, when Badeker [13] reported the oxidation of cadmium in a glow discharge chamber. The cadmium oxide film was transparent and electrically conductive.

The most widely used TCO for optoelectronic devices is ITO. Other TCOs are used in specialist applications where ease of deposition, cost or IR reflectivity are favoured over optimum transmission and minimum resistivity. For example, tin oxides high IR reflectivity and large area cheap deposition by CVD lends itself well to the low-emissivity energy conserving windows. While the volume of ITO produced for many applications in the optoelectronics industry is large, the volume of tin oxide for architectural applications is equally impressive. Lewis *et al.* [14] state that “the production of energy efficient architectural glass occurs in quantities measured in tens of square kilometres per year”.

In another example, where ITO is not the favoured TCO, silver/ZnO multilayers are used to make invisible security circuits for windows. These security circuits can be used on glass over valuable works of art, the silver/ZnO film having a dual purpose providing some UV protection to prevent fading.

R. G. Gordon [15] states that “an effective TCO should have high electrical conductivity combined with low absorption of visible light thus a useful figure of merit for a TCO may be defined as the ratio of the electrical conductivity σ to the visual absorption coefficient α ”. This is described by equation 2.5.1.

$$\sigma/\alpha = - \{R_s \ln (T + R)\}^{-1} \quad (2.5.1.)$$

Where R_s is the sheet resistance in ohms per square, T is the total visible transmission, and R is the total visible reflectance. Thus σ/α is a figure of merit for rating TCOs [16]. A larger figure of merit indicates better performance of the TCO. Figures of merit for some TCOs are given in table 2.5.1. taken from the literature [15].

As stated previously an effective TCO should have a high electrical conductivity, typical values of conductivity for metals are $< 10^{-6}$ - $10^{-10} \Omega \text{ cm}^{-1}$ and for insulators $< 10^6 \Omega \text{ cm}^{-1}$. Semiconductors fall in between these values (1 - $10^{-6} \Omega \text{ cm}^{-1}$). Conductivity increases with the product of the concentration of free electrons and mobility. For wide-bandgap semiconductors such as ZnO the maximum number of electronically active dopant atoms that can be placed in the ZnO lattice determines the free electron concentration. However attempts to place a larger number of dopant atoms in the lattice produces neutral defects, which decrease the mobility. Therefore accurate control of the dopant concentration is essential for the optimization of a TCOs electrical conductivity.

Material	Sheet Resistance (Ω/\square)	Visible Absorption Coefficient (α)	Figure of Merit (Ω^{-1})
ZnO:F	5	0.03	7
Cd ₂ SnO ₄	7.2	0.02	7
ZnO:Al	3.8	0.05	5
In ₂ O ₃ :Sn	6	0.04	4
SnO ₂ :F	8	0.04	3
ZnO:Ga	3	0.12	3
ZnO:B	8	0.06	2
SnO ₂ :Sb	20	0.12	0.4
ZnO:In	20	0.20	0.2

Table 2.5.1. Figures of Merit σ/α for Some Transparent Conductors. After Gordon [15].

The use of a suitably doped ZnO TCO for PV devices requires firstly that the material be thermally stable to the deposition temperature of further layers of material and secondly to the ambient operating temperature of the PV cell. The TCOs room temperature resistance will generally increase if annealed to a high enough temperature for a long enough time. Gordon [15] states that “low-pressure CVD of ZnO:F deposited at 200°C will not show increased sheet resistance above 10% when heated up to 250 °C”. This factor must be taken into account when laying subsequent layers onto the TCO.

The aim of researching alternative compounds to ITO, as a TCO for PV devices, is to optimize efficiency. However for an alternative to be viable in the market-place the production costs must not compromise any gains in efficiency. The costs of producing a TCO depend on the cost of the raw material and the processing of it into a thin layer. Gordon [15] shows that the cost of zinc is very appealing when considered alongside other metals used in TCOs, the cost of the raw materials generally increases in this order: Cd < Zn < Ti < Sn < Ag < In.

When considering the costs of deposition technique Gordon [15] ranks them typically-increasing in the following order: atmospheric-pressure CVD < vacuum evaporation < magnetron sputtering < low-pressure CVD < sol-gel < pulsed laser deposition. Speed of deposition is also important when considering industrial applications and again atmospheric pressure CVD has a high deposition rate and has been scaled up for large area growth.

Property	Material
Highest transparency	ZnO:F, Cd ₂ SnO ₄
Highest conductivity	In ₂ O ₃ :Sn
Lowest plasma frequency	SnO ₂ :F, ZnO:F
Highest plasma frequency	Ag, TiN, In ₂ O ₃ :Sn
Highest work function, best contact to <i>p</i> -Si	SnO ₂ :F, ZnSnO ₃
Lowest work function, best contact to <i>n</i> -Si	ZnO:F
Best thermal stability	SnO ₂ :F, TiN, Cd ₂ SnO ₄
Best mechanical durability	TiN, SnO ₂ :F
Best chemical durability	SnO ₂ :F
Easiest to etch	ZnO:F, TiN
Best resistance to H plasmas	ZnO:F
Lowest deposition temperature	In ₂ O ₃ :Sn, ZnO:B, Ag
Least toxic	ZnO:F, SnO ₂ :F
Lowest cost	SnO ₂ :F

Table 2.5.2. Choice of transparent conductors. After Gordon [15]

Toxicity of some of the elements used for TCOs becomes an important factor when considering large-scale manufacturing. There is the need to protect workers and prevent the escape of toxic materials into the environment; also the disposal of the TCOs at the end of their lifetime must be considered. Toxicity of elements for TCOs generally increases in the following order: Zn < Sn < In < Ag < Cd. These factors demonstrate that, if appropriate electrical and optical properties of a suitably

doped ZnO thin film can be synthesized, MOCVD of ZnO as a TCO would be highly commercially viable. Gordon [15] gives, in table 2.5.2, transparent conductor properties illustrating the best thin films for each property.

Ginley *et al.* [17] illustrate, in figure 2.5.1, the effects that decreasing resistivity has on transmission. Two SnO₂ films with different resistivities are shown; the plasma edge moves to higher energy as resistivity decreases. The increase in conductivity has the effect of decreasing transmission in the infrared. Thus the authors state “accomplishing the goal of increased conductivity and transparency will require a deeper understanding of the relationships between the structure and the electro-optical properties of these materials and will probably require new materials as well”.

This need for new materials moving away from ITO is also driven by economics. Indium is a rare and expensive material and is obtained as a byproduct of mining for other metals such as zinc and lead. There are no indium mines as it occurs in such small quantities that its extraction is only feasible when it is not the main product of mining. Lewis *et al.* [14] shows that in the year 2000 the high demand for ITO had put pressure on the availability of indium. Lewis *et al.* [14] state that “the annual supply of indium is about 200 metric tons. Half this amount is used as ITO in FPD manufacturing in the Far East”.

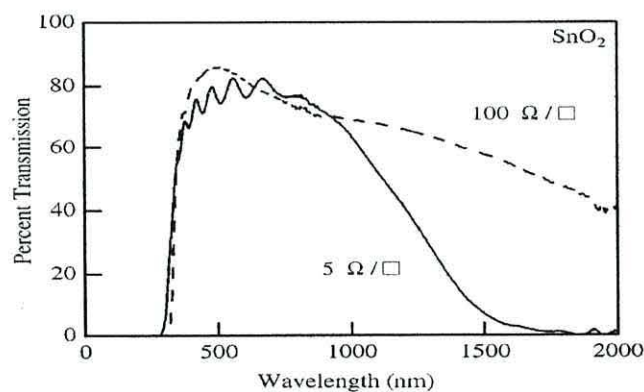


Fig. 2.5.1. Optical transparency versus conductivity for two SnO₂ films. As the resistivity decreases, long-wavelength transparency also decreases. After Ginley *et al.* [17].

Table 2.5.3. shows the favored choice of TCO's for various applications.

Application	Favoured Material	Favourable Properties
Flat panel displays	In ₂ O ₃ :Sn	Easily etchable, low deposition temp ($\geq 200^{\circ}\text{C}$), low resistance.
Low-emissivity windows (cold climates)	SnO ₂ :F	Long plasma wavelength (2 μm), high durability, low cost deposition.
Thin film solar cells	In ₂ O ₃ :Sn and SnO ₂ :F	High transparency, low resistivity, thermal stability (SnO ₂ :F), low cost (SnO:F).
Heated windows	In ₂ O ₃ :Sn	Low resistivity, durability.
Touch-panel controls	SnO ₂	Durability, low cost.
Electrochromic "Smart" windows and mirrors.	SnO ₂ :F	Chemical inertness, high transparency, low cost.

Table 2.5.3. Large scale TCO use, favoured materials and their properties.

2.6 Deposition of ZnO by Various Techniques

Thin films of ZnO semiconductors used in optoelectronic applications have generally been deposited from the vapor phase or from the liquid phase. A number of subtly different techniques have been used to grow ZnO from the vapor phase in order to achieve specific materials properties. Apart from MOCVD techniques the most widely used methods of ZnO thin film deposition quoted in the literature are Pulsed-Laser Deposition (PLD) [18-23], r.f. Magnetron Sputtering [24-29] and Molecular Beam Epitaxy (MBE) [30-33].

The PLD method involves creating a ZnO target from high purity fine zinc oxide powder, bound by methanol in the case of A. Mitra *et al.* [23], and cold pressed and

sintered at 1000°C. The ZnO targets are then subjected to pulsed laser repetition in a reaction chamber and a thin film is deposited onto a substrate some 4 cm away from the target. The advantages of PLD are that film composition is close to that of the target and the films may crystallize at lower substrate temperature.

The r.f. Magnetron Sputtering is a process whereby atoms are ejected from a solid target of high purity Zn by the impact of high-energy ions produced in the magnetron plasma. This is done in a carefully controlled oxygen/argon environment under high vacuum and results in thin films of zinc oxide being deposited onto a substrate a few cm away. The major advantage with this technique is the inherent ease with which the deposition parameters such as partial pressure of oxygen, sputtering power and substrate temperature can be controlled.

MBE employs a narrow stream of molecules formed by heating a compound in an oven with a small exit hole called a Knudson cell. Very thin layers can be deposited by directing the beam of precursor molecules onto the substrate in an ultra high vacuum (UHV) chamber. The technique is useful for growing single crystals of very specific thickness.

A number of other techniques used for the growth of zinc oxide thin films can be found in the literature such as: sol-gel [34], hydrothermal technique [35], plasma-assisted MOCVD [36-38], screen printing technique [39], spray pyrolysis [40-43], electrochemical deposition [44] and atomic layer deposition [45, 46].

Effective TCOs require that the thin film is highly conductive and are extremely optically transparent. Table 2.6.1. lists the best ZnO films with regards to these requirements and the various techniques employed to grow them. The table is divided into two sections, those of undoped and doped zinc oxide thin films.

Material	Resistivity (Ω cm)	Optical Transmittance (%)	Deposition Technique	Reference
Undoped				
ZnO	2.0×10^{-3}	90	PLD	[22]
ZnO	6.0×10^{-4}	95	MBE	[31]
ZnO	$10^{-3} - 10^{-2}$	80	MOCVD	[47]
ZnO	75 - 80	85	MOCVD	[48]
ZnO	0.31	70 - 80	MOCVD	[49]
Doped				
ZnO:B	7.5×10^{-4}	-	Atomic Layer Dep.	[45]
ZnO:B	1.33×10^{-4}	98	PA-MOCVD	[50]
ZnO:Al	9.0×10^{-4}	90	PLD	[19]
ZnO:Al	$2.7-6 \times 10^{-4}$	83	r. f. M.Sputtering	[25]
ZnO:Al	4.16×10^{-4}	80	r. f. M.Sputtering	[28]
ZnO:Al	3×10^{-3}	85 - 95	Spray Pyrolysis	[40]
ZnO:Al	6.22×10^{-4}	91	PA-MOCVD	[51]
ZnO:In	5.8×10^{-3}	86	Spray Pyrolysis	[52]
ZnO:In	$6.6-4.6 \times 10^{-3}$	80	MOCVD	[53]

Table 2.6.1. Comparison between zinc oxide doped/undoped electrical and optical properties.

2.7 MOCVD of ZnO

The most common MOCVD ZnO thin film precursors are the pyrophoric Group II alkyls dimethylzinc, $\text{Zn}(\text{CH}_3)_2$, and diethylzinc, $\text{Zn}(\text{CH}_2\text{-CH}_3)_2$, in combination with oxygen containing sources such as O_2 [48, 49, 54 and 55], H_2O , [56-60] heterocyclic compounds [47, 61] and nitrogen and carbon dioxides [60]. The highest transparency films have generally been obtained at low II/VI ratios, for this reason there has been little research into an increasing II/VI ratio. Auld *et al.* [62] have carried out research on the single source precursors; methylzinc isopropoxide and methylzinc tert-butoxide, thin films of zinc oxide were successfully grown in the absence of an added oxygen source. However it has proved difficult to obtain film resistivities $< 10^{-1} \Omega$ cm using single source precursors.

The most frequently used oxidizing sources are oxygen and water, however prereactions occur in these cases predominantly in the upstream part of the reactor leaving a white deposit at the exit. Some measures can be taken in order to

overcome this problem such as using low-pressure growth or mixing the gases close to the susceptor.

In 1991 Wenas *et al.* [56] investigated the growth of ZnO by low-pressure (1-25 Torr). The purpose of the research was to deposit rough and highly conductive thin films which are required for transparent front electrodes and antireflection coating for *a*-Si and CuInSe₂ solar cells. It had been shown by Pier *et al.* [63] that the conversion efficiency of these solar cells could be improved by using a rough TCO.

Wenas *et al.* [64] used DEZn and H₂O transported to a horizontal reactor via Ar carrier gas. The films were grown on Corning 7059 glass substrates and the substrate temperature varied from 100 to 300°C. Figure 2.7.1. shows that the growth rate was found to increase as the substrate temperature increased and became constant at higher temperatures.

Films deposited at temperatures above 300°C, when a decrease in growth rate could be expected due to desorption, were not reported. Figure 2.7.1. was attributed to the growth rate being limited by the dissociation of the reactant gases at lower temperatures. Figure 2.7.1. also shows the difference in growth rate at reactor pressures of 12 Torr and 20 Torr. DEZn reacts spontaneously with H₂O at room temperature; it was proposed by Wenas *et al.* [64] that the increase in growth rate, with decrease in reactor pressure, was a result of a reduction in this premature reaction due to fewer collisions in the gas phase.

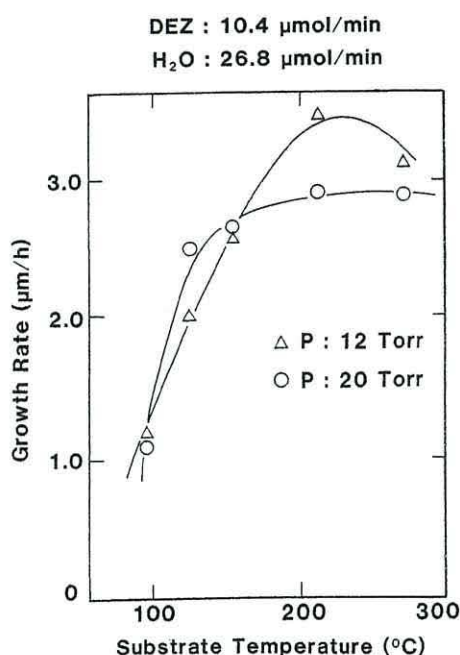


Fig. 2.7.1. Growth rate of the undoped ZnO films as a function of substrate temperature. After Wenas *et al.* [52].

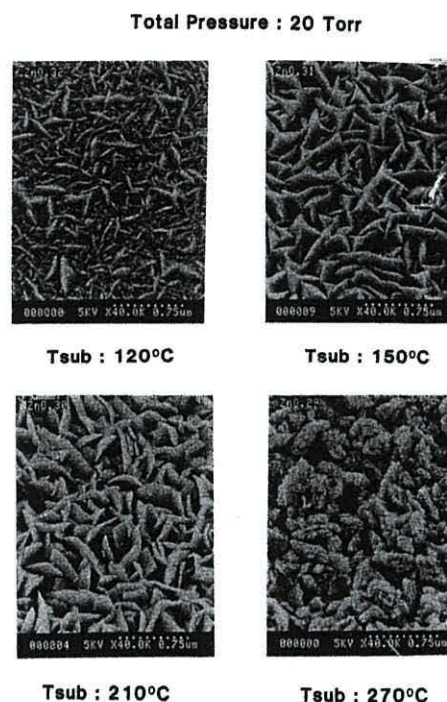


Fig. 2.7.2. SEM micrographs of ZnO films deposited at various substrate temperatures. After Wenas *et al.* [52].

The SEM images in figure 2.7.2. show the surface morphology of the ZnO films. At 150°C the films showed a tetrapod-like morphology which, the authors declared, became less pronounced at lower temperatures. The optical properties of a 2.5 μm -thick film are shown to have transmission above 80% between 400 and 1400nm.

In further work Wenas *et al.* [56] deposited boron doped ZnO films under similar conditions. They grew the films at substrate temperatures as low as 90°C but found that the films grown at 150°C showed the best rough morphology and low resistivity (10^{-2} ohms cm). The best ZnO films were applied to the preliminary stage of CuInSe₂ solar cells as TCOs and AR coatings giving promising results.

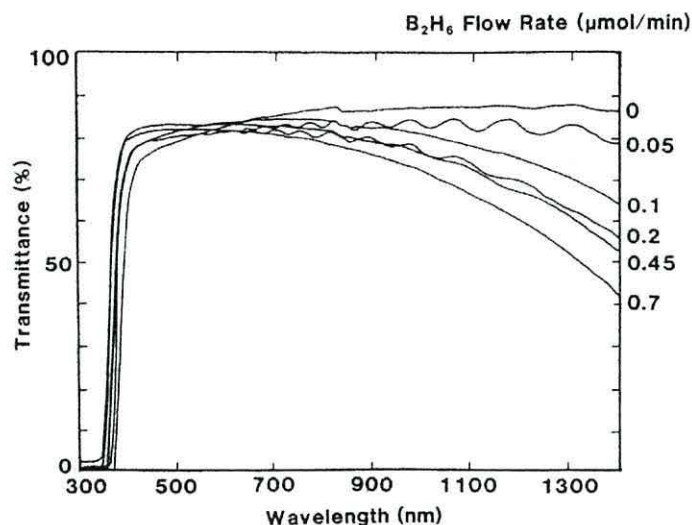


Fig. 2.7.3. Transmittance of the ZnO films grown at various B_2H_6 flow rates. After Wenas *et al.* [56].

Wenas *et al.* [56] noted that the optical gap increased with increasing B_2H_6 concentration (figure 2.7.3.). This was explained by the Burstein-Moss shift, the authors stated “in the heavily doped *n*-type semiconductor, the Fermi level is inside the conduction band and the states near the bottom of the conduction band are filled. Therefore, the absorption edge should shift to higher energy”.

Minami *et al.* [65] deposited transparent and conductive undoped and doped ZnO thin films by atmospheric MOCVD. The precursors used were zinc acetylacetonate ($Zn(C_5H_7O_2)_2$) and H_2O and the films were deposited onto Corning 7059 glass. It was found that, in the undoped films, the resistivity decreased as substrate temperature increased, table 2.7.1.

Substrate Temperature (°C)	350	450	550
Resistivity (Ωcm)	1.1×10^{-1}	3.7×10^{-2}	4.6×10^{-3}

Table. 2.7.1. Substrate temperature versus resistivity of undoped ZnO films. After Minami *et al.* [65].

Minami *et al.* [65] (figure 2.7.4.) used XRD to show that the films were polycrystalline with preferential (0002) orientation; c-axis perpendicular to the substrate. The intensity of the (0002) appears to increase with increasing substrate temperature. Like Wenas *et al.* [52] Minami *et al.* [65] show, in figure 2.7.5, the transmission spectra of two undoped and two Al doped ZnO films of different thicknesses. A transmission above 85% between 400 and 800nm was shown for samples of less than 300nm thickness. The differences in the absorption edge were attributed to the thickness and carrier concentration of the films. Minami *et al.* [65] state that “at thickness values above 400 nm, the transmittance considerably decreases at shorter wavelengths because of the scattering of incident light at the rough surface”. No attempts were made to investigate the possibility of a change in band gap between the samples.

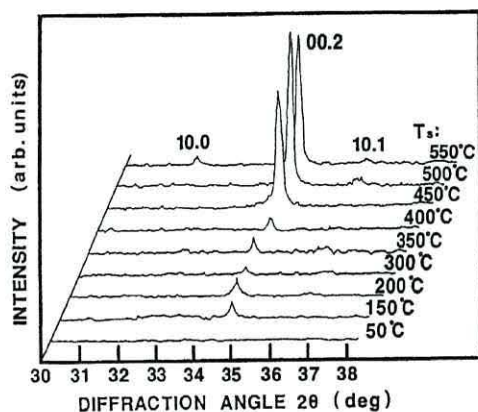


Fig. 2.7.4. XRD profiles for ZnO films deposited at different substrate temperatures. After Minami *et al.* [65]

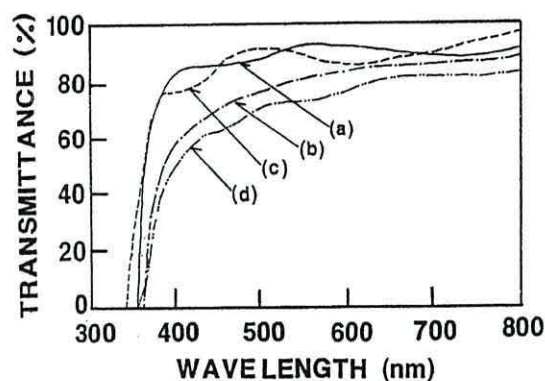


Fig. 2.7.5. Transmission spectra for undoped ZnO films with thicknesses of (a) 200 nm and (b) 450 nm and ZnO films with thicknesses of (c) 200 nm and (d) 400 nm. After Minami *et al.* [65]

Wright *et al.* [61] explored the reaction of DMZn and oxygen containing heterocycles in an attempt to solve the problem of premature reactions up-stream of the substrate. The heterocycles used were furan (C_4H_4O), tetrahydrofuran (C_4H_8O) and tetrahydrophyran ($C_5H_{10}O$). The maximum growth rates achieved on GaP substrates were 0.5 $\mu\text{m/h}$, 1.2 $\mu\text{m/h}$ and 2.0 $\mu\text{m/h}$ for furan, tetrahydrofuran and tetrahydrophyran respectively. No growth was observed at temperatures below 300°C. The growth rate versus substrate temperature profile followed the usual

trend; growth rate increased from low temperatures to a maximum, in this case around 370°C, and then decreased towards higher temperatures. It was noted by Wright *et al.* [61] that “an insignificant but just discernable film sometimes occurred on the reactor walls just upstream from the hot susceptor”.

Wright *et al.* [61] concluded that ZnO grown using oxygen containing heterocycles showed: reasonable growth rates, resistivities around $10^{-1} \Omega \text{ cm}$ and a preferred (002) orientation. The % transmission data was not so convincing at ca. 60% transmission between 500 and 700 nm.

An example of atmospheric MOCVD using oxygen is given by Suh *et al.* [48]. The zinc precursor was bis(2, 2, 6, 6-tetramethylpiperidino)zinc, $\text{Zn}(\text{tmp})_2$ and followed work where transition-metal amide complexes in combination with O_2 had given the corresponding metal oxide films at low substrate temperatures. This zinc precursor has the benefit of being non-pyrophoric. Suh *et al.* [48] deposited ZnO films on glass at 400°C, which showed resistivities of 75-80 $\Omega \text{ cm}$ and transparencies in the range of >80%.

Wenas *et al.* [66] used DEZn and D_2O as the oxidant for deposition of boron doped ZnO onto glass substrates by MOCVD. The experiments were carried out at low pressure (6 Torr) and films were also deposited from H_2O to show comparison. This comparison of D_2O with H_2O , almost identical chemically but differing in mass, highlights the complexity of MOCVD reaction mechanisms.

The SEM images, figure 2.7.6, show that although the growth conditions are identical the film grown with D_2O exhibits the macroscopic appearance of a smooth mirror like surface whilst the film grown with H_2O has a rough surface morphology. Wenas *et al.* [66] suggested that by using a mixture of D_2O and H_2O as the oxidant the surface morphology could be modified between smooth and rough to suit requirements.

Figure 2.7.7. shows the difference in the crystal orientation of the films grown with the two oxygen precursors. The authors state that “since D_2O and H_2O have almost the same chemical properties, the difference originates only from their physical properties. Since the D_2O is heavier than H_2O , it can be thought that the surface migration, as well as the transport properties of their precursors, may be different and this may cause a difference in their T_{trans} ”. Wenas *et al.* [66] did not elucidate further the difference in their chemical reactions or propose any reaction mechanisms.

The changes in resistivity of the films (D_2O and H_2O) with increasing substrate temperature showed similar tendencies. This was contrary to the changes in crystal orientation and led Wenas *et al.* [66] to conclude that “the change of resistivity with substrate temperature is not due to the change of crystal orientation of the films but more possibly to the change in the incorporation mechanism of dopant boron atoms”. A low incorporation of boron atoms at low temperature and desorption of the B_2H_6 molecules from the surface at high temperatures.

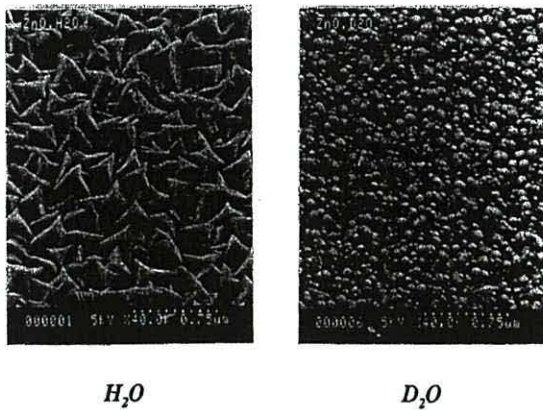


Fig.2.7.6. SEM images of 1.5 μm ZnO films grown by MOCVD using D_2O and H_2O as oxidants at 130°C. After Wenas *et al.* [66].

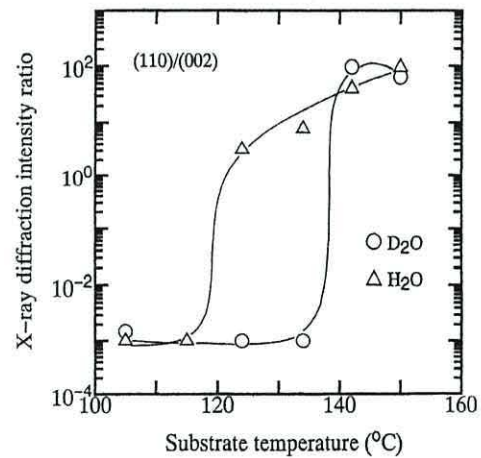


Fig. 2.7.7. Ratio of XRD intensities of ZnO films ((110)/(002)) as a function of substrate temperature. After Wenas *et al.* [66].

The MOCVD system in this research employs the mixing of the gases close to the susceptor to avoid prereaction. Also, an alcohol as a less reactive oxidizing source

has been employed following the first reported use of alcohol precursors for the MOCVD of ZnO thin films by Oda *et al.* [67]. In order to avoid the premature reactions often associated with well-known oxygen precursors such as O_2 , H_2O , CO_2 and NO_2 Oda *et al.* [67] pursued a new approach employing alcohols (R-OH) as oxidizing agents for DEZn. A horizontal reactor with tilted substrate and He as the carrier gas was used. Pressure in the system was adjusted using a rotary pump and throttling valve and the vapor pressure of the precursors was kept constant by immersing the bubblers in temperature controlled baths. Concentrations of precursors were maintained by controlling the flow rates of the He carrier gas.

2.8 MOCVD of ZnO Using Alcohol Precursors

Oda *et al.* [67] used three different alcohols to deposit ZnO; methanol, ethanol and tertiary butanol and H_2O for a known system comparison. For the alcohols, at low temperatures, growth rate increased as temperature increased showing the precursors were decomposed thermally. At high temperatures growth rates dropped due to depletion of the reactant gases at the substrate surface and white powdery deposits were found on the reactor tube instead.

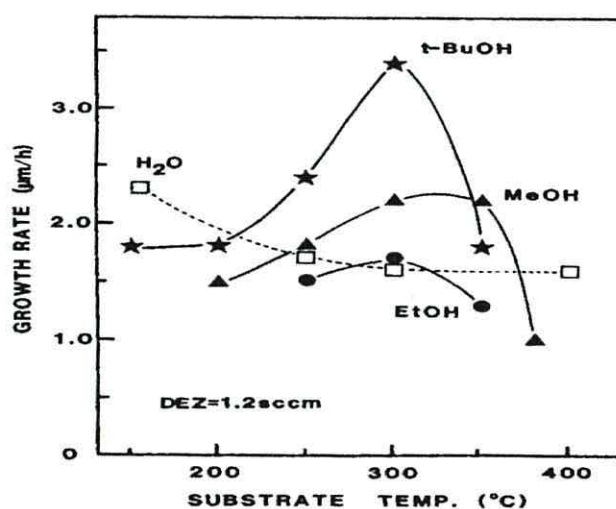


Fig. 2.8.1. The growth rates of ZnO films versus the substrate temperature for various oxidizing agents of DEZn). After Oda *et al.* [67].

Figure 2.8.1. shows the three alcohol precursors each having a maximum growth rate around 300°C after which the growth rate decreases due to mass transport effects at the substrate, while growth rate versus temperature for H₂O follows a reverse trend being higher at low temperatures and gradually decreasing for higher temperatures.

Oda *et al.* [67] studied the role of water as an impurity in the alcohols and found that it plays an important role in the growth of ZnO. The alcohols were thoroughly purified and then water was added in measured amounts, it was found that films grown from the purest alcohols were easily peeled from the surface. Addition of a small amount of water resulted in strongly adhered films.

Oda *et al.* [67] tried to clarify the role of the water in the growing film by supplying water only at the initial stages of growth and then continuing growth without water. The resultant film had the same properties as those grown without water. This result indicated that the H₂O role is not limited to the nucleated process but is integral to bulk growth. Deposition rates did not change significantly when water concentration was varied by a factor of 500. Oda *et al.* [67] concluded that the problem of premature reactions had been overcome and that tertiary butanol (t-BuOH) gave the best results of the alcohols providing defect-free and highly oriented films.

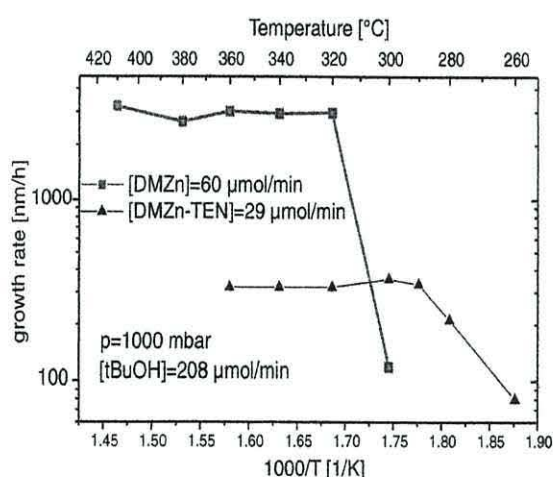


Fig. 2.8.2. Growth rate of ZnO versus growth temperature. After Hahn *et al.* [68].

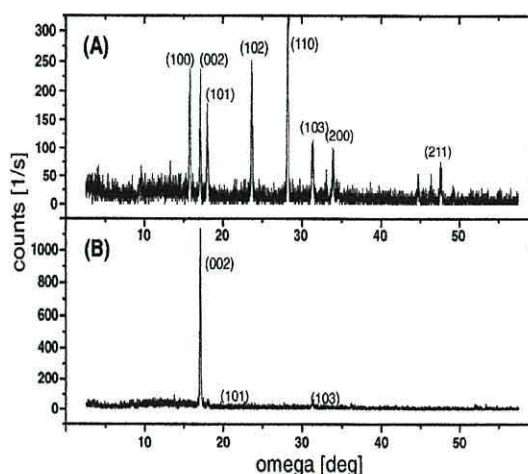


Fig. 2.8.3. XRD spectra of ZnO (A) grown with VI/II = 3.5 and (B) VI/II = 16 at 360°C. After Hahn *et al.* [68].

Hahn *et al.* [68] used t-BuOH and DMZn for the MOCVD of ZnO in an atmospheric pressure horizontal reactor. Both hydrogen and nitrogen carrier gases were used and were shown to have no influence on the sample properties. Hahn *et al.* [68] also used the adduct compound dimethylzinc-triethylamine (DMZn:TEN) which has a much lower vapor pressure (11.4Torr @ 0°C) than DMZn (120Torr @ 0°C) and is known to prevent premature gas-phase reactions in the growth of ZnS and ZnSe [69].

It was shown in figure 2.8.2. that for both precursors, in the temperature region < 300 °C, growth rate increased as temperature increased and that growth rate at high temperatures up to 410°C was limited by mass transport. Hahn *et al.* [68] studied the effect of different VI/II ratios on growth rate and morphology and found that, for the DMZn/t-BuOH system, high ratios (VI/II = 16) gave samples with mirror like surfaces without texturing showing strong (002) reflection peak; indicating *c*-axis orientation perpendicular to the substrate surface in most grains.

Hahn *et al.* [68] concluded that ZnO thin films can successfully be grown using DMZn or DMZn:TEN with tertiary butanol at atmospheric pressure using nitrogen or hydrogen as carrier gases. No premature reactions were observed and using high VI/II ratios leads to improved *c*-axis orientated films. It was noted that growth efficiency is greatly reduced by using the DMZn:TEN adduct.

Hahn *et al.* [68] also present XRD data, figure 2.8.3. of a film grown at a high VI/II ratio which showed a strong *c*-axis preferred orientation. Whereas the films grown at low VI/II ratios showed multiple peaks characteristic of unorientated polycrystalline ZnO.

Sallet *et al.* [70] have grown ZnO on sapphire (0001) substrates using DMZn:TEN and t-BuOH at atmospheric pressure in a horizontal reactor. The VI/II precursor ratio was varied between 1 and 20 and films were deposited over a temperature range of 270-450°C. The conditions of VI/II = 5 and 420°C gave the best results.

The work concentrated on the cleanliness of the reactor prior to deposition and how it influenced the morphology and orientation of the thin films. It was found that a freshly cleaned and degassed reactor resulted in layers exhibiting smooth morphology figure 2.8.4. and a (0001) orientation. However those films grown in subsequent runs exhibited a discontinuous rough surface composed of a stacking of coalesced grains.

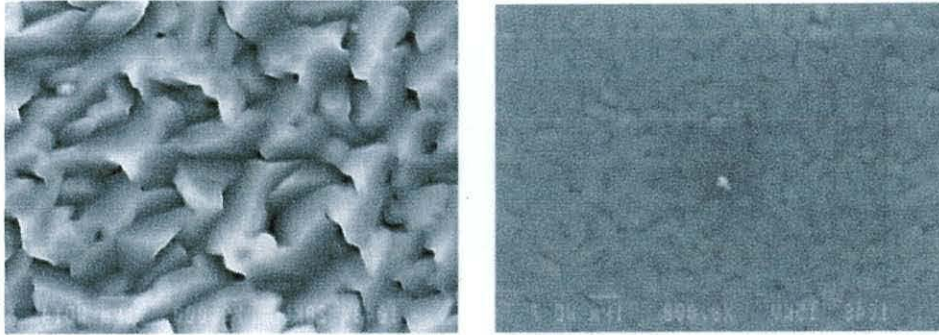


Fig. 2.8.4. SEM images of surface morphology of ZnO/sapphire films grown in a cleaned MOCVD reactor (right) or after several runs (left). After Sallet *et al.* [70]

Sallet *et al.* [70] attempted to clarify these results by running a substrate at 420°C under the hydrogen carrier gas for 5 minutes in a reactor that had not been cleaned or degassed. AFM studies of the surface revealed nanocrystallites, believed to be ZnO dots up to 5 nm in height, covering the sapphire surface. It was proposed that these nanocrystallites affected the morphology of subsequent layers grown on them leading to the rough surface shown in figure 2.8.4. (left). Sallet *et al.* [70] summarized that this particular MOCVD process would not be industrially viable for high-quality single crystalline layers due to the necessity for a clean reactor for each run.

Kirchner *et al.* [71] also studied the use of alcohol precursors, i-PrOH and t-BuOH, for the deposition of ZnO thin films. DEZn was used as the zinc source and the reactor pressure was varied between 200 and 500 mbar, the substrates were *c*-plane sapphire. Kirchner *et al.* [71] successfully deposited ZnO with both oxygen precursors; finding that the i-PrOH achieved a maximum growth rate at only 380°C

whilst the t-BuOH gave a constant growth rate over a wide temperature range 380-510°C. The authors found the optical properties of the t-BuOH films also to be superior.

Kirchner *et al.* [71] discuss the likelihood of an intermediate product formed between the DEZn and the alcohol. This alkylzinc alkoxide intermediate product is discussed in more detail in chapter 2.9. Kirchner *et al.* [71] state that “an alkylzinc alkoxide forms in the gas phase prior to the ZnO deposition on the substrate surface. This alkoxide is dissociated into zinc and oxygen on the substrate surface and forms ZnO.

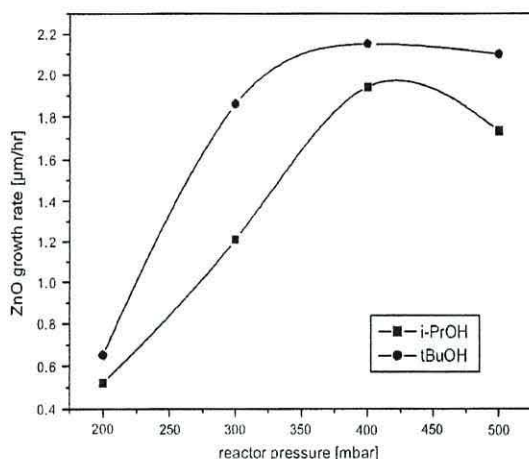


Fig. 2.8.5. Growth rates of i-PrOH and t-BuOH as oxygen precursor. Substrate temperature for both samples is 380°C and VI/II ratio is 18. After Kirchner *et al.* [71].

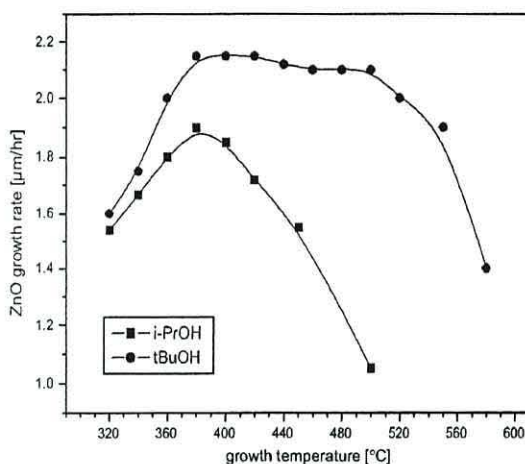


Fig. 2.8.6. Temperature dependence of the ZnO growth rate using i-PrOH or t-BuOH as the oxygen precursor. DEZn flow rate is 100 μmol/min. Reactor pressure for both samples is 400mbar. After Kirchner *et al.* [71].

Kirchner *et al.* [71] found the reactor pressure to be a crucial parameter for higher growth rates figure 2.8.5. The maximum growth rate for both alcohol precursors was achieved at 400 mbar, when the pressure was decreased the growth rate sharply decreased. This was ascribed to the mean-free paths of the DEZn molecules and alcohol precursor molecules being too long at low pressures, resulting in low alkylzinc alkoxide formation in the reactor. On increasing the pressure, above 500

mbar, i-PrOH was seen to give a white powdery deposit upstream of the susceptor and t-BuOH gave brown flakes on the susceptor.

Kirchner *et al.* [71] made a suggestion on the difference in growth rate versus substrate temperature between the two alcohol precursors, figure 2.8.6. They state that it is due to “a difference in stability of the alkylzinc alkoxides formed by i-PrOH or higher alkalized t-BuOH. Kirchner *et al.* [71] also state that “formation of the intermediate alkoxide is mandatory for MOCVD of ZnO if an alcohol is used as the oxygen precursor. Stable adducts can be efficiently transported to the substrate and then decomposed (heterogeneously) at the growth surface”.

	Diethylzinc	n-Butanol
Formula	$(C_2H_5)_2Zn$	$CH_3(CH_2)_2CH_2OH$
B. P.	118°C	118°C
M. P.	-28°C	-89°C
Vapor Pressure	12 mmHg @ 20°C	5 mmHg @ 20°C
Appearance/Odor	Colorless liquid/ -	Clear colorless solution/ characteristic alcoholic odor
Stability	Reacts violently with water, pyrophoric with air, light sensitive.	Stable under normal conditions
Health hazards	Skin contact can cause severe burns, fumes may cause Zinc Fume Fever and a hypothermic reaction, fumes may cause skin and eye irritation.	Inhalation may cause irritation to respiratory tract, ingesting has narcotic effect, will cause mild irritation to skin.

Table. 2.8.1. Table of properties of the two precursors used within this research. Data from Material Data Sheets [72].

It is suggested that the alkoxide formed by the t-BuOH is more stable than that formed by the i-PrOH. Hence the growth rate of the t-BuOH films is stable up to 510°C (mass transport limited growth); Kirchner *et al.* [71] state that “the alkoxide formed by the i-PrOH is less stable and is thermally cracked before the mass transport limited area is reached”. The possibility of t-BuOH which is a three-

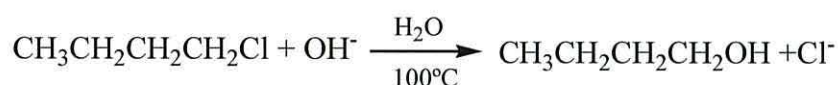
dimensional structure, rather than a chain, protecting the zinc from attack whilst in transport to the substrate surface is also noted.

The precursors; diethylzinc and n-butanol have been used to deposit zinc oxide in this research. Table 2.8.1. introduces some properties of these compounds

Diethylzinc can be obtained from the thermal decomposition of EtZnI, which is prepared by the reaction of ethyl iodide with a zinc-copper couple:



n-butanol may be prepared by the hydrolysis of alkyl halides in aqueous solvents:



Further discussion of the reaction of diethylzinc with alcohols to form alkylzinc alkoxides is given in section 2.9.

2.9 Alkylzinc Alkoxides

The organometallic and alcohol precursor gas phase reaction pathway, leading to the formation of an alkylzinc alkoxide intermediate, must be considered. The precursors can be thought of as separate entities arriving at the substrate surface, where they undergo a surface catalyzed reaction, leading to the deposition of a ZnO thin film and various volatile organic products expelled in the exhaust gas. More likely, the precursors when mixed form an “active intermediate”, the alkylzinc alkoxide. This active intermediate arrives at the reaction zone to break down, either in the boundary layer or on the substrate surface, forming a ZnO thin film and various volatile organic products again expelled in the exhaust gas.

Evidence for the active intermediate formed on mixing of the precursors comes from Coates *et al.* [73] who described reactions between zinc alkyls and various alcohols. It was shown that by slow addition of the alcohol to the zinc alkyl at -70°C , in an inert solvent, an alkylzinc alkoxide can be prepared with negligible displacement of the second alkyl group.



This alkylzinc alkoxide species would contain a co-ordinatively unsaturated zinc atom with its acceptor character enhanced by the oxygen atom whose donor character was in turn enhanced by the zinc atom. It was shown that the above effects result in the species $\text{Et}_2\text{AlOCH}_2\text{CH}_2\text{OEt}$ having the structure shown in figure 2.9.1.

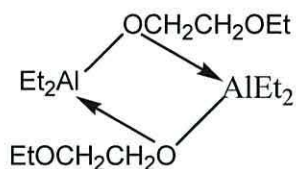


Fig. 2.9.1. $\text{Et}_2\text{AlOCH}_2\text{CH}_2\text{OEt}$.

It could be expected that alkylzinc alkoxides would be dimers analogous to figure 2.9.1. This structure would give three co-ordinate zinc, the zinc and oxygen atoms would be subject to angular strain. Both these problems were shown not to matter because nitrogen analogous to figure 2.9.1. prepared from R_2Zn ($\text{R} = \text{Me}$ or Et) and diphenylamine exist in this form. However all the alkylzinc alkoxides, produced by Coates *et al.* [73], were found to be tetrameric which were assumed to be eight-membered cyclic structures shown in figure 2.9.2. These alkylzinc alkoxides are white crystalline solids at room temperature and Coates *et al.* [73] report that they sublime unchanged when heated at 120°C at low pressure.

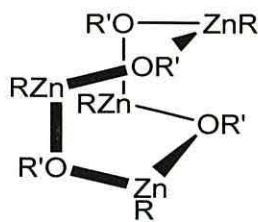


Fig. 2.9.2. Tetrameric alkylzinc alkoxide.
After Coates *et al.* [73].

This structure brings positive and negative centers relatively close together. Some interaction between O and Zn through space would effectively increase co-ordination of both the Zn and O bringing Zn closer to its full four co-ordinate state.

Further investigations into these alkylzinc alkoxides was carried out by Auld *et al.* [62] who reported that both $\text{MeZn}(\text{OPr}^i)$ and $\text{MeZn}(\text{OBu}^t)$ proved sufficiently volatile for use as single source precursors for the growth of ZnO by MOCVD. The white crystalline solids $\text{MeZn}(\text{OPr}^i)$ and $\text{MeZn}(\text{OBu}^t)$ were synthesized from $\text{DMZn}(\text{THF})$ adduct and respective alcohols. The $\text{MeZn}(\text{OPr}^i)$ was heated to 70°C in a bubbler and, using nitrogen carrier gas, was transported to the reaction zone where ZnO was deposited at low pressure (15 Torr) between 250 and 350°C . NMR studies showed that no decomposition of the precursor took place in the bubbler before or after use.

$\text{MeZn}(\text{OBu}^t)$ was held in a tube furnace and heated to 80 or 150°C depositing ZnO between 250 and 400°C again at low pressure (10^{-2} Torr). No decomposition of the $\text{MeZn}(\text{OBu}^t)$ was reported at 80°C , but significant decomposition was noted at the source temperature of 150°C . Both precursors were shown to undergo efficient intramolecular decomposition to deposit ZnO without an external oxygen source.

These results were contrary to previous work by Cockayne *et al.* [74] who found that Me_2Zn dioxin and thioxan adducts did not deposit ZnO unless additional oxygen containing precursors were present (cyclic ethers, THF or 1,4-dioxan itself). The ZnO thin films were similar to those already reported by Wright *et al.* [61] using Me_2Zn and $\text{C}_4\text{H}_8\text{O}$.

Auld *et al.* [62] used a mechanism, previously proposed by Ashby *et al.* [75], to describe how the alkylzinc alkoxide intermediate decomposes via a cyclic six-centre transition state shown in figure 2.9.3. This decomposition is facilitated by the abstraction of a β -hydrogen from the alkoxy group by the methyl group bonded

to the zinc. It was suggested that this decomposition mechanism may occur in the boundary layer or more likely on the substrate surface.

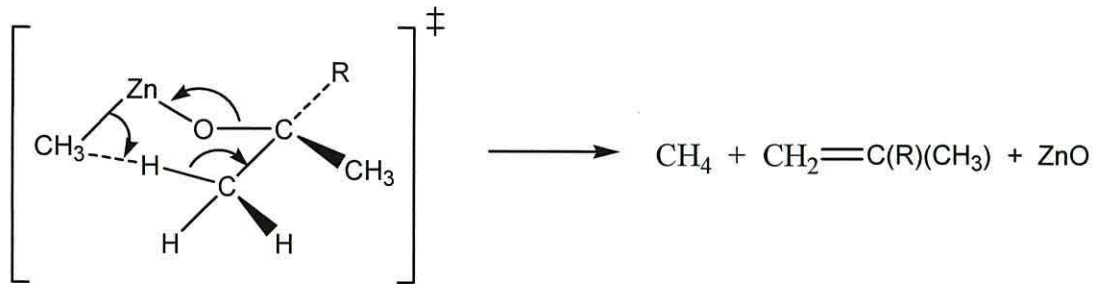


Fig. 2.9.3. Cyclic six-centre transition state. After Ashby et al. [75].

2.10 Growth modes of MOCVD

The growth of thin films on to a substrate surface involves the arrival at the surface of mobile deposit atoms, which will then either adhere to the substrate and aggregate with other deposited atoms or deflect of the substrate surface back into the reaction zone. Three main growth mechanisms, shown pictorially in figure 2.10.1. have been identified for growing thin films of one material on a substrate surface of another material:

- 1) Monolayer Growth
- 2) Nucleated Growth
- 3) Nucleation following Monolayer formation

Monolayer growth occurs when the deposited atoms are bound more strongly to the substrate than they are to each other. The deposited atoms form single layer islands on the substrate surface spreading out until they coalesce. New single layer islands form on the first monolayer and result in the deposition of a second monolayer. In this way the growth of the thin film continues monolayer by monolayer.

Nucleated growth takes place when the deposited atoms are bound more strongly to each other than they are to the substrate. The deposited atoms form many 3 dimensional islands on the substrate surface. The islands increase in size as further

atoms are deposited until they coalesce with neighboring islands to form a continuous film. This mechanism is commonly known as Volmer-Weber nucleation.

The third method is a mixture of both the first and second mechanisms whereby the initial growth is via the formation of one, or a small number of monolayers, followed by subsequent nucleation of 3 dimensional islands on top of these monolayers. This mechanism is known as Stranski-Krastanov mode.

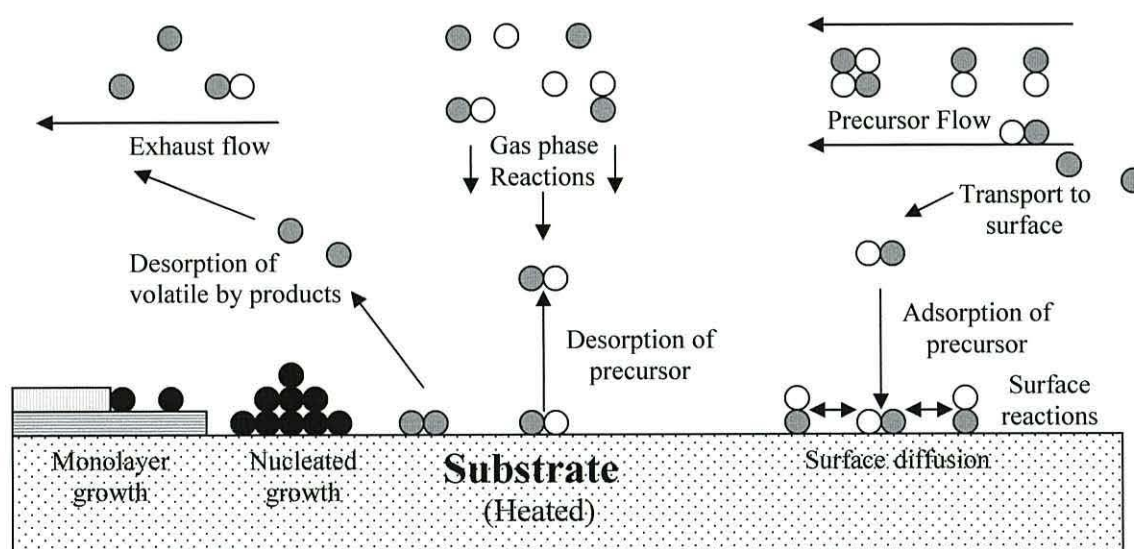


Fig. 2.10.1. The growth mechanisms of MOCVD.

2.11 Photoassisted MOCVD

In a standard MOCVD system the crystal growth process is a thermal one; close to equilibrium for liquid phase growth or at non-equilibrium for vapour phase growth. Photoassisted growth in MOCVD can follow a number of routes; the photons can be absorbed by the precursors in the gas phase leading to photolysis, the photons can act as a heat source as in photothermal-assisted crystal growth and finally the photons act as catalysts for surface reactions.

Many studies have been made on oxide thin films grown by a light source assisted MOCVD process, which is intended to cause photolysis of the precursors. The

photolysis of the one or more of the precursors in the vapour phase can reduce the thermal energy requirement of the deposition process allowing lower temperature deposition. This is desirable as many MOCVD thin film processes involve multilayer depositions under different temperatures. Heating a film above its original deposition temperature, in order to lay down a new thin film layer on top, can have an annealing affect, which may alter its properties.

An example of employing photolysis during the MOCVD procedure is given by Tamara *et al.* [76] who studied film thickness distribution of tin oxide films grown by photochemical vapour deposition. The SnO₂ films were prepared using tetramethyltin (TMT) and O₂ (containing 4 mol % O₃) at 250°C both with and without UV irradiation. The light source used was a low-pressure mercury lamp irradiating 253.7 nm and 184.9 nm wavelengths with intensities at the substrate respectively 7 and 0.6 mW/cm². 253.7 nm radiation is absorbed by ozone while the TMT absorbs the 184.9 nm radiation.

Tamara *et al.* [76] described the following results: growth rates of 0.16-0.25 µm/h for the photo-MOCVD with O₃, 0.07-0.24 µm/h for thermal only CVD with O₃, 0.03 µm/h for photo CVD without O₃. No growth was observed for purely thermal CVD without O₃. The minimum resistivity of 7x10⁻³ Ω cm was obtained at 250°C by photo-MOCVD with O₃. Tamara *et al.* [76] concluded that the 253.7 nm wavelength increases growth rate at all substrate temperatures whereas the 184.9 nm light does not affect growth rate but does form a more uniform thickness distribution. Tamara *et al.* [76] speculate that the effect of the 184.9 nm on film uniformity distribution may be due to the irradiation improving the uniformity of the reactive species distribution in the vapour phase.

In this research into ZnO thin films the photoassisted method employed consisted of subjecting the growing surface to UV irradiance designed to promote a surface catalytic reaction. Some previous examples of research carried out on photo-

induced surface catalytic reactions by Fujita *et al.* [77], on ZnSe and ZnS, and by Irvine *et al.* [78], on CdTe demonstrated the following advantages.

- The growth temperature can be significantly reduced.
- Selective area growth can be achieved.
- The materials properties such as dopant incorporation and conductivity can be enhanced.
- The substrate temperature and precursor dissociation can be controlled.
- The deposition rate can be increased.

Disadvantages of photoassisted growth are that the deposition process becomes more complex and there is relatively little knowledge of the fundamental mechanisms.

In order to avoid a gas phase reaction the UV/Vis absorbance spectra of the precursors must be studied and absorbing wavelengths filtered out. The unfiltered UV/Vis light, of energy $> E_g$ of the compound being deposited, is then absorbed promoting a photo-catalytic reaction. The intensity of the light source is such that the photo-thermal effect is relatively small ($<10\%$) compared to the deposition temperature.

Detailed studies of this method of thin film deposition have been carried out on CdTe [78], ZnS [79, 80] and ZnSe [77, 80, 81, and 82]. The proposed mechanism for the surface photo-assisted growth of ZnSe gives an idea of the mechanisms, which are involved in the growth of zinc oxide in this research.

Fujita *et al.* [80] deposited ZnSe by MOCVD using a 500W xenon arc lamp, with filters to avoid heating of the substrate, to promote a surface photo-catalysed reaction. The authors demonstrated that when the growth rate of ZnSe was measured as a function of incident light; the growth rate significantly increased at wavelengths shorter than the band gap energy (2.6 eV) see figure 2.11.1.

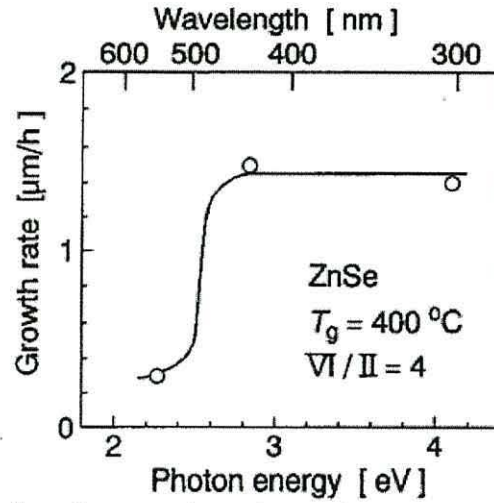


Fig. 2.11.1. Wavelength and energy dependence of growth rate in photo-assisted MOVPE of ZnSe. After Fujita *et al.* [80].

Fujita *et al.* [80] proposed a reaction scheme, figure 2.11.2, for the surface photocatalytic growth of ZnSe from DMSe and DEZn. Adsorbed species are denoted by “ad”. The initial surface reaction, eq. (1) is pyrolytic with the removal of one of the ethyl radical but the remaining ethyl blocks the surface. The second step, eq. (2) was considered, by the authors, to be a charge-transfer mechanism where the photon promotes the ethyl radical desorption indirectly via hole transfer to the surface.

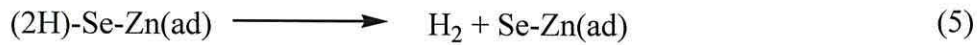
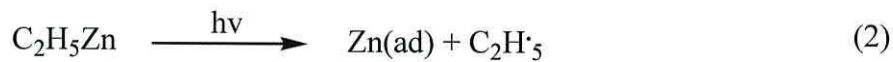
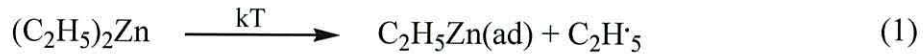


Fig. 2.11.2. Reaction Scheme of the surface photo catalytic growth of ZnSe using the precursors DMSe and DEZn. After Fujita *et al.* [80].

It can be seen that, eq (3, 4 and 5), the irradiation is promoting a photocatalysis reaction where the zinc precursor does not have to pre-dissociate on the surface.

Yoshikawa [83] attributed the growth mechanism to photo-induced excess holes. When a ZnSe surface is irradiated by photons with energy larger than the band gap of ZnSe at growth temp, electrons are promoted to the conduction band and electron-hole pairs are generated, then the holes are transferred to the surface. The oxidation number of DMSe is -2 while that of Zn in DMZn is $+2$, and both the oxidation numbers of elemental Se and Zn are 0, so DMSe may be decomposed by positive holes excited by irradiation with an oxidation reaction.

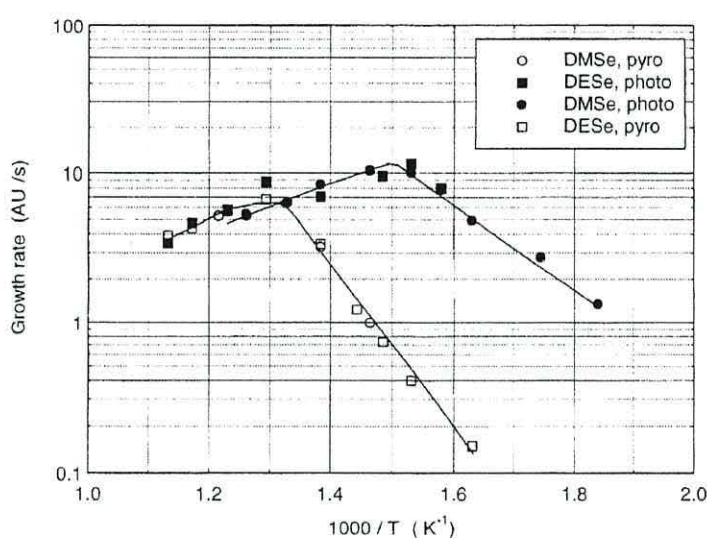


Fig. 2.11.3. Arrhenius plot for the growth rate of ZnSe to compare between the precursors DMSe and DESe. The DMZn:TEN partial pressure was 1.5×10^{-4} atm., VI:II ratio was 1:1 and photo-assisted laser intensity 50 mW cm^{-2} . After Irvine *et al.* [84].

Irvine *et al.* [84] also studied the photo-assisted growth of ZnSe. ZnSe was deposited onto GaAs substrates using the precursors DMZn:TEN with DESe or DMSe. An argon ion laser (458 nm) was used for the photo-assisted growth experiments. The intensity of the laser on the substrate surface was varied between 10 and 100 mW cm^{-2} . From figure 2.11.3. the photo-assisted method is shown to enhance the growth rate, for both selenium precursors, moving the maximum growth rate to a lower substrate temperature.

The photo-assisted growth rate enhancement was attributed to photo-assisted decomposition of the DMZn on the substrate surface. This fitted a model, produced by Ahmed *et al.* [85], in which the initiation of growth was based on the decomposition of adsorbed DMZn which led to the decomposition of DESe via surface radical reactions. These surface radical reactions, proposed to be via hydrogen radical reaction with adsorbed DESe, were shown by Ahmed *et al.* [86] to be carrier gas related.

A methyl radical reaction with the hydrogen carrier gas was suggested and when helium carrier gas was used instead, under the same growth conditions, no photoassisted growth was seen. Irvine *et al.* [84] state that “laser illumination of the surface increases the DMZn reaction rate, thus increasing the growth rate. Irvine *et al.* [84] conducted growth rate versus precursor ratio experiments to elucidate the critical reaction steps figures 2.11.4. and 2.11.5.

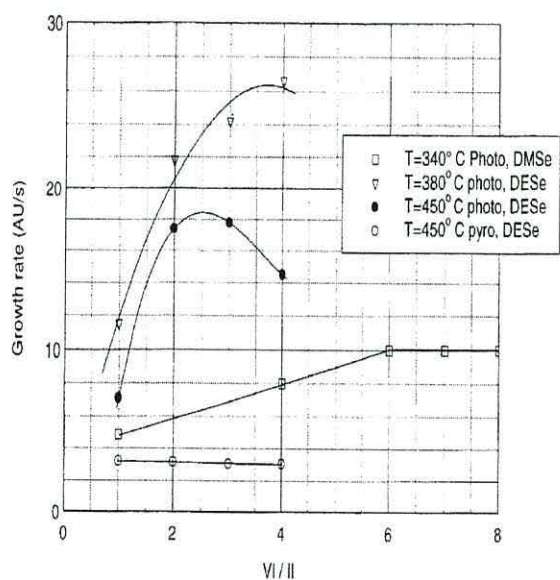


Fig. 2.11.4. Growth rate as a function of VI/II ratio for the Se-rich conditions using DESe and DMSe as indicated. The partial pressure of DMZn:TEN was fixed at 1.5×10^{-4} atm. The laser intensities for the photo-assisted growth experiments were 90 mW/cm^2 for DESe and 40 mW/cm^2 for DMSe. After Irvine *et al.* [84].

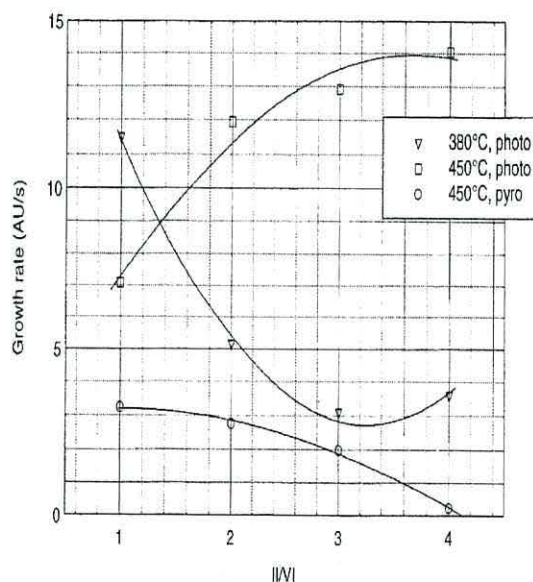


Fig. 2.11.5. Growth rate as a function of II/VI ratio for zinc-rich conditions where the DESe concentration was kept constant at 1.5×10^{-4} atm. After Irvine *et al.* [84].

This increase in DMZn decomposition by photo-assisted growth is illustrated by figure 2.11.3. Pyrolytic growth at 450°C using DESe showed no increase in growth rate with increasing VI:II ratio whereas photo-assisted growth under the same conditions showed an increasing growth rate with increasing VI/II ratio up to 2:1. Irvine *et al.* [84] state that the enhancement is consistent with more Zn available to react with the increased concentration of DESe on the surface. When the II/VI ratio was increased, at 450°C pyrolytically, the growth rate decreased whereas at 450°C with photoassisted growth the rate increased. This was attributed, respectively, to site blocking by unreacted DMZn on the surface and DMZn decomposition with laser illumination.

Irvine *et al.* [84] noted that the decrease in growth rate with II:VI ratio for photo-assisted growth at 380°C showed that other factors dominated at the lower temperature. To explain this result Irvine et al. [84] summarize the competitive factors determining growth rate.

- Desorption of unreacted precursors reducing growth rate.
- Surface reaction initiated by DMZn decomposition.
- Site blocking by unreacted organometallics or adsorbed products.

To decide which factor results in the decrease of photo-assisted growth rate, with increasing II/VI ratio at 380°C, the temperature regime of the reaction must be considered. Irvine *et al.* [84] state that “if the growth rate is in the low temperature thermally activated regime then site blocking is going to dominate. If the growth rate is near the maximum then desorption of unreacted precursors is going to become more significant”.

2.12 Photoassisted MOCVD of ZnO

It has been shown in chapter 2.4 that there is a need for low temperature deposited TCOs. The problems encountered with the growth of ZnO at low temperatures are not related to the stability of the precursors but to the poor crystallinity obtained.

This aspect of materials quality at low temperature growth opens the door for a non-thermal excitation approach such as the photoassisted method of this research. There have been few reports of photolysis assisted MOCVD of ZnO and none on surface catalyzed photoassisted.

Of the undoped zinc oxide thin films, in table 2.6.1, the most attractive for TCO applications are the two that combine low resistivity and high optical transparency [22 and 31]. Of the n-type doped zinc oxide thin films the best examples are those grown using Photoassisted MOCVD (PA-MOCVD) by Yoshino *et al.* [50] and Myong *et al.* [51] giving resistivities of 1.33×10^{-4} and $6.22 \times 10^{-4} \Omega \text{ cm}$ and optical transparencies of 98 and 91% respectively.

The methods of these two papers are the closest found, in the literature, to the aims of this research, although both are ambiguous as to the photochemical mechanisms assisting the growth in terms of whether they are gas phase or surface activated. The paper by Yoshino *et al.* [50] describes the growth of boron doped zinc oxide thin films using a low-pressure mercury lamp as an ultraviolet light source. The precursors DEZn and H₂O were kept in temperature-controlled baths and bubbled with pure Ar carrier gas. B₂H₆ was used as the dopant precursor and it was noted that at high concentrations of dopant the transmittance of the zinc oxide decreased in the longer wavelength region. Depositions were carried out between 125°C and 140°C, which are very low temperature ranges and emphasize the effect of photoassisted growth.

The influence of the light intensity was studied with the conclusion that when the intensity was too high, it became difficult to obtain good quality films therefore it is necessary to optimize the UV light intensity. It was noted that the deposition rate remained the same for all intensities of UV irradiance. The results of various growth runs indicated that UV irradiation during growth is very effective, only in the improvement of the electrical properties of the films, but even at low light intensity. However no attempt was made to filter out UV wavelengths that would

be absorbed by the precursors in the gas phase and thus it is difficult to know which reaction is dominant in this experiment; photochemical reactions in the gas phase or the surface photochemical reactions. SEM images showed that the films were all of the rough surface morphology.

The work by Myong *et al.* [51] is another example of PA-MOCVD of ZnO. The authors describe the growth of aluminium doped zinc oxide thin films again utilising a low-pressure mercury lamp to enhance the electrical properties. DEZ and H₂O were used as the precursors for the zinc oxide thin film and an aqueous solution of AlCl₃(6H₂O) as the doping gas. The carrier gas was high purity Ar and the substrate temperature ranges were 120°C to 150°C.

Myong *et al.* [51] make comparisons between doped and undoped thin films using the same growth parameters demonstrating that *n*-type doping of zinc oxide significantly enhances electrical conductivity whilst not reducing transparency. The photoassisted aspect of the work was not commented on and seemed to be used purely to decrease the resistivity of the films in response to the work by Yoshino *et al.* [50]. No consideration as to the photochemical mechanism was given and again no attempt was made to filter out UV absorbing wavelengths of the precursors.

Shimizu *et al.* [87] deposited ZnO thin films using DEZn and O₂, in a low-pressure reactor with argon carrier gas, by PA-MOCVD. The reaction chamber was kept at 1 Torr during growth and a 500 W high pressure mercury lamp or a 500 W xenon-mercury lamp provided the UV irradiation. Shimizu *et al.* [87] achieved photo-deposition at temperatures between 200 and 350°C, above 350°C the irradiation had no effect on the growth rate which was attributed to re-evaporation and a change in the sticking coefficient.

Using one or other of the lamps and ultraviolet transmitting filters Shimizu *et al.* [87] were able to study the variation in growth rate versus the wavelength of irradiation. The results, shown in figure 2.12.1, were that the shorter wavelength

light 220-410 nm gave the highest growth rate suggesting photo-dissociation of DEZn whose main absorption lies between 150-300 nm. The increased growth rate with 320-419nm wavelengths was suggested to result from a contribution of the red shifted tail, in the absorption spectrum, to some gas phase photo-dissociation of DEZn or the possibility of some surface photo-catalyzed mechanism. The latter is more likely because the gaseous absorption spectrum of DEZn is shown by Krchnavek et al. [88] to extend to wavelengths only as long as 290nm.

Previously to the deposition of the ZnO films the authors had carried out pyrolysis and photo-decomposition experiments of DEZn within the same reactor. Shimizu *et al.* [87] state that “Zn films of a grayish colour were deposited at substrate temperatures of 250-350°C. When the substrate was exposed to UV light from the high pressure mercury lamp, at room temperature, Zn films were formed on the substrate. The thickness of the films obtained increased as the short wavelength limit of the light source was decreased from 300 to 220 nm using UV transmitting filters. No film at all was deposited when the filter reached transmittance wavelength of 300 nm”.

The resistivity of the films grown by Shimizu *et al.* [87] was shown to decrease with increasing substrate temperatures, the lowest resistivity being around $10^1 \Omega \text{ cm}$ at 300°C. The films deposited with UV light irradiance were shown to be of lower resistance at the same substrate temperature, the lowest being $10^{-1} \Omega \text{ cm}$. In this work the lower resistivities were attributed to a better crystallinity of the photo-deposited films.

Yamada *et al.* [89] deposited ZnO films using the photo-MOCVD technique. DEZn and H₂O were used as the precursors and the deposition carried out at 6 Torr on Corning 7059 glass substrates. In this work the influence of the UV irradiation was discussed in some detail. The UV light source was a low-pressure mercury lamp, radiating intense 184.9 nm and 253.7 nm resonance lines (30 mW/cm^2 at 3

cm distance). Like the work by Yoshino *et al.* [50] no significant change in growth rate was noted under UV irradiation.

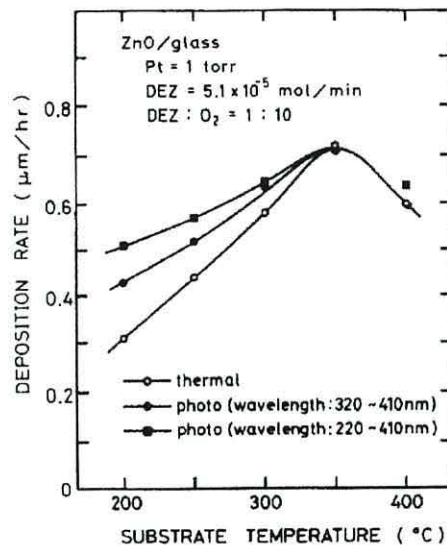


Fig. 2.12.1. Variation of the deposition rate as a function of substrate temperature and effect of the UV light irradiation on the deposition rate. 0.4 mW/cm² (320-410 nm) and 0.7 mW/cm² (220-410 nm). After Shimizu *et al.* [87].

Yamada *et al.* [89] show in table 2.12.1. that there was a significant enhancement of the films electrical properties when deposited with UV irradiation. The authors state that “both the electron mobility and the carrier concentration of the film grown with UV irradiation are higher than those of the film grown without UV irradiation”. Usually in semiconductors the electron mobility will decrease with increasing carrier concentration; the ionized impurity, giving rise to the increased carrier concentration, will increase scattering therefore decreasing mobility.

	Mobility (cm ² /V.s)	Carrier Concentration (x 10 ¹⁹ cm ⁻³)	Resistivity (x 10 ⁻³ Ω.cm)
Without UV irradiation	14.5	2.6	16.0
With UV irradiation	57.3	8.0	1.2

Table. 2.12.1. Electrical properties of undoped ZnO films. After Yamada *et al.* [89].

In order to see if there was an increase in crystallinity of the films grown under UV irradiation, which could explain this enhancement in electrical properties, the

authors carried out XRD and SEM measurements. The XRD spectra revealed both films to have a dominant (110) peak suggesting the *c*-axis of the ZnO lies in the plane of the substrate. The SEM images showed both films to have a rough tetrapod-like surface morphology. It was surmised that the crystallinity of the films was unchanged by the UV irradiation.

Yamada *et al.* [89] noted that both DEZn and H₂O photochemically decompose due to the absorption of photons at wavelengths of 184.9 nm. However, there was no enhancement in growth rate under UV irradiation; therefore, the authors concluded that the DEZn reaction with H₂O is faster than photolysis. The mechanism the authors propose to explain the increased electrical properties is a passivation of the grain boundaries with oxygen. It is noted that this is contrary to the usual effect of oxygen passivation of grain boundaries which increases resistivity. This effect is, in fact, the basis of ZnO sensors. Oxygen adsorbed to the surface of a ZnO sensor is removed by a reducing gas, releasing an electron to the ZnO lattice, which is seen as a decrease in the resistivity of the ZnO sensor.

Yamada *et al.* [89] suggest that their findings could contradict the popular model due to a difference in crystal orientation and or surface morphology of the ZnO films. To try to prove this theory the films were annealed at 100°C in air or O₃. The results are shown in table 2.12.2, Yamada *et al.* [89] state that “the results are consistent with our previous idea that the chemisorbed oxygen effectively passivates the grain boundaries and reduces the barrier height, resulting in enhancement of electron mobility”.

	Mobility (cm ² /V·s)	Carrier Concentration (x 10 ¹⁹ cm ⁻³)	Resistivity (x 10 ⁻³ Ω.cm)
as deposited	15.2	2.0	20.0
after annealing	23.4	2.7	9.7
after O ₃ treatment	36.5	5.8	2.9

Table 2.12.2. Electrical properties of undoped ZnO film after O₃ treatment. After Yamada *et al.* [89].

2.13 References

- [1] H. M. Manasevit, *J. Cryst. Growth* **55** (1981) 1-9
- [2] B. Harrison and E. H. Tompkins, *Inorg. Chem.* **1** (1962) 951
- [3] R. Didchenko, J. E. Alix and R. H. Toeniskoetter, *J. Inorg. Nucl. Chem.* **14** (1960) 35
- [4] H. M. Manasevit, *Appl. Phys. Letters* **11** (1968) 156.
- [5] H. M. Manasevit and W. I. Simpson, *J. Electrochem. Soc.* **116** (1969) 1725
- [6] G. B. Stringfellow, *J. Cryst. Growth* **68** (1984) 111-122
- [7] J. Van De Ven, G. M. J. Rutten, M. J. Raaijmakers and L. J. Giling, *J. Cryst Growth* **76** (1986) 352-372
- [8] R. L. Moon, *J. Cryst. Growth* **170** (1997) 1-10
- [9] M. R. Leys, *Chemtronics* **2** (1987) 155-16
- [10] H. Juergensen, *Mat. Sci. in Semi. Processing.* **4** (2001) 467-474. and M. J. Schurman, T. Slagaj, *Mat. Sci. and Eng.* **B43** (1997) 222-227.
- [11] A. G. Thompson, R. A. Stall, W. Kroll, E. Armour, C. Beckham, P. Zawadzki, L. Aina and K. Siepel, *J. Cryst. Growth* **170** (1997) 92-96
- [12] J. B. Mullin, S. J. C. Irvine and D. J. Ashen, *J. Cryst. Growth* **55** (1981) 92-106
- [13] K. Badeker, *Ann. Phys. (Leipzig)* **22** (1907) 749.
- [14] B. G. Lewis and D. C. Paine, *MRS Bulletin* **25** (2000) 22-27.
- [15] R. G. Gordon, *MRS Bulletin.* **25** (2000) 52-57.
- [16] R. G. Gordon, *Mater. Res. Soc. Symp. Proc.* **426**, Pittsburgh (1996) 419.
- [17] D. S. Ginley and C. Bright, *MRS Bulletin* **24** (2000) 15-18.
- [18] H. Ohta, M. Orita and M. Hirano, *J. Applied Phys.* **89** (2001) 5720-5725
- [19] Z. Y. Ning, S. H. Cheng, S. B. Ge, Y. Chao, Z. Q. Gang, Y. X. Liu, *Thin Solid Films* **307** (1997) 50-53.
- [20] J. Yin, Z. G. Liu, H. Liu, X. S. Wang, T. Zhu, J. M. Liu, *J. Cryst. Growth* **220** (2000) 281-285.
- [21] M. Ishii, S. Komuro, T. Morikawa and Y. Aoyagi, *J. Applied Phys.* **89** (2001) 3679-3684.
- [22] K. L. Narasimhan, S. P. Pai, V. R. Palkar and R. Pinto, *Thin Solid Films* **295** (1997) 104-106.
- [23] A. Mitra and R. K. Thareja, *J. Applied Phys.* **89** (2001) 2025-2028.
- [24] W. T. Lim and C. H. Lee, *Thin Solid Films* **353** (1999) 12-15.
- [25] O. Kluth, B. Rech, L. Houben, S. Wieder, G. Schope, C. Beneking, H. Wagner, A. Löffl and H. W. Schock, *Thin Solid Films* **351** (1999) 247-253.
- [26] E. Bak-Mikkelsen, R de Reus and S. Bouwstra, *J. Micromech. Microeng.* **6** (1996) 63-65.
- [27] K. Tominaga, T. Murayama, I. Mori, T. Ushiro, T. Moriga and I. Nakabayashi, *Thin Solid Films* **386** (2001) 267-270.
- [28] J. F. Chang and M. H. Hon, *Thin Solid Films* **386** (2001) 79-86.
- [29] E. Dumont, B. Dugnoille and S. Bienfait, *Thin Solid Films* **353** (1999) 93-99.

- [30] S. H. Lim, D. Shindo, H. B. Kang and K. Nakamura, *J. Cryst. Growth* **225** (2001) 208-213.
- [31] K. Ramamoorthy, C. Sanjeeviraja, M. Jayachandran, K. Sankaranarayanan, P. Bhattachary and L. M. Kukreja, *J. Cryst. Growth* **226** (2001) 281-286.
- [32] S. H. Lim, D. Shindo, H. B. Kang and K. Nakamura, *J. Cryst. Growth* **225** (2001) 202-207.
- [33] K. Nakahara, T. Tanabe, H. Takasu, P. Fons, K. Iwata, A. Yamada, K. Matsubara, R. Hunger and S. Niki, *Japan. J. Appl. Phys.* **40** (2001) 250-254.
- [34] Y. S. Choi, C. G. Lee and S. M. Cho. *Thin Solid Films* **289** (1996) 153-158.
- [35] S. Zhu, C. H. Su, S. L. Lehoczky, M. T. Harris, M. J. Callahan, P. McCarty and M. A. George, *J. Cryst. Growth* **225** (2001) 190-196.
- [36] X. Wang, S. Yang, J. Wang, M. Li, X. Jiang, G. Du, X. Liu and R. P. H. Chang, *J. Cryst. Growth* **226** (2001) 123-129.
- [37] K. Haga, M. Kamidarira, Y. Kashiwaba, T. Sekiguchi and H. Watanabe, *J. Cryst. Growth* **214/215** (200) 77-80.
- [38] Y-J. Kim and H-J. Kim, *Materials Letters* **41** (1999) 159-163.
- [39] B. Ismail, M. Abaab and B. Rezig, *Thin Solid Films* **383** (2001) 92-94.
- [40] T. Y. Ma and S. S. Lee, *J. Mat. Sci. Mat. In Elec.* **11** (2000) 305-309.
- [41] P. Nunes, B. Fernandes, E. Fortunato, P. Vilarinho and R. Martins, *Thin Solid Films* **337** (1999) 176-179.
- [42] M. L. Olvera, A. Maldonado, R. Asomoza, O. Solorza and D. R. Acosta, *Thin solid films* **394** (2001) 242-249.
- [43] B. J. Lokhande and M. D. Uplane, *Aplied Surface Science* **167** (2000) 243-246.
- [44] T. Pauporte and D. Lincot, *Electrochimica Atca* **45** (2000) 3345-3353.
- [45] A. Yamada, B. Sang and M. Konagai, *Aplied Surface Science* **112** (1997) 216-222.
- [46] K. Kaiya, N. Yoshii, N. Takahashi and T. Nakamura, *J. Mat. Sci. Letters* **19** (2000) 2089-2090.
- [47] Z. Zhaochun, H. Baibiao, Y. Yongqin, C. Deliang, Q. Xiaoyan and J. Minhua, *Rare Metals* **19** (2000) 183-186.
- [48] S. Suh, L. A. Minea and D. M. Hoffman, *J. Mat. Sci. Letters* **20** (2001) 115-118.
- [49] Y. Natsume and H. sakata, *J. Mat. Sci. Mat. In Elec.* **12** (2001) 87-92.
- [50] M. Yoshino, W. W. Wenas, A. Yamada, M. Konagai, and K. Takahashi, *Japan. J. Appl. Phys.* **32** (1993) 726-730.
- [51] S. Y. Myong, S. J. Baik, C. H. Lee, W. Y. Cho and K. S. Lim, *Japan. J. Appl. Phys* **36** (1997) L1078-L1081.
- [52] P. Nunes, E. Fortunato and R. Martins, *Thin Solid Films* **383** (2001) 277-280.
- [53] J. Nishino, T. Kawarada, S. Ohshio, H. Saitoh, K. Maruyama and K. Kamata, *J. Mat. Sci. Letters* **16** (1997) 629-631.

- [54] S. Muthukumar, C. R. Gorla, N. W. Emanetoglu, S. Liang and Y. Lu, *J. Cryst. Growth* **225** (2001) 197-201.
- [55] Y. Kashiwaba, F. Katahira, K. Haga, T. Sekiguchi and H. Watanabe, *J. Cryst. Growth* **221** (2000) 431-434.
- [56] W. W. Wenas, A. Yamada and K. Takahashi, *J. Applied Phys.* **70** (1991) 7119-7123.
- [57] Y. Natsume, H. Sakata and T. Hirayama, *Phys. Stat. Sol.*, **148** (1995) 485.
- [58] K. Kobayashi, T. Mastubara, S. Matsushima, S. Shirakata, S. Isomura and G. Okada, *Thin Solid Films* **266** (1995) 106-109.
- [59] N. F. Cooray, K. Kushiya, A. Fujimaki and I. Sugiyama, *Solar Energy Materials and Solar Cells* **49** (1997) 291-297.
- [60] C. K. Lau, S. K. Tiku and K. M. Lakin, *J. Electrochem Soc.* **127** (1980) 1843-1847.
- [61] P. J. Wright, R. J. M. Griffiths and B. Cockayne, *J. Cryst. Growth* **66** (1984) 26-33.
- [62] J. Auld, D. J. Houlton, A. C. Jones, S. A. Rushworth, M. A. Malik, P. O'Brien and G. W. Critchlow, *J. Mater. Chem* **4** (1994) 1249-1253.
- [63] D. Pier and K. Mitchell, proceedings of the 9th European Photovoltaic Solar Energy Conference, Kluwer Academic, Dordrecht, Netherlands (1989) 488.
- [64] W. Wenas, A. Yamada, M. Konagai and K. Takahashi, *Jpn. J. Appl. Phys.* **30** (1991) L441-L443.
- [65] T. Minami, H. Sonohara, S. Takata and H. Sato, *Jpn. J. Appl. Phys.* **33** (19994) 743-746.
- [66] W. Wilson, W. Wenas, A. Yamada, M. Konagi and K. Takahashi, *Jpn. J. Appl. Phys.* **33** (1994) L283-L285.
- [67] S. Oda, H. Tokunaga, N. Kitajama, J. Hanna, I. Shimizu and H. Kokado, *Jap. J. App. Phys.* **24**, 12, (1985) 1607-1610.
- [68] B. Hahn, G. Heindel, E. Pschorr-Schoberer and W. Gebhardt, *Semicond. Sci. Technol* **13** (1998) 788-791.
- [69] B. Hahn, H. Preis, M. Schindler, T. Reisinger and W. Gebhardt, *J. Cryst. Growth* **179** (1997) 415-422.
- [70] V. Sallet, C. Thiandoume, J. F. Rommeluere, A. Lusson, A. Riviere, J. P. Riviere, O. Gorochoy, R. Triboulet and V. Munoz-Sanjose, *Mat. Letters* **53** (2002) 126-131
- [71] C. Kirchner, T. Gruber, F. Reuss, K. Thonke, A. Wang, C. Giessen and M. Heuken, *J. Cryst. Growth* **248** (2003) 20-24.
- [72] Material data safety sheet for DEZn issue (13th March 2000), Epichem Ltd Power Road, Bromborough, Merseyside. Material data safety sheet for n-butanol from Applied Research Institute, Newtown, CT. Applied Research Products Ltd. (21st Jan. 1998)
- [73] G. E. Coates and D. Ridley, *J. Chem. Soc.* (1965) 1870-1877
- [74] B. Cockayne, P. J. Wright and A. J. Armstrong, *J. Cryst. Growth* **91** (1988) 57-62.
- [75] E. C. Ashby, G. F. Willard and A. B. Goel, *J. Org. Chem.* **44** (1979) 1221-1232.

- [76] S. Tamura, T. Ishida, H. Magara, T. Mihara, S. Mochizuki and T. Tatsuta, *Applied Surface Science* **169-170** (2001) 425-427
- [77] S. Fujita, A. Tanabe, T. Sakamoto, M. Isemura and S. Fujita, *J. Cryst. Growth* **93** (1988) 259.
- [78] S. J. C. Irvine and J. B. Mullin, *J. Cryst. Growth* **79** (1986) 371.
- [79] A. P. Roth and D. F. Williams, *J. Electrochem. Soc.*, **128** (1981) 2784
- [80] S. Fujita, A. Tanbe, T. Sakamoto, M. Isemura and S. Fujita, *J. Cryst. Growth* **93** (1988) 259
- [81] G. Yu, X. W. Fan, J. Y. Zhang, B. J. Yang, X. Zhao, D. Shen and Y. M. Lu, *J. Cryst. Growth* **196** (1999) 77-82.
- [82] Y. Fujita, *J. Cryst. Growth* **221** (2000) 382-387.
- [83] A. Yoshikawa, *Physica B* **185** (1993) 50.
- [84] S. J. C. Irvine, M. U. Ahmed and P. Prete, *J. Electron. Mater* **27** (1998) 763.
- [85] M. U. Ahmed, P. Prete, S. J. C. Irvine, A. Stafford, L. M. Smith, A. C. Jones and S. A Rushworth, *J. Cryst. Growth* **184/188** (1998) 429.
- [86] M. U. Ahmed and S. J. C. Irvine, *J. Elect. Mat.* **29** (2000) 169-172.
- [87] M. Shimizu, H. Kamei, M. Tanizawa, T. Shiosaki and A. Kawabata, *J. Cryst. Growth* **89** (1988) 365-370.
- [88] P. R. Krchnavek, H. H. Gilgen, J. C. Chen, P. S. Shaw, T. J. Licata and R. M Osgood, *J. Vac. Sci. Technol.* **B5** (1987) 20.
- [89] A. Yamada, W. Wenas, M. Yoshino, M. Konagai and K. Takahashi, *Jpn. J. Appl. Phys.* **30** (1991) L1152-L1154

Chapter Three: Design and construction of MOCVD system

3.1 Introduction

The deposition of ZnO thin films for this research was to have been carried out on a commercially built oxide CVD reactor with facilities for doping. However, due to financial constraints it became clear that the reactor would not be available. With this in mind an old horizontal MOCVD research reactor was refurbished and a MOCVD gas handling system constructed around it.

The process of designing and building the whole MOCVD system has been of huge advantage for understanding the growth process and solving equipment related deposition problems. The MOCVD system was also used for the growth of cadmium oxide on another research project that ran concurrently with this one.

This chapter describes the design and construction processes carried out to produce a fully functioning thin film deposition system. The reasoning behind the design of the gas handling system and the exhaust scrubber is explained. A more accurate method of describing the actual temperature of the substrate surface as opposed to the susceptor temperature is demonstrated. Finally the considerations in choosing a light source for the photoassisted experiments and the setup of the *in situ* laser reflectance are discussed.

3.2 Designing the MOCVD System

A number of steps needed to be carried out to produce a MOCVD system; firstly the old reactor had previously been used to grow zinc telluride and needed thoroughly cleaning. A gas flow layout, from the bubblers to the exhaust, needed to be designed and constructed, and within this arose the need to recalibrate some Hastings mass flow controllers (MFCs) that had previously been used with hydrogen carrier gas. The UV lamp, for the photoassisted growth, needed to be specified and ordered and the *in situ* analytical techniques decided on and sourced. A scrubber system to cope with the un-oxidized metals, especially cadmium in the

exhaust gases was designed. This chapter addresses the design and construction of these specified components.

The reaction tube was a two piece quartz unit consisting of; an outer tube held in place by metal end plates, a removable inner tube onto which the susceptor was mounted. The reaction tube, which had previously been used for depositing ZnTe, was thoroughly cleaned. The quartz tubes were etched in aqua regia and the metal end plates polished using a carborundum paste. The reaction tube is shown in figures 3.2.1. and 3.2.2.

For the MOCVD of ZnO it is appropriate that the precursors be transported separately in vapor form, to avoid prereaction, and arrive at the reaction chamber where they then mix and flow over a heated substrate. The configuration of the gas handling system was designed around the reaction tube secured in the cabinet.

The specifications for the gas handling system were such that the switching of the flows through the bubblers needed to be electronic. This allowed the isolation of the bubblers automatically if needed and also ensured a smooth transition between the nitrogen carrier gas and carrier gas/precursor flow. The window purge flow and total precursor flows were designed in such a way that the two flows were balanced at any precursor concentration. This helped maintain a laminar flow of the precursor's whilst passing over the substrate. The precursor inlet was designed to provide even mixing on entering the reaction tube, see Figure 3.2.3. Combining the precursors in this way allows the best possibility of a homogenous mixture reaching the substrate. It also ensured any prereaction products would be within the reaction tube and not the pipe-work.

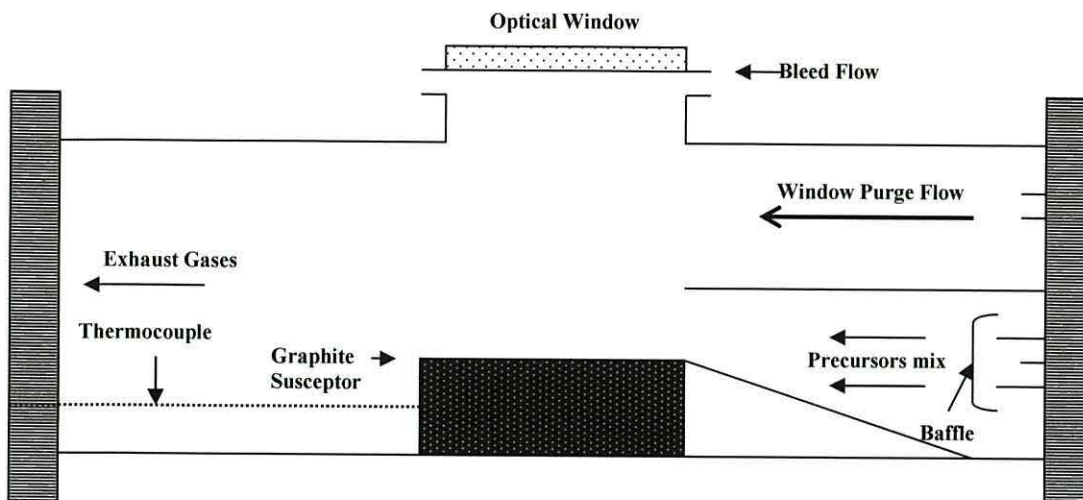


Fig. 3.2.1. The quartz reaction tube. The quartz optical window allows the monitoring of thin film growth by interferometry as well as allowing irradiance of the substrate surface by the UV/Vis light. The window is kept free from deposit by a bleed flow of the carrier gas which is passed over the window. The window purge flow also acts to prevent deposit on the optical window.

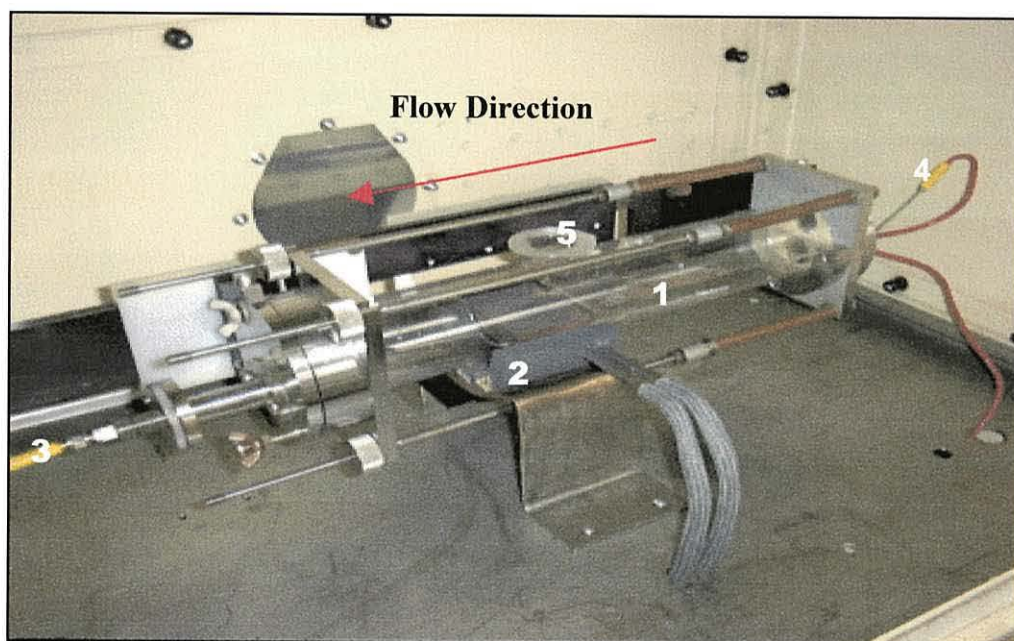


Fig. 3.2.2. The reaction tube as situated in the cabinet. (1) quartz tube, (2) heater unit (resistance), (3) thermocouple located inside susceptor, (4) thermocouple located at inlet and (5) port for optical window.

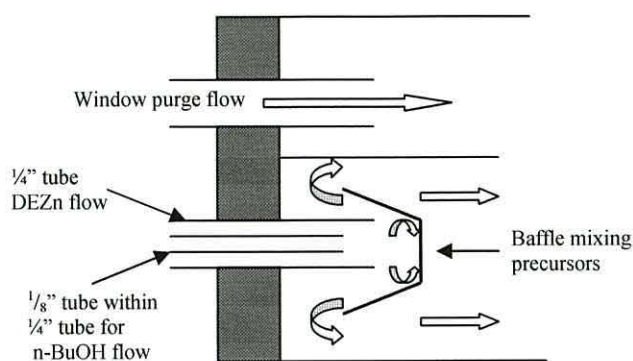


Fig. 3.2.3. Precursor inlet designed to maximize mixing at latest point to reduce prereaction.

In order to help design a gas handling system that would facilitate these requirements a literature search was carried out into the various configurations used by other research groups. Some examples of which are shown in figure 3.2.4.

It was decided that a vent/run system as shown in figure 3.2.4. (a) would not be necessary for the research being undertaken. However the ability to dilute and effectively balance the flows of the precursors, as shown in figure 3.2.4. (b), was essential to the reaction tube design. All systems have a facility to apply a vacuum to the gas lines. This serves a number of purposes; to remove air when the reaction tube has been loaded, removing precursors from the lines after a deposition and to vacuum down lines before removal and after refitting of bubblers. In low pressure MOCVD the vacuum pump also controls the pressure within the reaction tube.

The flow paths and rates needed to be fully controllable in order to alter parameters for different growth runs and for safety. The pipe-work used within this system was the standard $\frac{1}{4}$ inch electro-polished stainless steel tubing from Dockwyler Ltd. The tubing was shaped and cut by hand before being joined together using Swagelok fittings and welding where necessary.

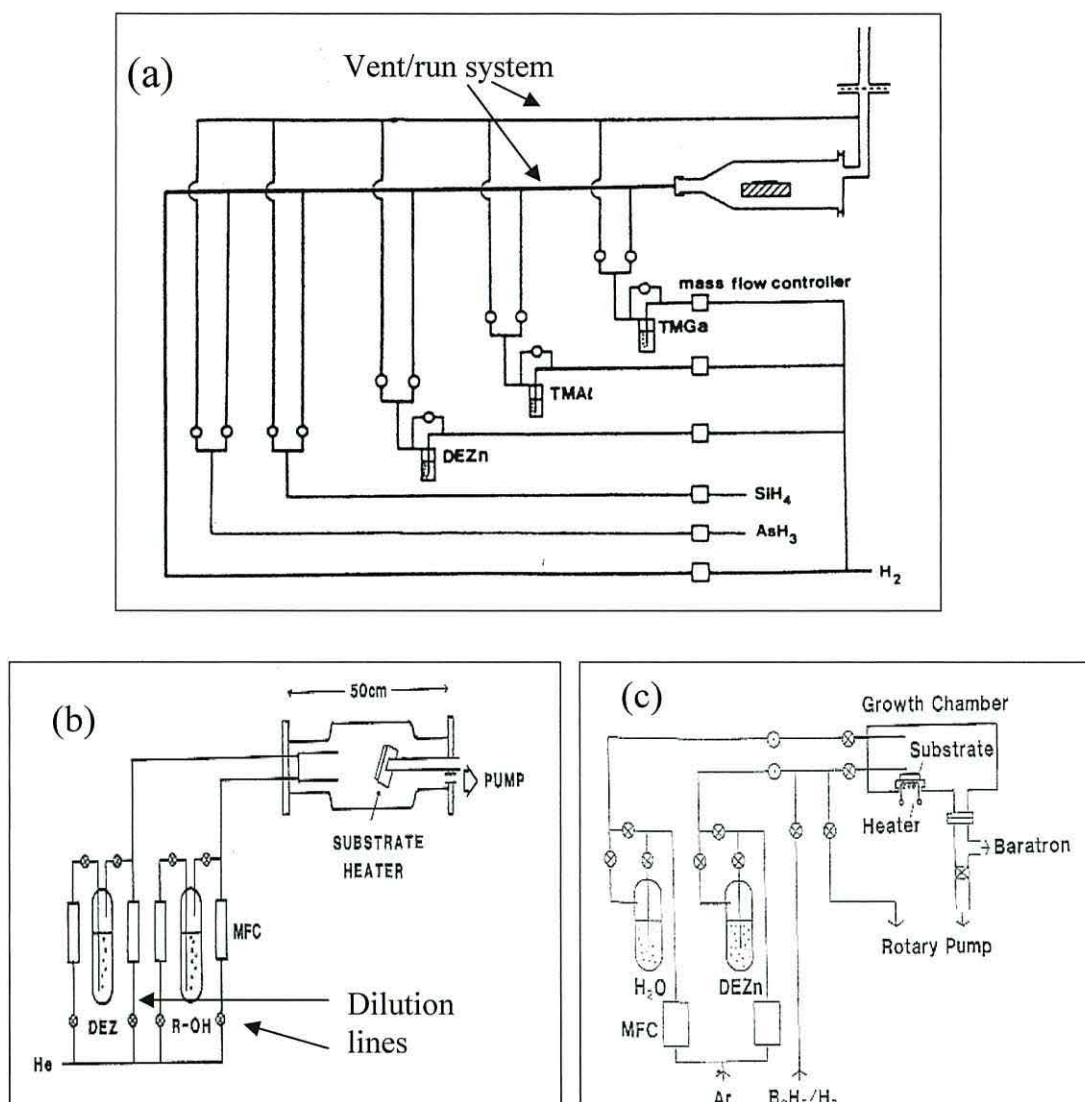


Fig. 3.2.4. Schematic diagrams of MOCVD systems (a) MOCVD system with multiple lines leading to a horizontal reactor. Features a vent/run system for quick switching between precursors. After M. Leys [1]. (b) MOCVD system with two lines and no vent/run. Has the capability of providing a balanced flow mixing within the reactor. After S. Oda *et al.* [2]. (c) MOCVD system again with two lines but no vent/run or balancing of flows. Again the precursors are injected separately into the reaction tube. After W. Wenas *et al.* [3].

The system had three flows entering the reaction tube; a window flow which acted to avoid deposition on the optical port, a metalorganic precursor flow and an oxygen precursor flow. MFCs managed the flow rates of each of these lines and pneumatic and manual valves allowed lines to be opened or closed as required. Figure 3.2.5. is a schematic of the final design of the gas flow panel.

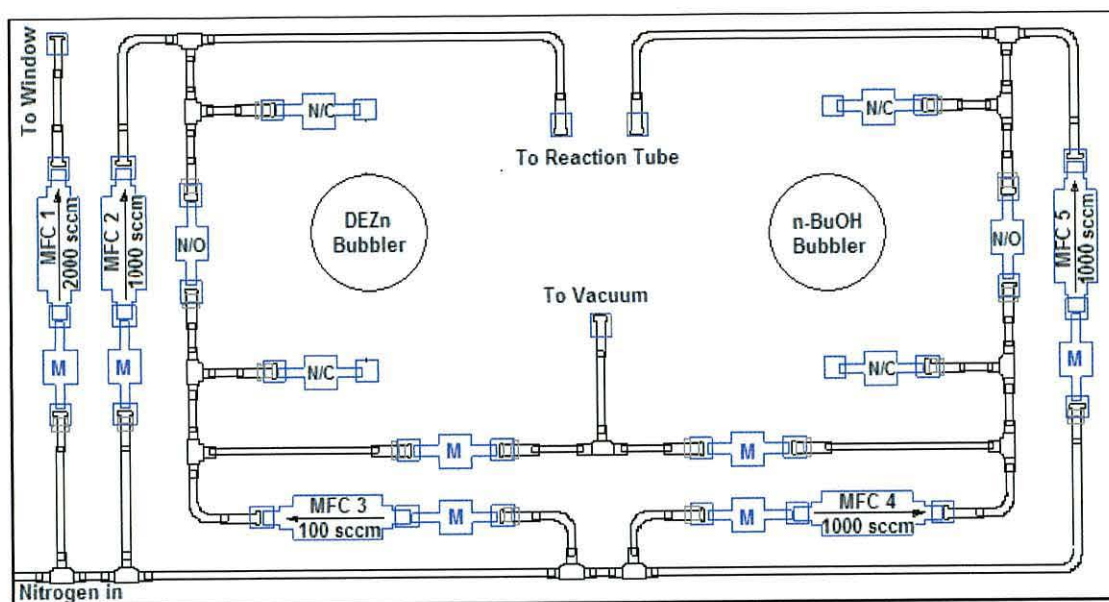


Fig. 3.2.5. Schematic of gas flow panel providing the carrier gas to the bubblers and onto the reaction tube. The lines can be degassed via a vacuum pump. N/C are normally closed pneumatic valves, N/O are normally open pneumatic valves, M are manual valves, MFCs are labeled with their maximum flows in sccm.

The MFCs are labeled with their maximum flow rate in standard cubic centimeters per minute (SCCM), they are accurate to within 1% of full scale. The MFC capacities and the flow they control are shown in table 3.2.1. The panel was designed so that the metalorganic/oxygen precursor ratio could be controlled. This was completed by incorporating a dilution flow system into each precursor line so the flow rates from the two lines were always balanced.

MFC Maximum Flows (SCCM)	Flows Controlled
2000	Window flow
1000	Metalorganic precursor dilution flow
1000	Oxygen precursor dilution flow
100	Metalorganic bubbler flow
100	Oxygen bubbler flow

Table. 3.2.1. The maximum flows (sccm) of each MFC

The manual valves are depicted by blue squares; they allow parts of the system to be isolated during the degassing procedure. The pneumatic valves are operated remotely from a control panel enabling fast switching between bubbler flows on and off. The pneumatic valves also provided a remote safety feature allowing the isolation of the bubblers. The finished gas panel and bubblers are shown in figure 3.2.6.

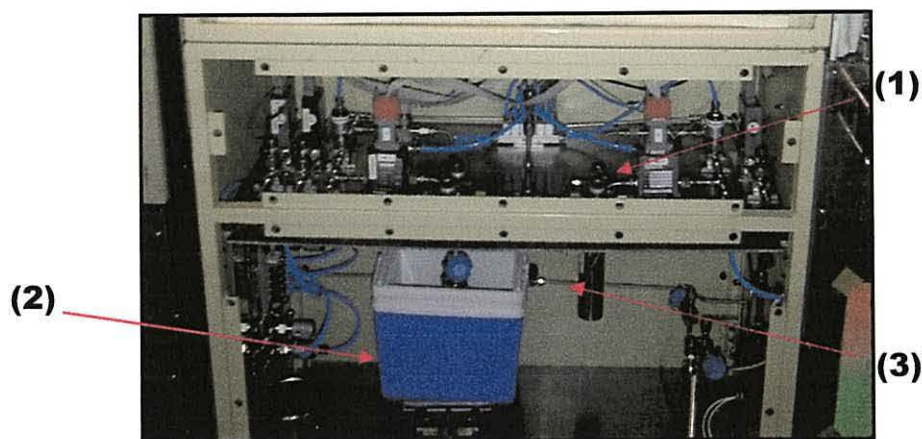


Fig. 3.2.6. The gas flow panel and bubblers. (1) a MFC, (2) the ice box surrounding the metalorganic bubbler, and (3) the oxygen bubbler kept at room temperature.

A resistance heater unit was fitted, as close as possible to the quartz reaction tube, beneath the graphite susceptor. A thermocouple located within the susceptor linked to a Eurotherm allowed monitoring of susceptor temperature. The Eurotherm enabled the programming of various temperature programs. A second thermocouple was used to monitor the temperature of the precursor mixing zone knowledge of which is useful when considering prereactions.

A major concern when designing a MOCVD system is the handling of the exhaust gases. This system was designed to deposit both zinc oxide and cadmium oxide. It was expected that the most toxic by-product of the zinc oxide deposition would be zinc oxide powder. Zinc oxide powder is found in many commercial products including baby cream. When ingested in the powder form it can cause what's known as the zinc shakes. Cadmium oxide in the powder form is a highly toxic carcinogen.

Following the conventional approach to handling metalorganic products an activated carbon trap was designed. This employed a length of removable pipe filled with activated carbon, which has the property of adsorbing large quantities of gases. It was then possible to change the contents of this “trap” at regular intervals. A schematic of the MOCVD system, including the trap is shown in figure 3.2.7.

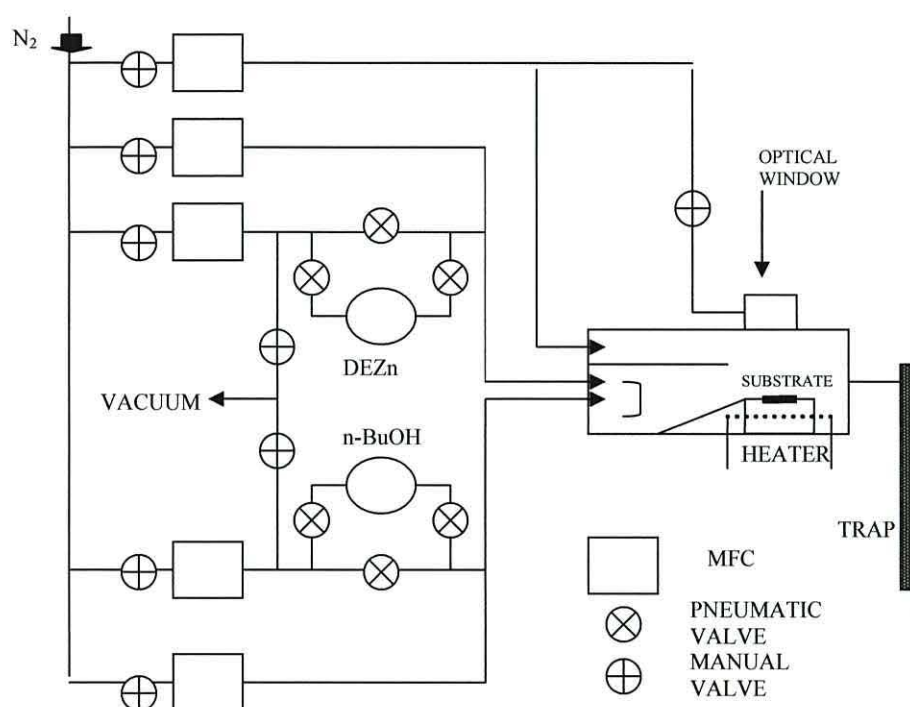


Fig. 3.2.7. Schematic of MOCVD system.

3.3 Correcting for substrate temperature

Due to the location of the thermocouple, within the susceptor, there was an uncertainty as to the actual temperature at the substrate surface. This was investigated by using an ingenious method of measuring the temperature of the substrate surface. By shaping both a piece of indium wire (m.p. 156.6°C) and a piece of tin wire (m.p. 231°C) into a ball and placing them onto a substrate it was possible, ramping the temperature slowly, to observe the balls crumple as they reached their melting points. Using room temperature as a third point of reference it was possible to produce a graph of the actual substrate surface temperature versus the thermocouple temperature, shown in figure 3.3.1.

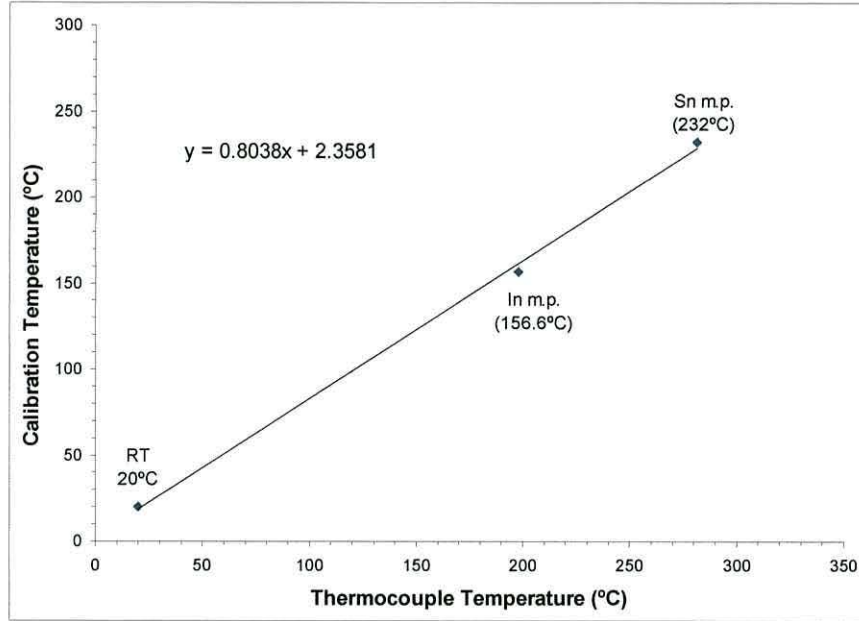


Fig. 3.3.1. Calibration of actual substrate surface temperature by observing thermocouple reading when melting points of indium and tin wire are reached.

3.4 Calculating the Precursor Partial Pressures

The two stainless steel bubblers were suspended below and attached to the gas panel. One contained DEZn, supplied by Epichem Ltd, and was maintained at 0°C using an ice bath. This reduced the saturated vapor pressure from 15.9 Torr at RT to 3.6 Torr. The other bubbler contained n-butanol sourced from Aldrich and was kept at room temperature (V_p 5 Torr). The n-butanol was transferred into an empty bubbler under nitrogen using modified Schlenk line conditions. The partial pressure required for any particular deposition was obtained using equations 3.4.1. and 3.4.2.

$$[C] = \text{SVP} \cdot F_{\text{Bubbler}} / P_{\text{Reactor}} \cdot F_{\text{Total}} \quad (3.4.1.)$$

Rearranging to give:

$$F_{\text{Bubbler}} = [C] \cdot P_{\text{Reactor}} \cdot F_{\text{Total}} / \text{SVP} \quad (3.4.2.)$$

Where SVP is the saturated vapor pressure (Torr), [C] is the concentration in the reactor expressed as a partial pressure in atm, P is the reactor pressure (atmospheric

pressure in Torr at the time of experiment), F_{total} is the total flow in sccm of both precursors and F_{bubbler} is the bubbler flow in sccm.

As discussed in chapter 2.2 Leys [1] showed that the partial pressure, (concentration) of the precursors for MOCVD, is mostly in the order of 10^{-4} atm. The capacities of the MFCs (total sccm) were chosen with this precursor partial pressure in mind. For example a 1:1, II/VI, reaction gives the following flow rate calculation.

For DEZn at 0°C and 760 Torr.

$$F_{\text{bubbler}} = \frac{(2 \times 10^{-4}) \times 760 \times 500}{3.6}$$

$$F_{\text{bubbler}} = 21.1 \text{ sccm}$$

For n-BuOH at 20°C and 760 Torr.

$$F_{\text{bubbler}} = \frac{(2 \times 10^{-4}) \times 760 \times 500}{5}$$

$$F_{\text{bubbler}} = 15.2 \text{ sccm}$$

Using these bubbler flows, as an example, the dilution flows would be set so that the total flow of each precursor entering the reactor was 250 sccm. In this way the two flows were effectively balanced on mixing at the baffle.

3.5 The UV/Vis Light Source

One of the unique aspects to this research, into zinc oxide thin films, was the photoassisted growth mechanism. This being the case, one of the most important pieces of equipment was the UV/Vis light source, the specifications for which are outlined as follows.

- The spectral intensity of the selected light source needs to be uniform across the wavelength range to stimulate photo-catalysis.
- The irradiation intensity needs to be tunable over a range of ca. 5 to 90 mW/cm² [4].
- The irradiation needs to be filtered over wavelengths absorbed by the metalorganic and oxygen precursors in the gas phase.

- The light source needs to be easily directed onto the substrate through the optical window of the reactor.
- Safety issues need to be considered.

Specifications and quotes were gained for a number of UV lamps from Hamamatsu in Japan, Photonics Solutions in Edinburgh and L. O. T.- Oriel based in Surrey. The model most suited to the purposes of this research was a 450 W Xe lamp from Photonics Solutions.

As discussed in chapter two, in order to exclude the possibility of photolysis of the precursors in the gas phase, the light source needed to be filtered of wavelengths absorbed by the precursors. The absorption spectra of the two precursors; DEZn from Rothschild [5] and n-butanol are shown in figure 3.5.1. The main absorbance for both precursors lies below 280 nm.

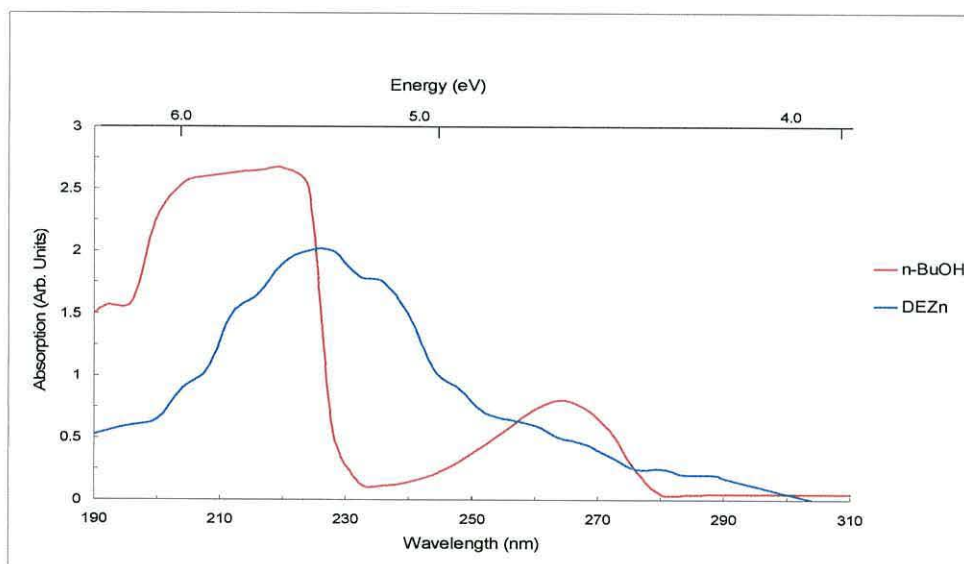


Fig. 3.5.1. DEZn and n-BuOH absorption versus wavelength/energy. The DEZn data was adapted from Krchnavek *et al.* [5].

The 450 W Xe lamp provided a power intensity of up to 100 mW/cm² (between 280nm and 510nm). It also delivered its irradiance via a one meter flexible fiber-optic light guide, which allowed easy access to the optical port of the reactor

without using up valuable space in the reactor cabinet. UV arc lamp sources emit invisible, intense UV radiation which is harmful to human eyes therefore the appropriate protective goggles were worn during its operation. A filter was provided with the lamp to shut out any wavelengths shorter than 280nm which would be absorbed by the precursors in the gas phase.

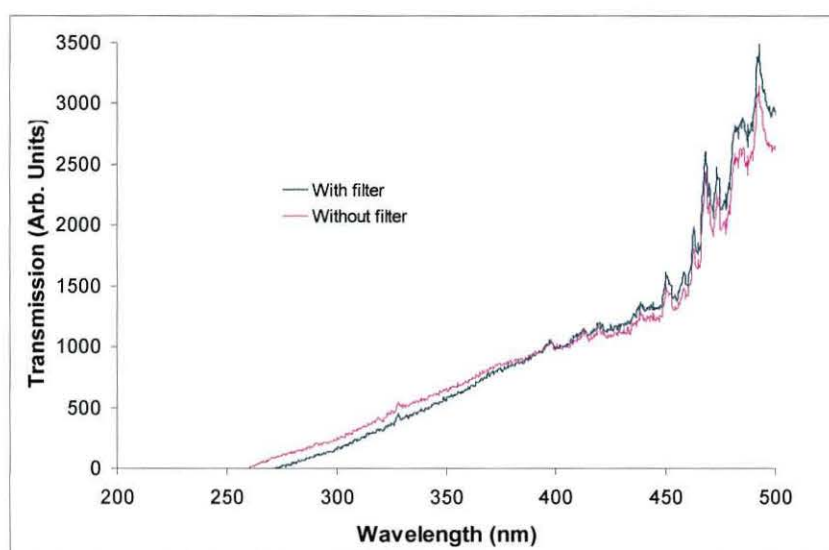


Fig. 3.5.2. Transmission (arb. units) versus wavelength (nm) of unfiltered and filtered Photonics Solutions 450 W Xe UV/Vis lamp.

Figure 3.5.2. shows that the filtered light source will not provide high enough energy to promote any gas phase photolysis in the precursors. Figure 3.5.3. gives the transmission of the UV/Vis lamp at different power settings along with typical absorption range of ZnO.

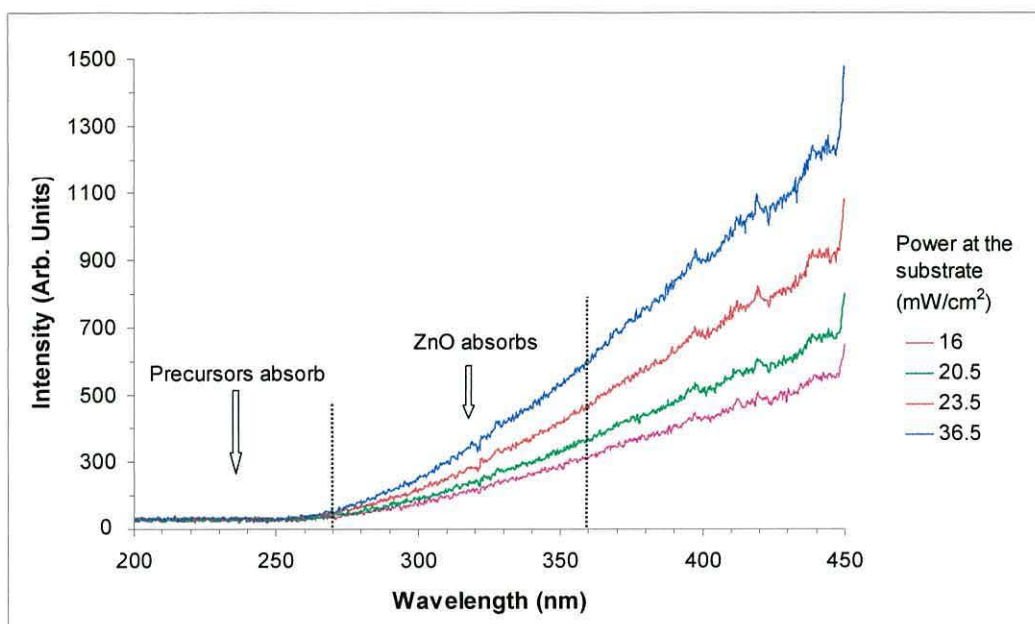


Fig. 3.5.3. Transmission (Arb. units) at different power settings (mW/cm^2) versus wavelength (nm) of filtered Photonics Solutions 450 W Xe UV/Vis lamp.

3.6 *In situ* Interferometry

As discussed in chapter 2 an *in situ* interferometer was used to monitor growth of the films in real-time. The first version of the interferometer was a unit designed by a former PhD student. This was a compact unit designed to “bolt” onto Aixtron production MOCVD systems. The unit, figures 3.6.1. and 3.6.2. was comprised of a red laser (635 nm and 3mW) mounted within a brass casing. The unit was situated above the optical window of the reactor.

The path of the laser was as follows; it passed through a beam splitter and was reflected normal to the substrate surface. Then the reflected beam was then directed by the beam splitter to a photodetector whose signal was logged as intensity versus time on a PC. As the thin films grew their surfaces produced a second reflection which interfered constructively or destructively, depending on film thickness, with the substrates reflection. This data was then displayed as an interference oscillation on the PC.



Fig. 3.6.1. The interferometer above the reaction tube.

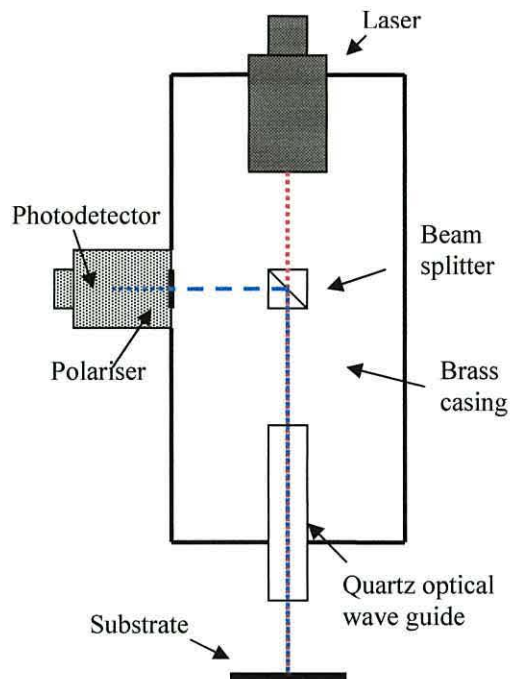


Fig. 3.6.2. Schematic of the interferometer.

However, there were a number of problems with this system:

- The TTL laser encased in the brass unit was unstable due to temperature fluctuations within the cabinet; this meant it was not possible to get a stable background signal before deposition.
- Because of the layout of the reactor the susceptor had to be removed for the loading of each substrate; for each run the interferometer had to be laboriously aligned to the new position of the substrate. This proved extremely time consuming.
- Access for the optical light guide of the UV/Vis lamp was restricted by the interferometer.

Some time into the research it was decided to change the interferometer setup to solve the above problems. The solution was to construct a rail above the reactor to

house the laser and photodetector and to direct the beam using mirrors. The setup is shown in figures 3.6.3. and 3.6.4. The design shown in figures 3.6.3. and 3.6.4. allowed: easy alignment for each substrate, moved the laser away from the hot zone and provided optimum access for the UV/Vis light guide. An intensity stabilized constant wavelength laser could now be used as the beam was chopped externally.

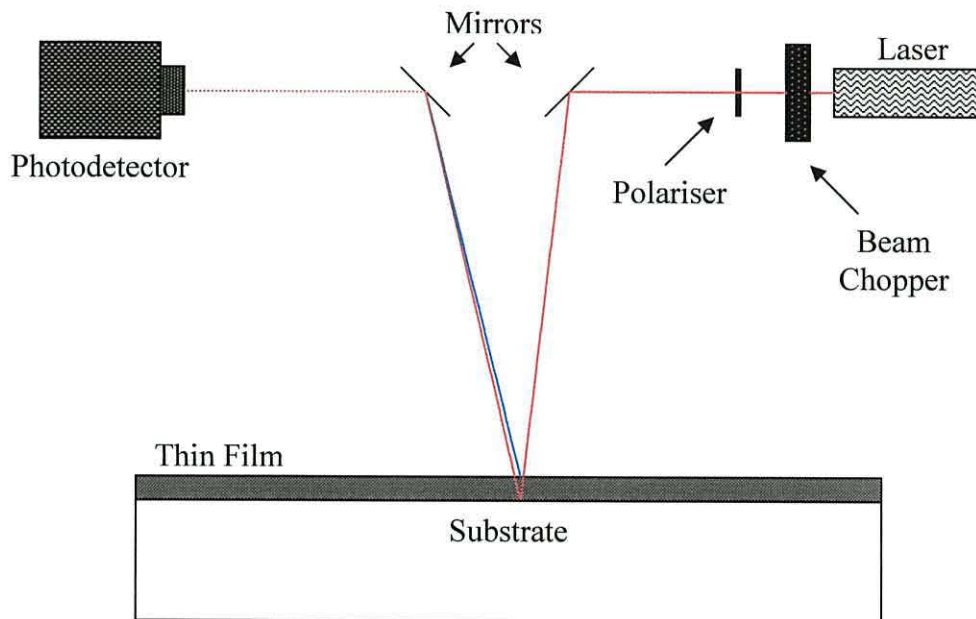


Fig. 3.6.3. Schematic representation of in situ Interferometry monitoring of thin film growth.

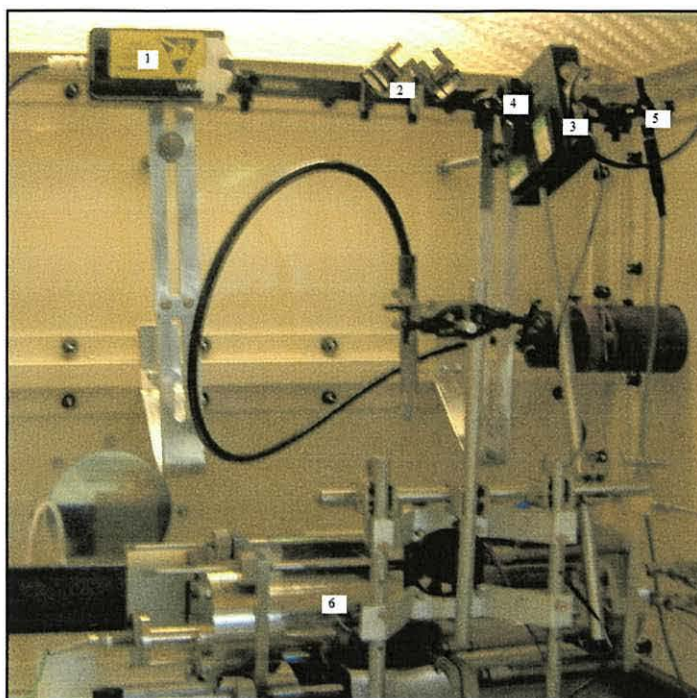


Fig. 3.6.4. Actual interferometer layout on MOCVD system. (1) The photodetector, a 1 cm² silicon photodetector connected to a lock-in amplifier. (2) The mirrors, which direct the laser beam onto the substrate surface and the returning signal to the photodetector. (3) The beam chopper, linked to the lock-in amplifier; it is set to give a 1000Hz chopped beam. This effective on/off pattern of the beam allows changes in the background to be taken into account. (4) Shows the polarising material which allows the intensity of the laser beam to be modified to avoid saturation of the photodetector. (5) The laser a 635nm red 5mW laser, whose intensity can be changed using a Melles Griot diode laser driver. (6) The quartz reactor tube housing the substrate.

3.7 Data Logging

The data logging system was built in the department according to certain specifications. As shown in figure 3.7.1. the program displayed: the flow rates of each MFC, the substrate and inlet temperature, and the signal intensity from the interferometer. Data points were taken once a second and the overall deposition time displayed.

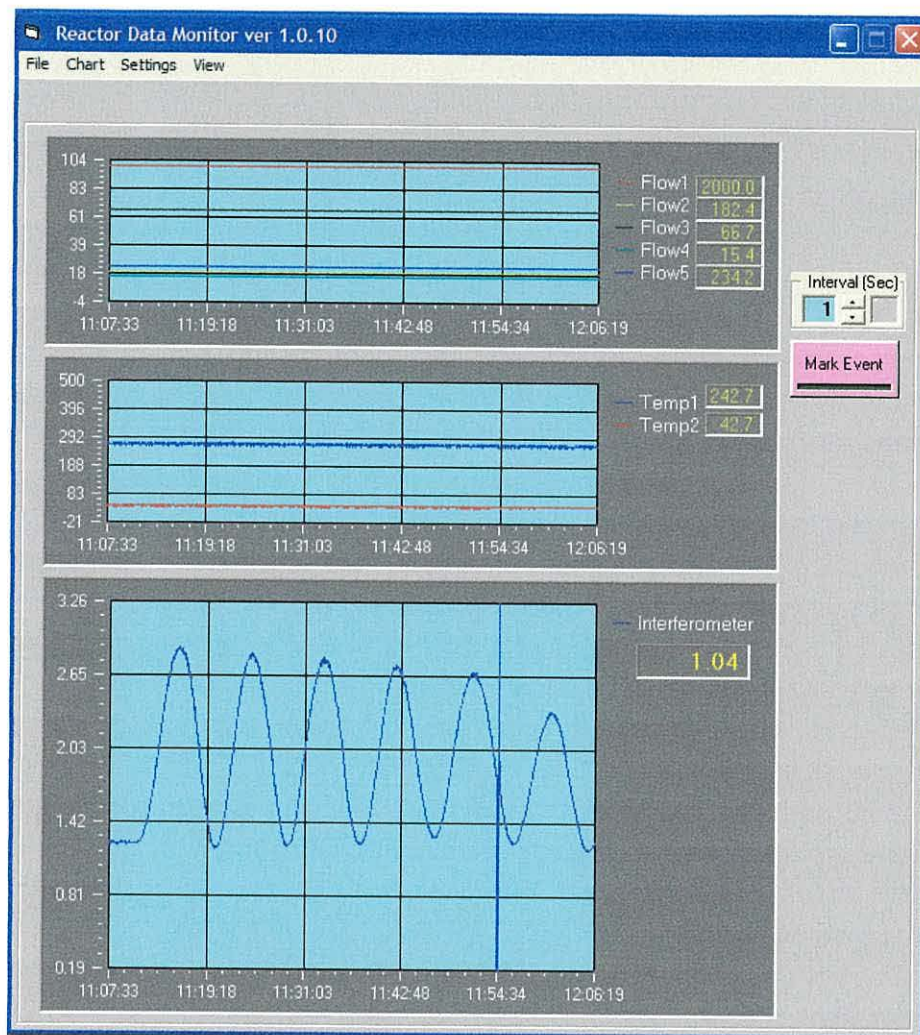


Fig. 3.7.1. The monitoring program display. The top chart shows the flow rates (sccm) of all 5 MFCs as a function of time. The middle chart displays the susceptor temperature (blue line) and the inlet temperature (red line) as a function of time. The bottom chart displays the reflectance of the interferometer laser as a function of time.

3.8 Experimental procedures

Between each growth run the inner quartz tube, which held the susceptor and the two Pyrex deflectors, were soaked in aqua regia and then in water before being rinsed with methanol and thoroughly dried in a heated cabinet. The procedure was applied to the outer quartz tube after every five runs or if heavy deposition was observed on it. The ZnO films were deposited onto one inch square Corning 1737 (aluminosilicate) glass substrates. These were ultra-sonically cleaned in deionised water for ten minutes, rinsed twice with methanol and dried with nitrogen.

The aluminosilicate glass was supplied by Delta Technologies Ltd and was manufactured by a draw fusion process which, the company claims, produces glass with virtually untouched surfaces and a low surface roughness. A typical aluminosilicate composition is given in table 3.8.1.

Compound	SiO ₂	CaO	Al ₂ O ₃	B ₂ O ₃	Na ₂ O
Percentage	55.0	21.0	10.4	7.0	1.0

Table. 3.8.1. A typical aluminosilicate glass substrate composition.

An alternative substrate to aluminosilicate glass is soda lime glass. This is the most common type of window glass. It has a similar refractive index to aluminosilicate glass of 1.51 but approximately a three times higher thermal coefficient of expansion. This latter fact, along with the benefits of the drawn fusion process, makes the aluminosilicate glass a better choice for higher temperature depositions.

Once the substrate was loaded on the susceptor and the reactor closed, the interferometer was then aligned. This was carried out without the quartz optical window in place to be certain the substrate was responsible for the returning signal. With the interferometer aligned and the optical window in place the temperature ramp was initiated and the reaction tube degassed using an Edwards vacuum pump. An ice/water bath was prepared and the DEZn bubbler submerged in it. With the system degassed the nitrogen carrier gas flows were set and the monitoring software initiated. The system was then left for approximately two hours to reach the set point temperature. The Eurotherm indicated when the desired growth temperature was achieved and, after two hours, the DEZn was assumed to be the same temperature as the ice bath 0.5°C.

During the heating procedure the interferometer signal would decrease to about 10 % of its original level. When the temperature reached a steady state the interferometer signal would level out providing the base line for the growth. This is discussed further in chapter 5. With a constant intensity from the interferometer the

growth run conditions were noted and then the bubbler lines opened via the pneumatic valves. After an initial nucleation time, depending on the particular growth parameters, the deposition of the thin film could be observed as an increase of the signal intensity.

The reactor conditions including: substrate and inlet temperatures, MFCs status and interferometer signal could all be monitored remotely outside the laboratory via a PC. Using the interferometry as a guide, the growth run could be stopped when the films reached a particular thickness. The bubbler lines were closed and the heater switched off. The nitrogen carrier gas flows were maintained until the substrate cooled to room temperature. The substrate was then removed for analysis and the reactor prepared for the next run. The nature of the reactor made it almost impossible to carry out more than one growth run per day.

3.9 References

- [1] M. R. Leys, *Chemtronics* **2** (1987) 155-16.
- [2] S. Oda, H. Tokunaga, N. Kitajama, J. Hanna, I. Shimizu and H. Kokado, *Jap. J. App. Phys.* **24**, 12, (1985) 1607-1610
- [3] W. Wenas, A. Yamada, M. Konagai and K. Takahashi, *Jpn. J. Appl. Phys.* **30** (1991) L441-L443
- [4] G. Yu, X. W. Fan, J. Y. Zhang, B. J. Yang, X. Zhao, D. Shen and Y. M. Lu, *J. Cryst. Growth* **196** (1999) 77-82.
- [5] P. R. Krchnavek, H. H. Gilgen, J. C. Chen, P. S. Shaw, T. J. Licata and R. M Osgood, *J. Vac. Sci. Technol.* **B5** (1987) 20.

Chapter four: Techniques for Thin Film Analysis

4.1 Introduction

This chapter describes the analytical techniques carried out on the thin films deposited during the research. In some cases analytical equipment not specifically designed for thin films was utilized. In these instances some form of qualification of the procedure followed is given. It was necessary, for comparison to growth rate, to focus all the analytical techniques on the area of the thin film measured by the *in situ* interferometry.

The methodology of measuring the optical properties of the thin films using UV/Vis spectroscopy is described. An explanation of the measurement of growth rate via *in situ* interferometry followed by the analytical technique for the electrical properties of the thin films is given. Three techniques, SEM, AFM and XRD, for probing the surface morphology and crystalline structure of the thin films are detailed.

4.2 UV/Vis Measurements

One of the key properties of TCOs is their transparency in the visible wavelengths 400-750nm. A high transparency of the TCO, in this wavelength range, increases the efficiency of the photovoltaic device. For thin film photovoltaics wide bandgap TCOs such as ITO are favoured. Thin film ITO with a band gap of 3.8 eV will absorb energy of shorter than 300nm and transmit wavelengths longer than 300nm up to the plasma edge. For this reason it is important to measure the transmission spectrum of any material proposed as a TCO and make calculations as to the materials band gap energy.

In this research the transmission spectra were obtained on an ATI UNICAM UV/Vis spectrometer scanning between 190nm and 900nm. It is usual to see interference oscillations in the transmission spectrum of thin films; these can be used to measure the films thickness. However the thin films grown in this research

were of non-uniform thickness reducing the effects of interference oscillations and the transmission spectra did not allow the calculation of film thickness.

The transmission spectra were used within this research to demonstrate: an average percentage transmission above the band edge (400 – 900 nm), the effects caused by changes in the surface morphology on the transmission spectrum and to approximate the optical bandgap energy.

An approximation of the optical bandgap energy for a semiconductor of direct optical transitions is obtained using equation 4.2.1.

$$\alpha \text{ proportional to } (h\nu - E_g)^{1/2} \quad (4.2.1.)$$

Where α = absorption coefficient as a function of frequency for a direct (allowed) transition.

α is obtained from the transmission spectra by equations 4.2.2, 4.2.3. and 4.2.4.

$$\left(\frac{I}{I_0} \right) = T \quad (4.2.2)$$

$$I = I_0 e^{-\alpha d} \quad (4.2.3.)$$

$$\alpha = -\ln \frac{\left(\frac{I}{I_0} \right)}{d} \quad (4.2.4.)$$

Thus the plotting $(\alpha E)^2$ versus energy $h\nu$ and extrapolating the linear portion of the curve to the intercept with the energy axes gives the bandgap energy.

Purica *et al.* [1] show an example of this technique in figure 4.1.1. The ZnO films were prepared by single source CVD using zinc acetylacetonate $[\text{Zn}(\text{C}_5\text{H}_7\text{O}_2)_2]$ as

the source material and deposited at 360°C on glass substrates. The calculated bandgap for the sample shown in figure 4.2.1. was 3.47 eV.

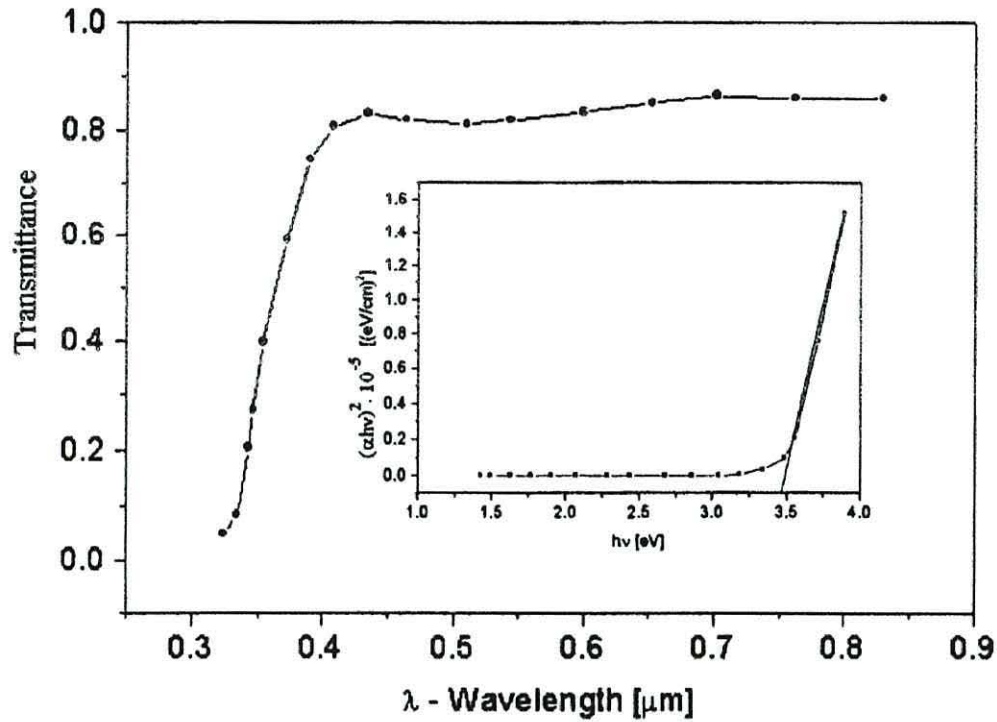


Fig. 4.2.1. Transmittance of a ZnO film and (insert) the plot of $(\alpha E)^2$ versus energy (eV). After Purica *et al.* [1].

Adjustments were made to the transmission data used in calculating the bandgap energy by this technique within the research of this thesis. To account for any small interference effects, in the transmission data, wavelengths longer than 600 nm were averaged and this average taken to be equal to zero absorption by the materials bandgap. This is based on the assumption that any loss of transmission below the bandgap energy is not resultant from bandgap absorption but from reflection, scattering or absorption by species such as free carriers.

4.3 Measuring growth rate by *in situ* Interferometry

The terms Interferometry and interferometer are both derived from the word interference. Interference is a phenomenon that occurs when waves of any kind come together, be they sound waves, light waves or ocean waves. Whenever two waves comes together at the same time and place interference will occur.

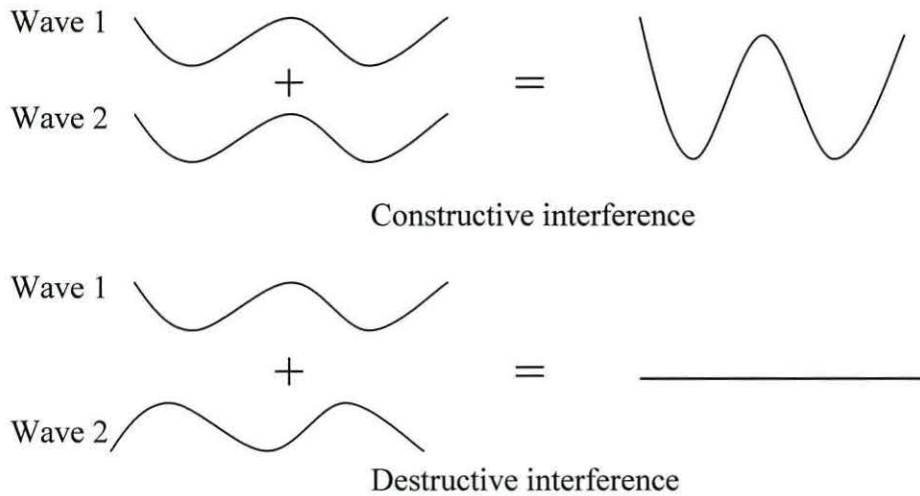


Fig. 4.3.1. Constructive and destructive interference patterns.

Interference can be seen as the adding together of two waves with each other. Depending on wave size (amplitude) and the degree to which they are in or out of step with each other (phase) they will reinforce or cancel one another (see figure 4.3.1.). In the case of laser interferometry; single wavelength light waves are reflected by the substrate surface and are then collected by a photo-detector. Any transparent film deposited on the substrate will itself reflect a certain amount of the light waves; these will then interfere with the light waves reflected of the substrate. Depending on the distance (d) between the two reflections, destructive or constructive interference will occur.

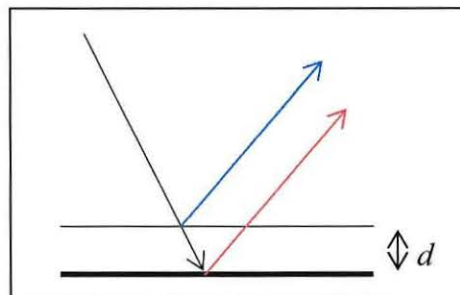


Fig. 4.3.2. The red arrow represents reflection by the substrate surface and the blue arrow reflection by the growing transparent film. Depending on the thickness (d) of the growing film the two reflections will interfere constructively or destructively to produce an interference pattern.

In the case of figure 4.3.2, for a film with no absorbance or scattering of the laser light, the interference pattern produced during thin film growth would follow that of a sinusoidal wave. In thin film laser interferometry the signal is recorded per second, each second being equal to a certain thickness of deposition, and plotted against the signal intensity. The interferogram may be plotted as reflectance as a function of film thickness as shown in figure 4.3.3.

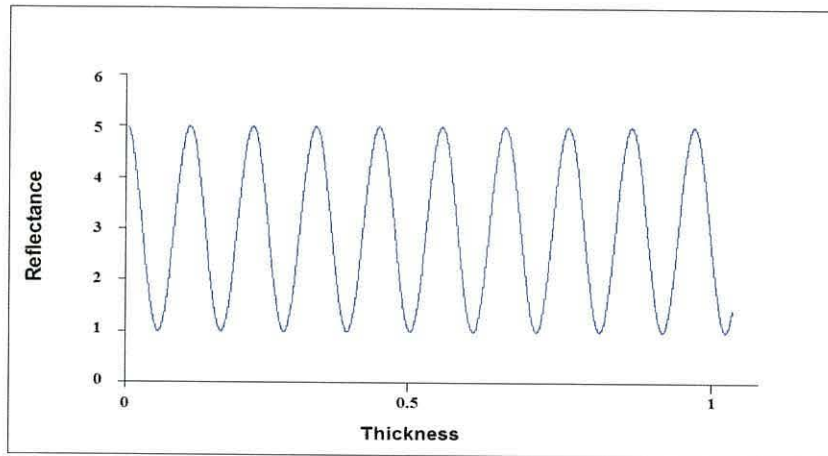


Fig. 4.3.3. Theoretical interferogram. Reflectance (Arb. Units) is plotted as a function of thickness.

Information about the film thickness (d) and therefore growth rate (GR) can be gained from the interferogram. Also, film roughening and optical properties such as the refractive index (n) and absorption coefficient can be obtained. The growth rate is calculated using equation 4.2.1.

$$GR = (\lambda/2n_f)/t \quad (4.2.1.)$$

Where GR = growth rate, λ = laser wavelength (nm), n_f = refractive index of thin film and t = duration in time of one oscillation.

For zinc oxide thin films $n_f = 1.9$ therefore, using a 635nm laser, one oscillation represents a thickness of 1671 Å. Once the thickness of the thin film is calculated,

from the number of oscillations, growth rate per unit time can be obtained. This method of measuring growth rate during deposition provides information about the reaction kinetics. The effect on the growth rate of any parameter change made during deposition can be observed. As opposed to *ex situ* growth rate measurements which rely on dividing the total thickness by the deposition time and take no account of growth rate changes during deposition.

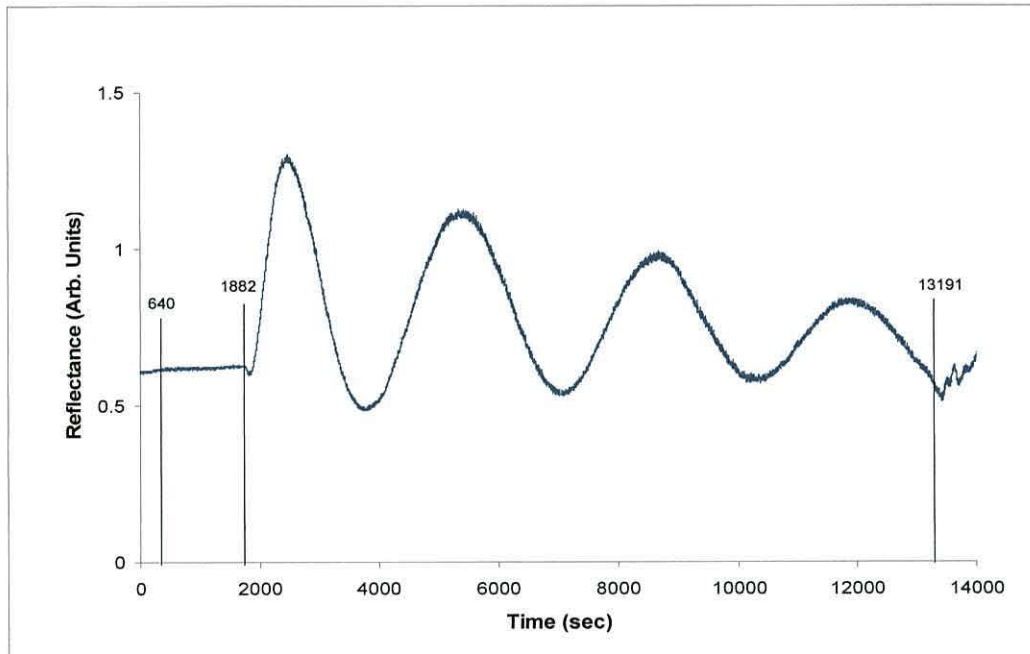


Fig. 4.3.4. Reflectance (Arb. Units) versus time (seconds) for a ZnO thin film deposited at 300°C II/VI ratio 1:1 using DEZn and n-butanol.

Figure 4.3.4. is an example of an interferogram of zinc oxide deposited by MOCVD within this research, the features to note are: the periodicity which shows the changing growth rate, the attenuation of the signal due to absorption and scattering, and the change in average signal due to roughening. The nucleation delay is shown between 640 seconds, when the precursors are set to flow, and 1882 seconds when the signal starts to change due to film growth.

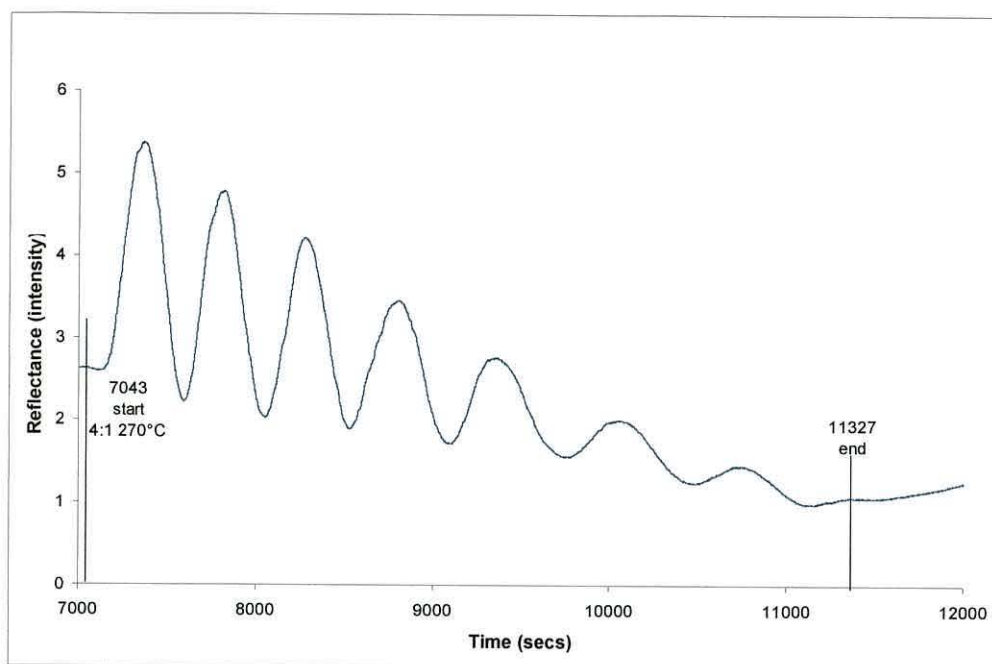


Fig. 4.3.5. Reflectance (Arb. Units) versus time (seconds) of ZnO deposited at 270°C VI/II ratio 4:1 using DEZn and n-butanol precursors.

Figure 4.3.5 is an interferogram of zinc oxide deposited under different parameters to figure 4.3.4. and serves to demonstrate the decrease in average reflectance indicating a roughening film. The growth rate of this film does not reach a steady state due to the roughening surface. Figure 4.3.6. shows how the powerful a growth monitoring tool *in situ* interferometry is. In this experiment the concentrations of the precursors are changed during growth and interferogram resolves the response of the growing film properties to these changes.

With each oscillation representing 167 nm of thin film growth the overall thickness of sample banzn062 can be calculated as approximately 2.5 μm . Throughout the growth run the average reflectance decreases gently indicating a slight roughening of the film. The attenuation of the reflectance signal decreases considerably as a result of absorbance and scattering by the growing thin film. The change in oscillation time of the reflectance signal is a clear response to varying precursor concentrations. This *in situ* monitoring technique allows, in this sample, the effects of four different concentration ratios to be examined within one experiment.

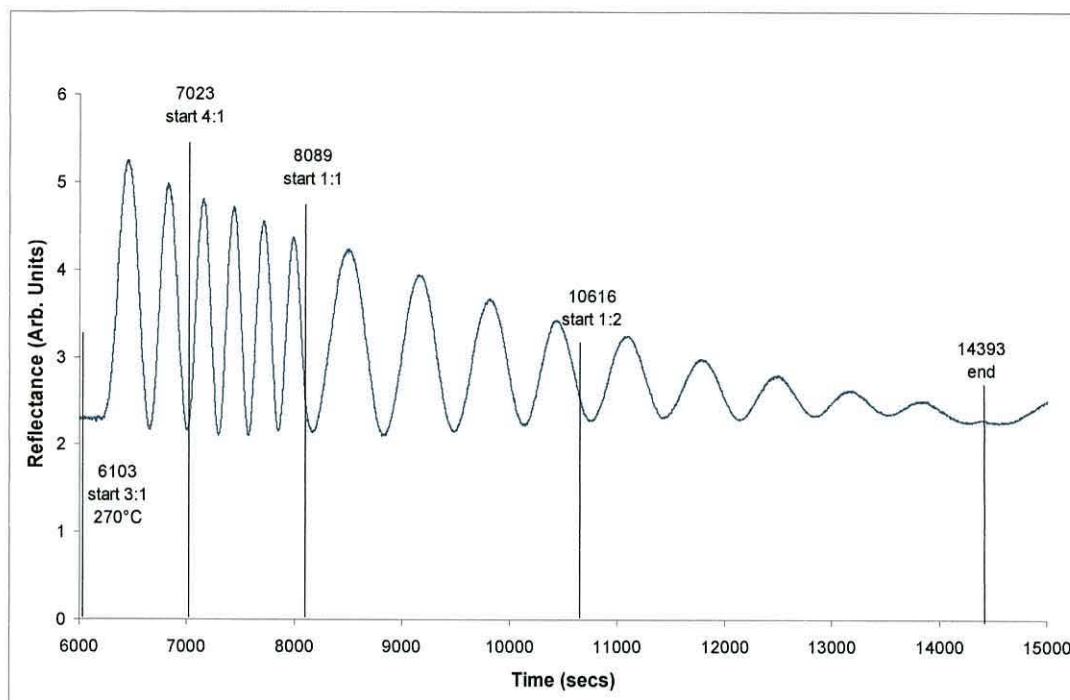


Fig. 4.3.6. Reflectance (Arbitrary Units) versus time (seconds) of banzn062. Substrate temperature maintained at 270°C whilst DEZn and n-Butanol precursor ratios altered.

4.4. Using Atomic Force Microscopy for thin film analysis

Atomic force microscopy is a commonly used tool for analyzing the surface morphology of thin films. In AFM a tip, typically constructed from silicon nitride, with a diameter of between 1 and 20 nm is mounted on a cantilever. The tip is kept at a constant distance, whilst scanned over the sample, via attractive Van Der Waals forces, and the repulsion forces of electron cloud overlap.

The balance between the two forces is maintained by a piezo-electric device. In this way an image of the surface is built-up. Using computer software the image can be displayed as a 2D or 3D topographical representation of the sample surface. Further manipulation of the data can yield information such as average roughness for the surface and average grain size. The apparatus used for the images presented in this thesis was a Nanoscope 3A with a J-type scanner.

The substrate requires no preparation for AFM. The maximum xy area that can be scanned is $150\text{ }\mu\text{m}$; however there is a limit to the z-range that means that samples with large surface unevenness may not be scanned.

The samples undergoing AFM in this research were representative of the substrate area measured by the interferometry as shown in figure 4.4.1. The non-uniformity of the thin film growth manifests itself in a wedge shaped deposition from inlet end to exhaust end. Taking samples from the cross-section in line with the interferometry measuring point allows the best knowledge of that samples thickness.

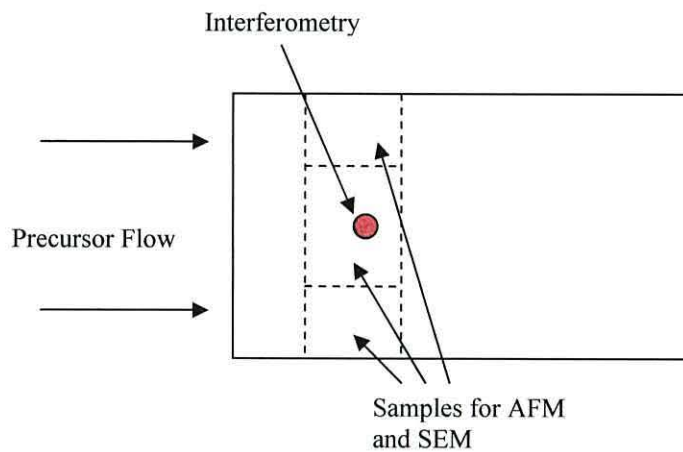


Fig. 4.4.1. Schematic of typical substrate. Red dot represents the area of measurement by the interferometer. The dotted lines represent the samples taken of the thin film for analysis.

In figure 4.4.2. the left hand image is a $5\text{ }\mu\text{m}^2$ 3D representation of the surface morphology. The centre image is the height histogram estimating the grain size for the $5\text{ }\mu\text{m}^2$ area. The right hand image is the roughness analysis of the $5\text{ }\mu\text{m}^2$ area giving a rms value of 6.35 nm.

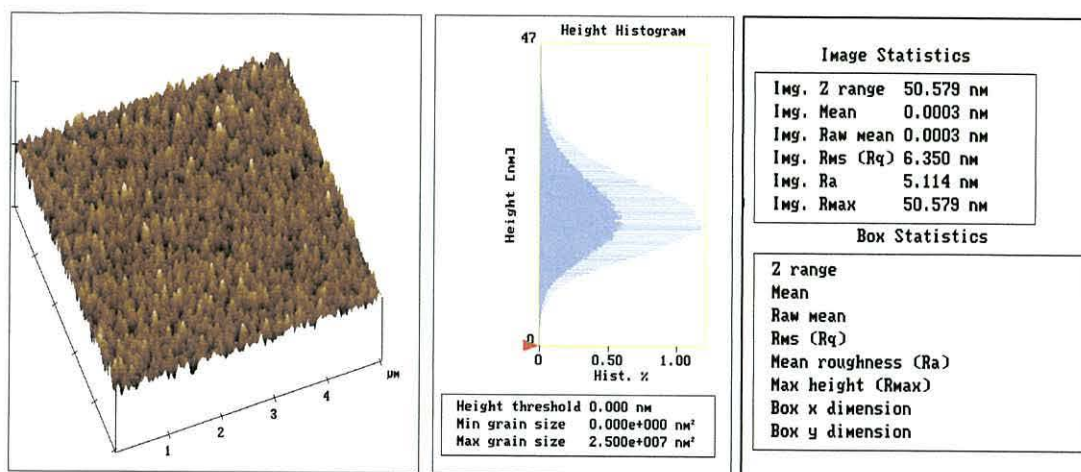


Fig.4.4.2. AFM 3D image, grain size and roughness data for a ZnO thin film deposited at 3:1 II/VI ratio and 300°C.

Measuring the grain size by hand is a recognized technique and compliments the AFM software. This method involves drawing a line of consistent length across the AFM images and measuring, using the scale on the image, the diameter of each grain that the line intercepts. An average of all grains dissected by the line is then taken.

4.5 Using Scanning Electron Microscopy for thin film analysis

The SEM is another powerful surface imaging tool used for thin film analysis. A beam of electrons is generated in an electron gun (the cathode); the beam is then attracted to the anode where a hole in the anode allows a fraction of the electrons to continue through. This fine beam of electrons is focused by electromagnetic lenses onto the sample surface. The beam is scanned across the area to be imaged creating amongst others secondary and backscattered electrons from the sample. These electrons are collected by a secondary or backscattered electron detector and converted to a voltage to be displayed.

SEM requires an electrically conducting sample so that charge from the electron beam can be dissipated; where a sample is non-conductive a thin coating of gold may be applied. During imaging the SEM is maintained under high vacuum. The

SEM has the added benefit over AFM of being able to image samples of very uneven surface morphology.

ZnO thin films are intrinsically conducting, however (see figure 4.5.1. (b)) to image the cross section of a thin film where the non-conducting glass substrate is exposed, it is necessary to coat the sample with a thin film of gold. As well as giving an image of the surface morphology of a thin film the SEM image may be used to give information on grain size in the same way describe for AFM.

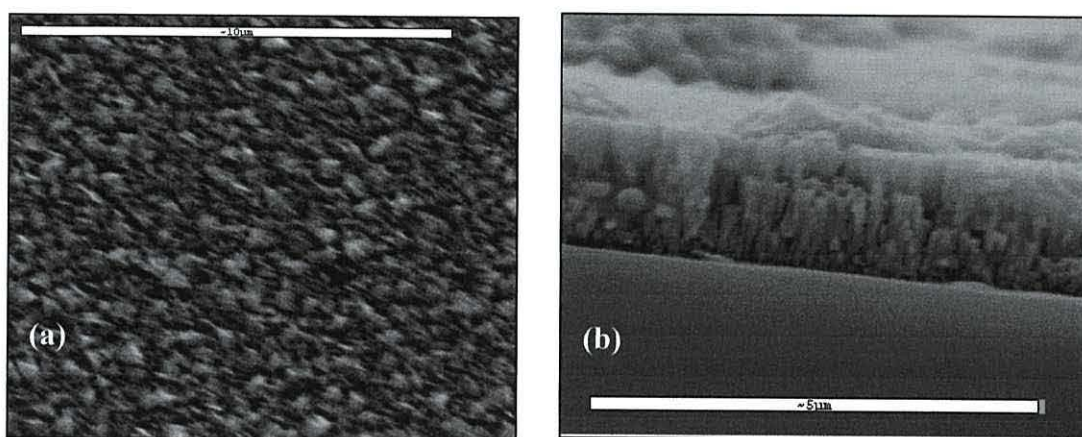


Fig. 4.5.1. (a) SEM image of the surface of a ZnO thin film, the scale bar indicates 10 μm . (b) SEM image of gold coated cross section of ZnO thin film, the scale bar is 5 μm . This image can be used as an indication of film thickness.

When the electron beam is focused onto the sample, backscattered X-rays are also generated as well as the secondary or backscattered electrons. These X-rays are resultant of the beam of electrons interacting with individual atoms of the sample. These X-rays may be detected and yield characteristic emission peaks enabling the identification of most elements. In this way qualitative and quantitative information of the elements in the sample may be gained. This technique is known as energy dispersive analysis of X-rays (EDAX) an example of an EDAX spectrum is shown in figure 4.5.2.

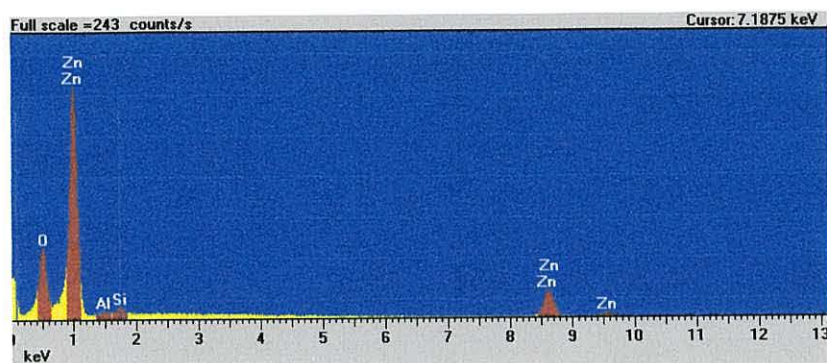


Fig. 4.5.2. EDAX spectrum of banzn053 a ZnO thin film deposited onto aluminosilicate glass substrate. Sample was deposited at 220°C and II/VI ratio 3:1. The film thickness was 1.5 μm .

In figure 4.5.2. each peak has been ascribed an identity, from an archive of elements contained in the software program, due to the particular energy at which it arises. For this sample of thin film ZnO the expected Zn and O peaks are clearly visible. There are also peaks arising from aluminum and silicon contained within the glass substrate. The EDAX of ZnO thin films in this work is purely qualitative as the necessary calibration of the equipment, for quantitative data, was not possible.

4.6 X-ray Diffraction

Thin films can be thought of in three crystallographic terms; amorphous, polycrystalline and single crystal. Amorphous describes a material without any regular ordered structure, polycrystalline a material with many interlocking but different crystals and single crystal being one with a completely regular structure throughout. It is important to gain knowledge of a thin films crystallographic structure as this dictates many of the films physical properties such as; electrical and thermal conductivity, refractive index and absorption coefficient.

The technique of X-ray diffraction is used to ascertain the crystallographic nature of a thin film and the effects any changes to deposition parameters have on it. X-rays are produced by striking a metal target with a beam of electrons and are then focused onto the sample to be investigated. The specific wavelength of the X-ray is determined by the metal target and the type of filter used. For this research a Phillips W3830 X-ray generator was used with a copper target the various X-rays

generated being filtered by a sheet of nickel to produce a monochromatic beam of Cu K_{α} radiation of wavelength 1.54Å.

This monochromatic beam of radiation of wavelengths, comparative to inter-atomic spacing, is incident on the sample producing reflections from any regular array of atoms or ions. Analysis of these reflections yields information of any and what type of crystallographic order there is within the sample. The thin films deposited for this research were found to be polycrystalline and the XRD technique has been used for defining the crystallinity, orientation and grain size of the thin films.

Crystallinity of the thin film is evident from the diffraction pattern; no clear diffraction peaks is synonymous with an amorphous film, a number of diffraction peaks with a polycrystalline film and a single sharp peak with a single crystal film. In the case of a polycrystalline thin film one particular orientation may be dominant, so-called preferred orientation. In this case the thin films may display anisotropic behavior if their physical properties depend upon the preferred orientation.

The orientation is found by comparison of the ZnO thin film data with standard ASTMS data for a ZnO powder sample, table 4.6.1. This allows the classification of any peaks arising from the ZnO thin film diffraction pattern.

2 θ	counts	ints(%)	θ	sin θ	d	h	k	l
31.797	20535	100%	15.8985	0.2739	2.811245	1	0	0
34.4	16874	47%	17.2	0.2957	2.603991	0	0	2
36.245	36024	100%	18.1225	0.311	2.475884	1	0	1
47.528	9448	26%	23.764	0.403	1.91067	1	0	2
56.641	10983	30%	28.3205	0.4744	1.623103	1	1	0
62.824	11130	31%	31.412	0.5212	1.47736	1	0	3
66.296	3283	9%	33.148	0.5468	1.408193	2	0	0
67.923	9960	28%	33.9615	0.5586	1.378446	1	1	2
69.117	5344	15%	34.5585	0.5672	1.357546	2	0	1
72.588	2642	7%	36.294	0.5919	1.300895	0	0	4
76.928	3236	9%	38.464	0.622	1.237942	2	0	2
81.376	2735	8%	40.688	0.6519	1.181163	1	0	4
89.621	4516	13%	44.8105	0.7048	1.092509	2	0	3
92.767	2852	8%	46.3835	0.724	1.063536	2	1	0

Table 4.6.1. standard ASTMS data for ZnO powder sample.

For this comparison the d -spacing (separation between the planes) is required for each diffraction peak. This is given for hexagonal ZnO by equation (4.6.1.).

$$\log d^2 = \log [a^2 / 4/3 * (h^2 + hk + k^2) + (l^2/(c/a))] \quad (4.6.1.)$$

Where d is the separation between the planes, h , k and l are integers known as Miller indices and used to describe any particular plane of the unit cell. The thin films of ZnO crystallized in the Wurtzite form shown in figure 4.6.2. $c = 5.12 \text{ \AA}$ and $a = 3.25 \text{ \AA}$. The Wurtzite structure is composed of a hexagonal close packed array of oxygen ions with alternate tetrahedral holes occupied by zinc ions. Each oxygen ion is tetrahedrally coordinated by four zinc ions and vice versa. Thus using equation 4.6.1. diffraction peaks arising from a thin film sample may be allocated a particular orientation as shown in figure 4.6.1.

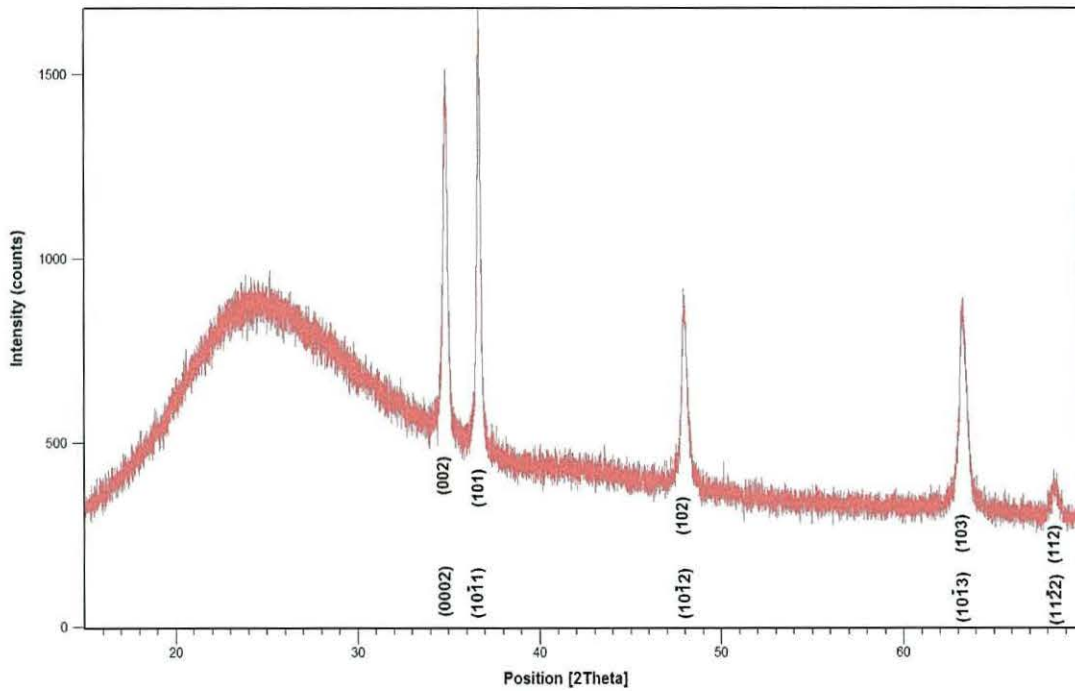


Fig. 4.6.1. XRD pattern showing main orientations for ZnO thin film deposited at 219°C and various II/VI ratios. Film thickness = 2.5 μm .

The hexagonal crystal structure can be more accurately describe by using four coordinates as shown in figure 4.6.3. The fourth coordinate is designated i and is related to h and k by equation 4.6.2. The equivalent four Miller indices notation is shown below the three Miller indices labels in figure 4.6.1.

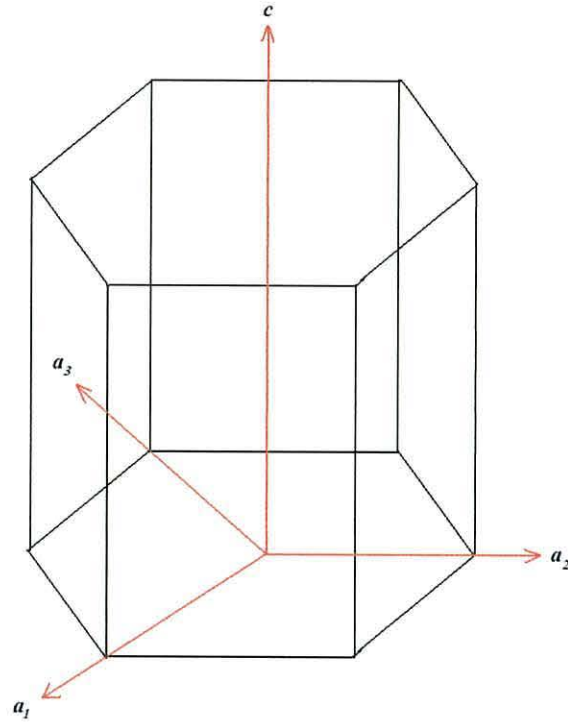


Fig. 4.6.2. i is related to a_3 the fourth coordinate required to describe planes in the hexagonal close packed array.

$$i = -(h+k) \quad (4.6.2.)$$

Figure 4.6.3. represents the (0002) plane in the hexagonal system. When this reflection arises, in thin film XRD, the c -axis is described as normal to the substrate surface.

In a polycrystalline thin film each crystal is referred to as a grain. For TCOs the size of these grains is an important factor in the electrical conductivity of the films. The region where one grain comes into contact with another is known as the grain boundary. It is at these grain boundaries where recombination of charge carriers may

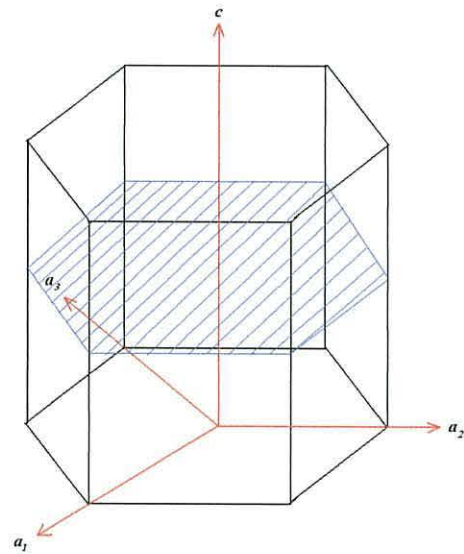


Figure 4.6.3. the (0002) plane within the hexagonal system.

occur. Thus, the smaller the average grain size of a thin film the larger the area of grain boundaries. This leads to an increased probability of recombination and hence increases in resistivity. To improve the conductivity of a TCO it is desirable to maximize grain size.

It is possible to calculate the grain size by XRD, of any particular orientated crystal giving rise to a diffraction peak, using the Scherrer equation (4.6.3.).

$$GS = (0.94 * \lambda) / (FWHM * \cos \theta) \quad (4.6.3.)$$

Where GS = grain size, 0.94 = shape factor, λ = X-ray wavelength 1.54 Å, FWHM = full width at half maximum and, θ = peak position. When the grain size of all orientations is calculated an average grain size for the bulk material can be obtained.

4.7 Electrical measurements of thin films

For the ZnO thin films deposited in this research the resistance was measured by; evaporating two gold contacts of a known size and distance apart, applying a voltage to these contacts and measuring the current generated between them. The set up of the resistance measurement is shown in figure 4.7.1. With knowledge of the voltage and current the resistance of the thin films were found using Ohm's law, equation 4.7.1.

On applying this technique two assumptions were made; all contacts made to the films were equal and the film thickness as measured by interferometry did not change over the measured area. The quoted electrical measurements have their associated errors arising from each parameter involved. The resistance measurements error arises from any differences in the contacts made to the films and their subsequent connection to the IV instrument. The IV instrument will also have an associated error.

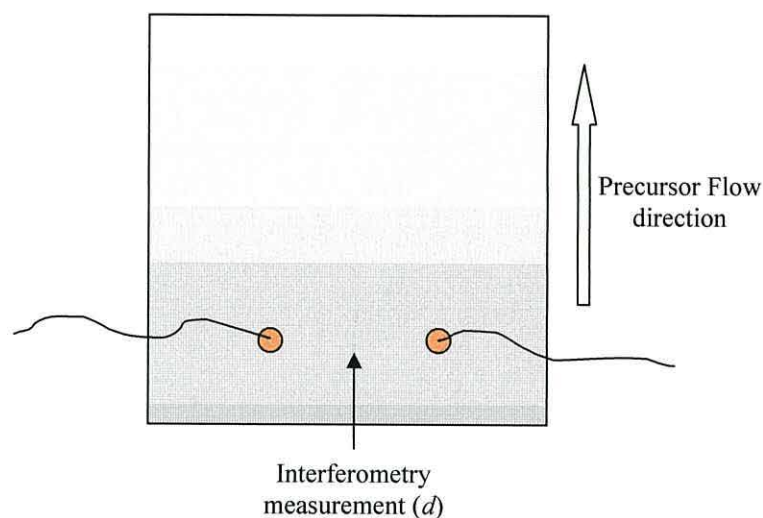


Fig. 4.7.1. Schematic of the gold contacts made to the thin films for the measurement of resistance. The shading represents the non-uniformity in the thin film thickness.

The error in the sheet resistance data is resultant from the resistance data error and from error in measuring the contact dimensions. The resistivity data contains the error of the sheet resistance calculation along with error arising from the film thickness measurement by interferometry. These are shown in table 4.7.1.

Measurement	$R (\Omega)$	$\rho \Omega \text{ cm}$	$R_s \Omega/\square$
Error	$\pm 1\%$	$\pm 6\%$	$\pm 12\%$

Table 4.7.1. Errors associated with electrical measurements.

Ohms law: $V = I \cdot R$ eq (4.7.1.)

Therefore: $R = V/I$ eq (4.7.2.)

For TCOs the parameter called the sheet resistance (R_{sheet}) is often quoted in the literature. R_{sheet} is calculated from knowledge of the materials resistance and the contact dimensions; it does not take account of the films thickness. With a value for the resistance the R_{sheet} can be calculated from equation 4.7.3:

$$R_{\text{sheet}} = (R \cdot W) / L \quad \text{eq (4.7.3.)}$$

Where L = the distance between the two contacts and W = the width of the contacts. For the thin films measured in this research the distance between the two contacts was 5 mm and the width of the contacts was 1.1 mm. From equation 4.7.3. the unit of R_{sheet} is seen to be the ohm.

The resistivity (ρ) of a thin film is an intrinsic property of the material; it is a measure of the ability of material to resist the flow of an electric current. Resistivity of a thin film is calculated from knowledge of the resistance, the contact dimensions and the film thickness, see equations 4.7.4. and 4.7.5.

$$\rho = R \cdot W \cdot d / L \quad \text{eq (4.7.4.)}$$

Substituting R_{sheet} for $(R \cdot W) / L$:

$$\rho = R_{\text{sheet}} \cdot d \quad \text{eq (4.7.5.)}$$

From equation 4.7.5. the units of ρ can be seen to be Ω m, which are often more conveniently expressed as Ω cm.

The errors of this technique may be quantified by applying the same approach to a sample of commercial ITO with a known resistance. The ITO sample was obtained from Delta Technologies Ltd (CG-511N-S107) where it was produced by sputtering onto SiO_2 passivated, polished float glass. This value for the ITO sample is then the benchmark to which all the ZnO thin films deposited in this research are compared.

4.8 References

- [1] M. Purica, E. Budianu, E. Rusu, M. Danila and R. Gavrilă, Thin Solid Films **403-404** (2002) 485-488.

Chapter Five: Results and Discussion

5.1 Introduction

After the design and construction of the MOCVD system a number of experiments were carried out to test the capabilities of the system for thin film growth. Following these experiments a number of films were deposited. The results and discussion of these thin films are presented in this chapter.

The non-uniformity of deposition is presented and clarified. Temperature dependant growth regimes are described. Reaction mechanisms that describe the changes in growth rate at different precursor ratios are proposed. Nucleation delays are measured and the results discussed in terms of the effective supersaturation of reactive species at the substrate surface. The optical and electrical properties of the films are presented and discussed along with the thin film morphology as given by AFM, SEM and XRD.

5.2 Thin Film Profile

All the ZnO thin films deposited within this research had a distinctive wedge shaped profile. This was due to the non-rotation of the substrate leading to a concentration gradient of precursors over the substrate. The part of the substrate nearest the precursor inlet was exposed to the maximum precursor concentration and the part of the substrate furthest from the inlet exposed to a depleted precursor concentration. The effect of this wedge shaped profile needs to be considered when characterising the thin film properties.

Figure 5.2.1 shows a typical ZnO film where analyzing it by cross-sectional SEM, at four different points along the length of the substrate, it was possible to characterise the wedge shape profile. An estimation of the film thickness at the four sample points along the substrate is shown in figure 5.2.2; this figure also includes the films thickness as measured by *in situ* interferometry which can be seen to fit well with the SEM estimated thickness. Error in measuring film thickness from

cross sectional SEM arises from the angle of incidence of the electron beam on the sample. The images shown in figure 5.2.1 are not normal to the incidence beam, hence the perspective has been considered along with error in the final measurement when allocating the error bars. The film thickness as given by the *in situ* interferometry has errors arising from the parameters given in equation 4.2.1 (page 88).

When analysing the films the evidence of a wedge shaped profile has been used to the affect that all *ex situ* measurements were carried out on the area of the substrate measured by the interferometer. This enabled the most accurate knowledge of the films thickness to be used.

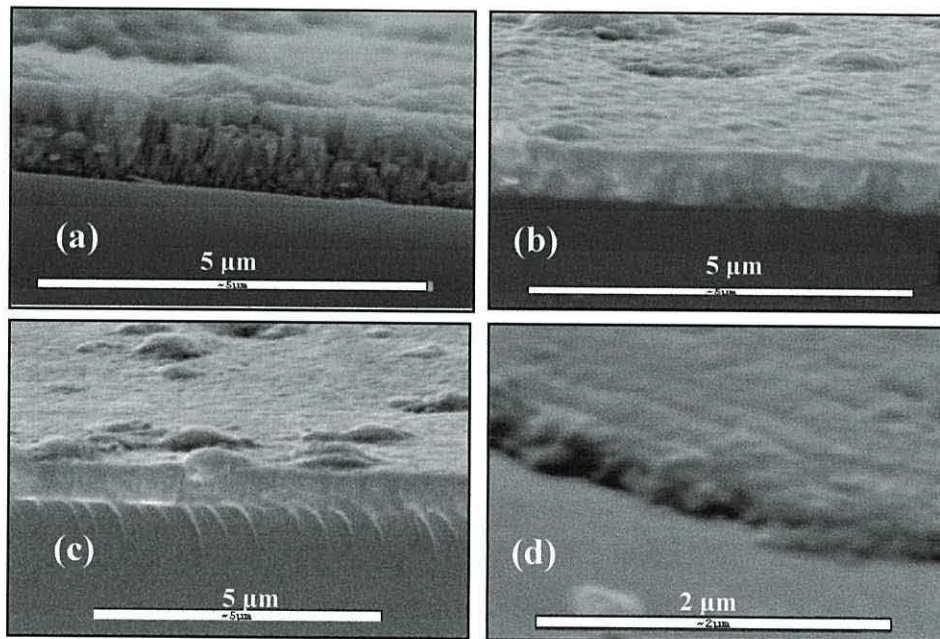


Fig. 5.2.1 Cross-sectional SEM images of 055 deposited at 219°C and II/VI = 4. (a) Sample taken 3 mm from leading edge, estimated thickness = 1.3 μm . (b) Sample taken 10 mm from leading edge, estimated thickness = 0.9 μm . (c) Sample taken 17 mm from leading edge, estimated thickness = 0.6 μm . (d) Sample taken 23 mm from leading edge, estimated thickness = 0.3 μm .

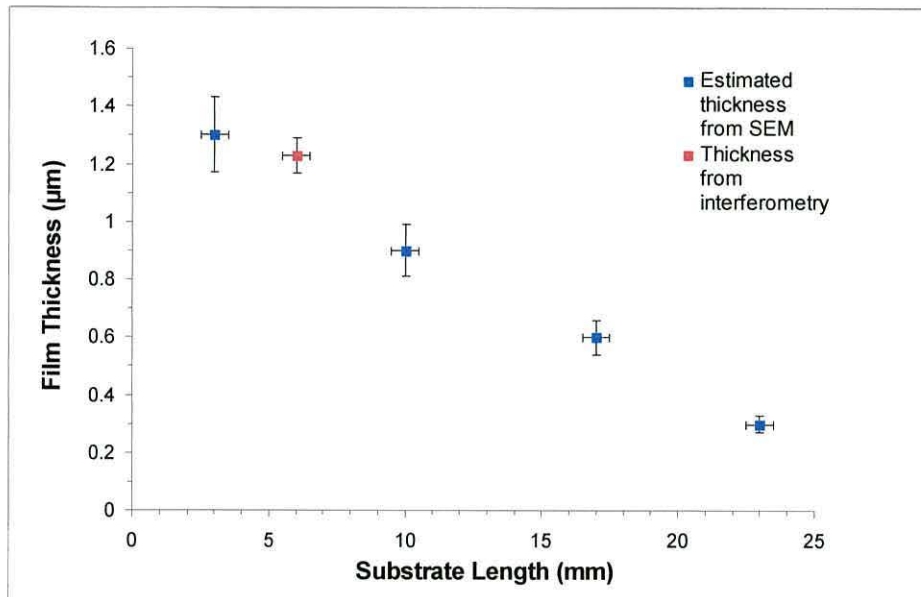


Fig. 5.2.2 Plot of film thickness (μm) versus distance from substrate leading edge (mm). The blue data is an estimated thickness from cross-sectional SEM. The red data point is the thickness as measured by interferometry.

Since the introduction of the MOCVD technique one of the main considerations has been the ability to achieve good film thickness uniformity. The two major influences on thickness uniformity within a MOCVD reactor are, uniform heating and uniformity of the delivery of the precursors to the whole of the substrate area. The former is relatively easy to control in a single-wafer reactor, by uniformly heating a susceptor onto which the substrate is mounted. However, the uniform introduction of the precursors to the whole substrate area is more difficult to achieve.

The majority of MOCVD systems typically mix the individual precursors together in a manifold, before entering the reactor. This mixture of precursors is then transported to the heated substrate area to form a thin film. However, for oxide thin film deposition, prereactions are observed which produce a powder deposit fouling the inlet lines. Thus, mixing of the precursors close to the substrate is usually favoured for oxide systems.

With the non-rotated substrates, problems arise in thickness uniformity as the area of the substrate closest to the reactor inlet will receive the highest concentration of precursor. The area of the substrate furthest from the reactor inlet receives, due to depletion effects, a lower concentration of the precursors. This is the foremost factor leading to non-uniformity in MOCVD thin films.

The four cross sectional SEM images shown in figure 5.2.1 are typical of the ZnO thin films deposited in this research. Image (a) was taken 3mm from the leading edge; an estimate of film thickness was made using the scale bar. Image (a) also clearly shows a columnar nature of the ZnO film under those deposition parameters. Images (b) and (c) were taken further from the leading edge and show the ZnO film thickness decreasing. Image (d) is at 30 degrees to the substrate surface and shows that at the end of the substrate, under these deposition conditions, the film becomes very thin.

These results provide direct evidence of gas-phase depletion of the active precursor over the length of the substrate. The leading edge displays the fastest growth rate as it receives the maximum concentration of active precursor. The active precursor is consumed by the growing film, this leads to decreasing concentrations being available for film growth further along the substrate. The figure 5.2.2 identifies a wedge shaped deposition profile. The film thickness as measured by *in situ* interferometry is also shown in figure 5.2.2 and fits well with the SEM estimated measurements. As described in 4.4.1 (page 92), analysis of the ZnO thin films was carried out on the same area of each substrate in order to negate any influence of the wedge shape profile.

Leys [1] reported that good homogeneity in film thickness requires rotation of the substrate. Rotation allows the whole area of the substrate to effectively receive an equal concentration of the precursors. Rotation of the substrate is achieved either by using a motor or gas flow to revolve the susceptor. The former is more difficult to engineer as the drive shaft must enter the reaction vessel creating a metal/quartz

interface that needs to withstand a vacuum. The benefits of this method of rotation are absolute knowledge and control of the revolutions per minute (rpm) of the susceptor. This enables thickness uniformity to be correlated to substrate rotation. The latter technique for substrate rotation involves a susceptor that contains a rotating segment onto which the substrate is mounted.

5.3 Growth Properties and Kinetics

5.3.1 Pyrolytic Deposition

Figure 5.3.1 shows the growth rates of the ZnO plotted as a function of the substrate temperature for $\text{II/VI} = 3$. In the low temperature regime between 50 and 150°C the growth rate steadily increases, this is normally attributed to [2] the decomposition of the thermally activated precursors and site blocking by unreacted organometallics or adsorbed products. Between 200 and 250°C the growth rate reaches a maximum, in this range the growth rate may be limited by desorption of unreacted precursors from the substrate surface. Above 250°C the growth rate decreases rapidly due to: (a) thermal cracking of the precursors before reaching the reaction zone leading to deposition on the reactor walls and (b) desorption of unreacted precursors.

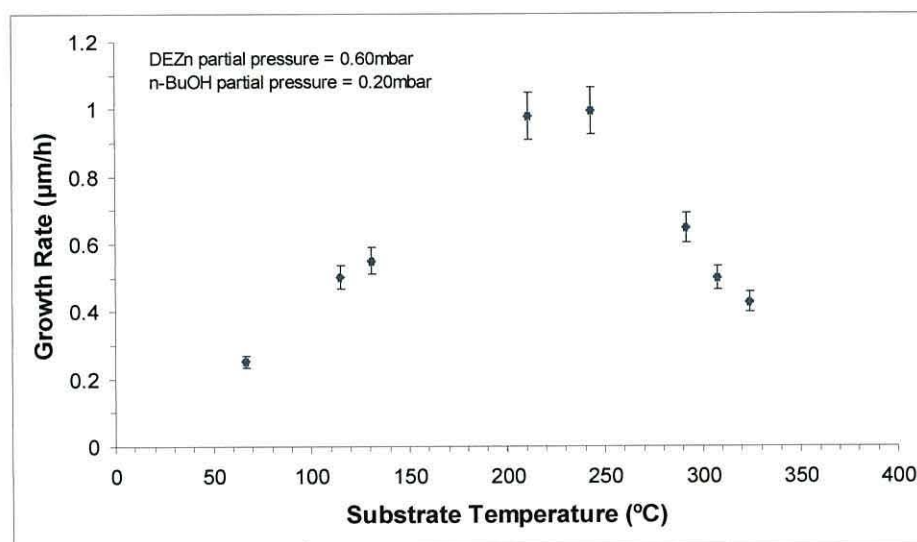


Fig. 5.3.1 The growth rates ($\mu\text{m/h}$) as a function of substrate temperature ($^{\circ}\text{C}$) for ZnO thin films grown at $\text{II/VI} = 3$.

Figure 5.3.2 shows the growth rates of the ZnO plotted as a function of the substrate temperature for II/VI = 1. In comparison to figure 5.3.1 the growth rates can be seen to be approximately 5 times lower but following the same general trend. It was not possible to achieve any data points for substrate temperatures below 180°C due to the extremely low growth rate. The effect on growth rate, of changing the precursor ratios can help to identify the reaction mechanisms of the thin film growth. Experiments were carried out on varying the precursor ratios in the three temperature regimes outlined above.

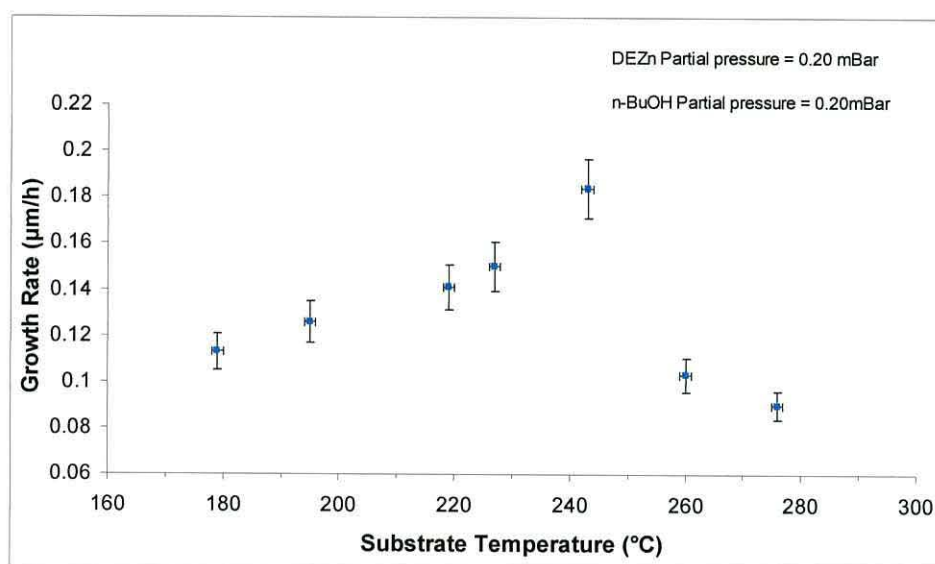


Fig. 5.3.2 The growth rates ($\mu\text{m/h}$) as a function of substrate temperature ($^{\circ}\text{C}$) for ZnO thin films grown at II/VI = 1.

Growth rate results for the photoassisted films are not presented here. Insufficient data were collected to produce a growth rate versus substrate temperature or UV power.

No prereaction was observed over the deposition temperatures shown in figures 5.3.1 and 5.3.2. For both the II/VI ratios the growth rate steadily increases with increasing temperature reaching a maximum at around 240°C. This increase in growth rate is attributed to the decomposition of the precursors being thermally activated. Above 240°C the growth rate decreases rapidly possibly as a result of

premature thermal cracking of precursors before reaching the reaction zone or desorption of unreacted precursors.

The growth rate versus substrate temperature results shown in figures 5.3.1 and 5.3.2 agree with similar studies from the literature by Oda *et al.* [3] and Kirchner *et al.* [4] which follow the same general trend, described above. In the case of Hahn *et al.* [5] the growth rate maximum is an extended region between 320 and 410°C. This is typical of mass transport limited growth where, the growth rate is limited not by temperature but the supply of precursors to the deposition zone. This behavior was not seen in figures 5.3.1 and 5.3.2 suggesting that mass transport was not dominant in this system.

It was the deposition conditions of Hahn *et al.* [5] that the work presented in this thesis most closely resembled. However, the VI/II ratios do differ significantly, this along with the isomeric factor of n-BuOH compared with t-BuOH may explain the higher growth rates (1.2 $\mu\text{m/h}$ for VI/II = 3.5 in Hahn *et al.* [5] versus 0.18 $\mu\text{m/h}$ for VI/II = 1) and the mass transport controlled region.

The work by Oda *et al.* [3] and Kirchner *et al.* [4] which was carried out at a reduced reactor pressure which, as described in chapter 2.3, avoids premature reactions by increasing the mean-free path of the precursors. Three different alcohols were used by Oda *et al.* [3]; it is interesting to note that the thin film maximum growth rate decreased from tertiary to secondary to primary alcohol and also with increasing alkyl chain length (3.5, 2.2 and 1.6 $\mu\text{m/h}$ respectively). Following this trend n-BuOH with its longer alkyl chain would be expected to, and indeed did at 0.18 $\mu\text{m/h}$, produce a much lower maximum growth rate than the EtOH used by Oda *et al.* [3]. The longer the aliphatic chain the more stable the alcohol is and therefore less likely to react with the DEZn. This is highlighted in table 5.3.1 where the growth rates of ZnO from various alcohols are reported.

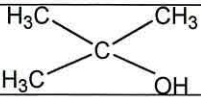


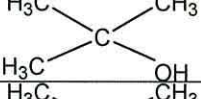
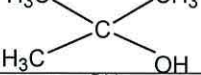
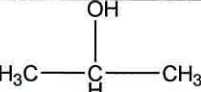
Author	Alcohol precursor	VI/II Ratio	Reactor pressure (atm.)	Max. growth rate temp (°C)	Max. growth rate (μm/h)	Alcohol Structure
Oda <i>et al.</i> [3]	t-BuOH	18-166	0.08-0.4	300	3.5	
	MeOH			300	2.2	
	EtOH			300	1.6	
Hahn <i>et al.</i> [5]	t-BuOH	3.5	1	320-410	1.2	
Kirchner <i>et al.</i> [4]	t-BuOH	18	0.2-0.5	400	2.1	
	i-PrOH			350	1.9	

Table 5.3.1 Growth rate versus deposition temperature results for three studies of ZnO thin films using DEZn with alcohol precursors.

Figure 5.3.3 shows that, in all three temperature regimes, an increase in DEZn concentration whilst maintaining a constant n-BuOH concentration leads to a linear increase in growth rate. In this case the growth rate is limited by the partial pressure of the zinc precursor.

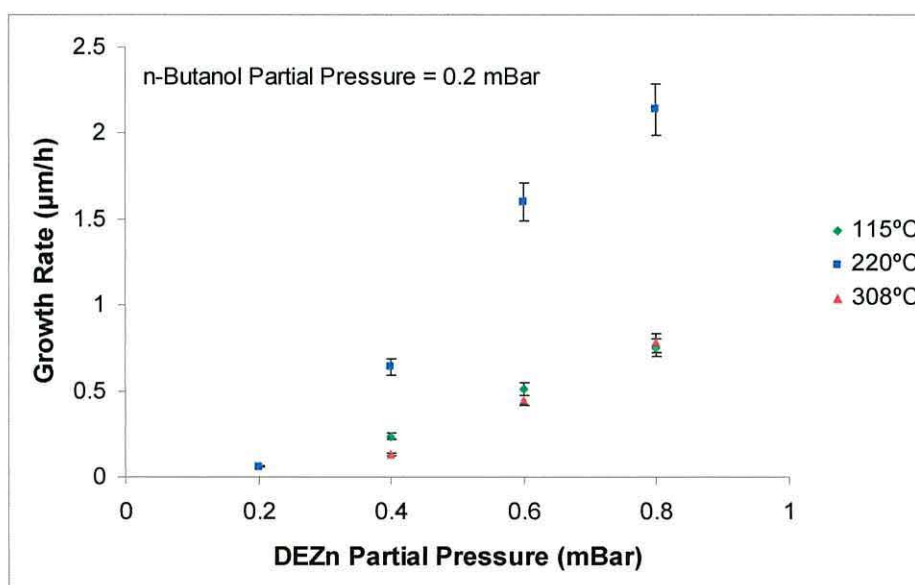


Fig.5.3.3 Growth rate (μm/h) versus increasing DEZn partial pressure (mBar), maintaining a constant n-BuOH partial pressure and at various temperatures.

To understand the effect on growth rate of precursor ratios, previous work on the reactions of alkylzinc with alcohols and ZnO thin film deposition must be considered. From work by Coates *et al.* [6] it is known that when DMZn and R-OH are mixed the result is the formation of an alkylzinc alkoxide with little displacement of the second alkyl group. Furthermore, as discussed in chapter 2.8, this alkylzinc alkoxide was also shown to exist as a tetrameric oligomer. Auld *et al.* [7] proved that the alkylzinc alkoxide ($\text{MeZn}(\text{OBu}^t)$) proved sufficiently volatile to be used as a single source precursor for the growth of ZnO by MOCVD.

Auld *et al.* [7] stated that the $\text{MeZn}(\text{OBu}^t)$ 'is decomposed into ZnO either in the hot boundary layer above the substrate, or more likely, during heterogeneous pyrolysis of the alkylzinc alkoxide on the substrate surface'. The decomposition of this alkylzinc alkoxide 'active precursor' was shown, by Ashby *et al.* [8], to follow a cyclic six-centered transition state shown in figure 2.9.3 (page 48). The ZnO thin film is formed on the surface when a β -hydrogen of the alkoxy moiety is abstracted by the methyl group of the zinc.

In this research, the $\text{EtZn}(\text{OBu}^n)$ active intermediate is unlikely to decompose by a cyclic six-centered transition state. This is due to the straight chain butyl being sterically less likely to follow the same route as the branched butyl of the $\text{MeZn}(\text{OBu}^t)$. If indeed the rearrangement follows a cyclic mechanism then the cyclic five-centered transition state proposed in figure 5.3.4 would be more likely. Abstraction of a β -hydrogen from the alkoxy moiety by the ethyl group could result in the formation of ethane, a carbene and zinc oxide adsorbed to the surface.

It is proposed that this cyclic rearrangement of the $\text{EtZn}(\text{OBu}^n)$ would be less favorable than that of the $\text{MeZn}(\text{OBu}^t)$ for two reasons. Firstly the β -hydrogen of the alkyl group of the $\text{EtZn}(\text{OBu}^n)$ is sterically less likely to interact with the ethyl group than that of the branched alkyl groups with the methyl in the $\text{MeZn}(\text{OBu}^t)$. Secondly, the carbene formed is an unstable high energy product.

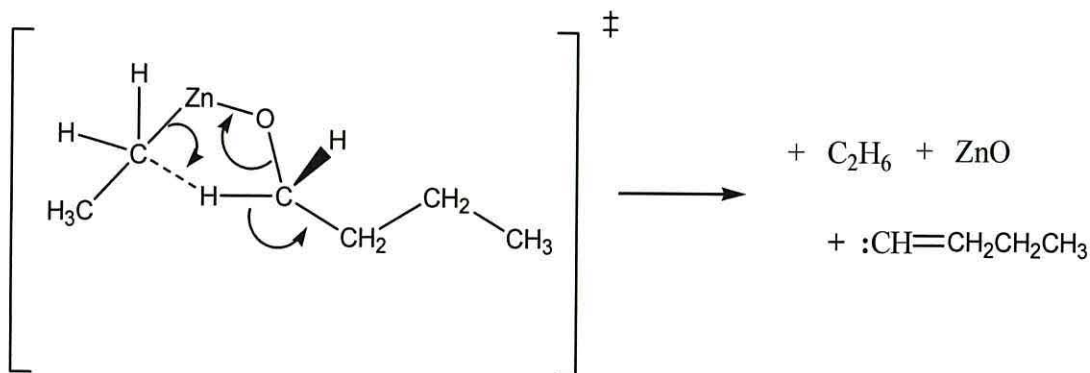


Fig. 5.3.4 Cyclic five-centered transition state and products of EtZn(OBuⁿ) alkylzinc alkoxide.

It is more likely that the rearrangement of the EtZn(OBuⁿ) species, adsorbed onto the surface at these growth temperatures, takes place via a radical reaction. It is tentatively proposed that the mechanism is not a cyclic rearrangement but one that, for equimolar DEZn and n-BuOH, follows the route shown in figure 5.3.5. This mechanism would then be responsible for k_A in the rate equation 5.3.1.

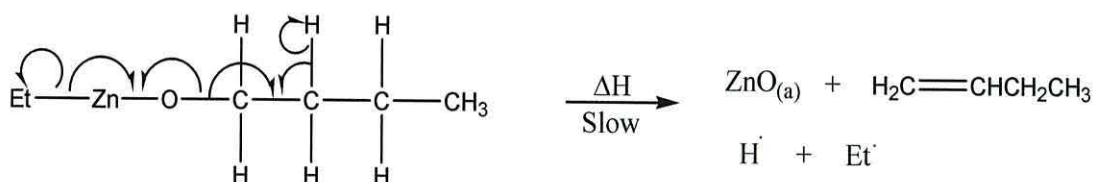


Fig. 5.3.5 Proposed radical mechanism and products of decomposition of EtZn(OBuⁿ) alkylzinc alkoxide.

$$\text{Growth Rate} = k_A [\text{EtZn(OBu}^n)] + k_B ([\text{DEZn}] - [\text{n-BuOH}]) \quad (5.3.1)$$

Where $k_A \ll k_B$

The results in figure 5.3.3 demonstrate that at these temperatures the kinetics are pseudo-first order with respect to DEZn partial pressure. It should be noted however that the linear section of the plot (in excess of II/VI = 1) does not pass through the origin as expected for a first order rate equation. When DEZn partial pressure moves below 0.2 mBar (where II/VI = 1) the growth rate decreases more slowly. The rate equation 5.3.1 describes the growth rate data for ZnO from figure

5.3.3 where; $[\text{EtZn}(\text{OBu}^n)]$ is the concentration of alkylzinc alkoxide and $[\text{DEZn}] - [\text{n-BuOH}]$ represents an excess of DEZn (above the II/VI = 1 ratio).

This increase in growth rate with increasing excess DEZn partial pressure may be explained by the DEZn decomposing into a mono-ethylzinc radical which is physisorbed onto the surface. This mono-ethylzinc radical, may then act as an initiator, preferentially inserting into the carbon-oxygen bond of the alkoxide, and removing the butyl chain to form an asymmetric alkylzinc leaving group as shown in figure 5.3.6 This leaves chemisorbed Et-ZnO from which the Et \cdot radical will eventually desorb. Effectively the higher the II/VI ratio the larger the concentration of the mono-ethyl zinc radical, physisorbed to the surface, is available to decompose the alkylzinc alkoxide. This mechanism would then be responsible for k_B in the rate equation 5.3.1.

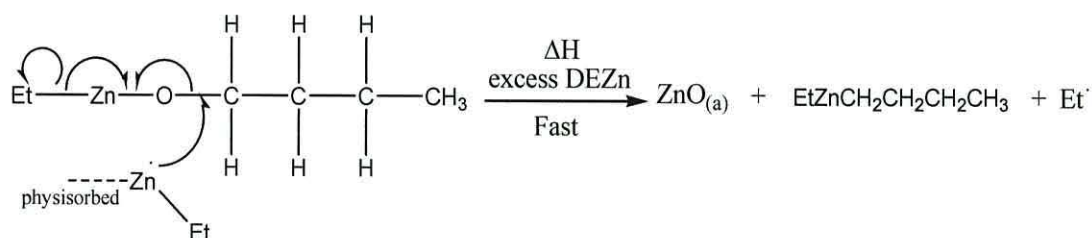


Fig. 5.3.6 Proposed mechanism and products of decomposition of $\text{EtZn}(\text{OBu}^n)$ alkylzinc alkoxide under conditions of excess DEZn.

Figure 5.3.7 shows the effects on growth rate when moving from zinc rich conditions to alcohol rich conditions. It should be noted that the equimolar portion of the graph occurs at an n-BuOH partial pressure of 0.6 mBar in this case. From figure 5.3.3 it was seen that the growth rate of ZnO was extremely low at DEZn/n-BuOH partial pressures of 0.2 mBar. Therefore for the investigation into high VI/II ratios the partial pressure of the DEZn was fixed at 0.6 mBar enabling reasonable growth rates for data collection.

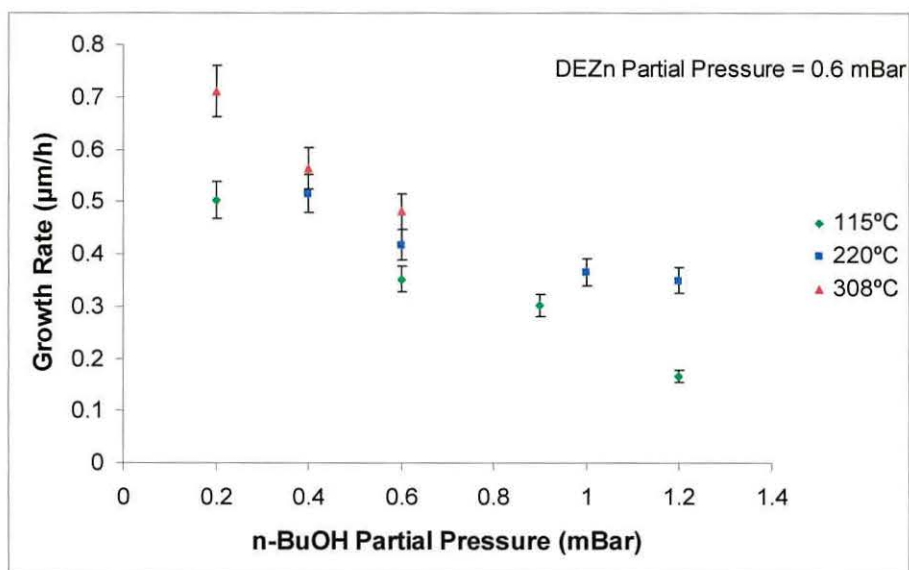


Fig. 5.3.7 Growth rate ($\mu\text{m/h}$) versus increasing n-BuOH partial pressure (mBar), maintaining a constant DEZn partial pressure and at various temperatures.

Taking the above into context the first section of the graph in figure 5.3.7, n-BuOH partial pressure 0.2-0.6 mBar, represents moving from zinc rich to equimolar conditions. This may be treated as a different experiment to figure 5.3.3 as it is the DEZn partial pressure that remains fixed throughout. However, the behavior of this section of the graph is similar to that seen in figure 5.3.3 where the growth rate increases with increasing II/VI ratio, thus supporting the proposed EtZn radical mechanism. The alcohol rich conditions occur where the n-BuOH partial pressure moves from 0.6 to 1.2 mBar. In this part of the graph, for the deposition temperature of 220°C, the growth rate decreases initially, appearing to level out at the highest VI/II ratio. In the lower growth rate regime 115°C the growth rate decreases more rapidly as the VI/II ratio increases.

The suppression of the growth rate, when moving to higher VI/II values, could be explained by surface site blocking by the excess n-BuOH in a Langmuir-Hinshelwood type mechanism. This argument may be supported by the evidence in figure 5.3.7 that, at the lower temperature (115°C), the reduction in growth rate is the greatest where the n-butanol will be more strongly adsorbed. Whereas, at the

higher temperature (220°C), where site blocking would be less effective due to increased thermal energy, the reduction in growth rate was reduced.

Evidence for this site blocking by the excess alcohol is given by Kim *et al.* [9] who reported that isopropanol chemisorbed into isopropoxy and atomic hydrogen on the surface of Si (100) between 550 and 650K. The Kim *et al.* [9] study into the thermal decomposition pathway and desorption of isopropanol and tertiary butanol on silicon (100), shown in figure 5.3.8, demonstrated that both alcohols were adsorbed onto the silicon below 150K in an ultrahigh vacuum chamber. Both alcohols were observed to desorb at temperatures below 550K. Decomposition of the isopropanol on the silicon surface did not take place until 650K where it decomposed into a isopropoxy radical and a hydrogen atom. The tertiary butanol decomposed at 640K to form iso-butene and a surface adsorbed hydroxy group.

Assuming for these surface reactions that n-butanol (sterically) and the aluminosilicate substrates, discussed in this thesis, are analogous to the isopropanol and silicon respectively. Under the temperature regimes of this research < 580K the n-butanol, in isolation, could then be thought of as a site blocking molecule adsorbing and desorbing on the surface unreacted.

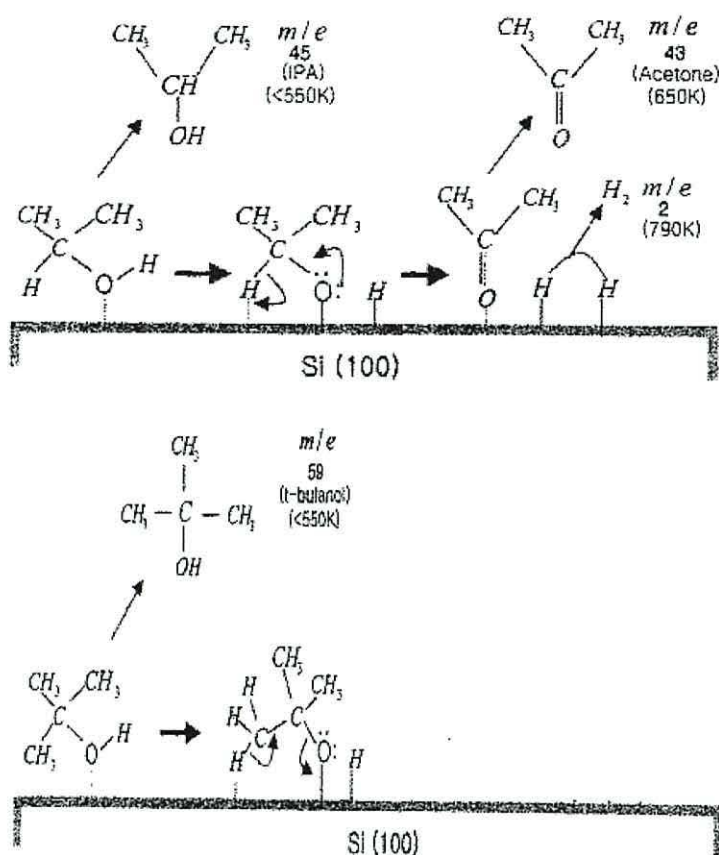


Fig. 5.3.8 Adsorption and desorption pathways of isopropanol and tert-butanol. After Kim *et al.* [9]

If the n-BuOH was preferentially adsorbed, over the alkylzinc alkoxide, onto the substrate it would block sites on the substrate surface. The rate of reaction would then be determined by how many sites were available for the alkylzinc alkoxide to adsorb onto the substrate and further decompose to ZnO. Therefore, the higher the partial pressure of n-BuOH at the substrate surface, the lower the likelihood of the alkylzinc alkoxide finding a free surface site and hence the lower the growth rate.

Both of the radical mechanisms proposed, shown in 5.3.5 and 5.3.6, result in different reaction products; the identification of the reaction products in the exhaust gas by mass spectrometry may offer conclusive evidence of the reaction mechanism. In figure 5.3.5 the hydrogen and ethyl radicals may combine to form products such as: molecular hydrogen, ethane and butane. An experiment to

replace a hydrogen atom, predicted to leave the alkoxide in figure 5.3.5, with deuterium may also help to clarify the reaction mechanism.

Mass spectrum analysis of exhaust gases has been shown to give some evidence as to the reaction products resulting from MOCVD of alkylzinc with alcohol. Oda *et al.* [3] deposited ZnO onto glass substrates using DEZn and R-OH (not n-BuOH). The surviving chemical species in the exhaust gas were monitored by a mass spectrometer.

Figure 5.3.9 shows a typical mass spectrum for a DEZn/t-BuOH deposited at various temperatures. The figure clearly shows a number of zinc related peaks at m/e of between 60 and 225. The peaks at 190 and 219 m/e are seen to disappear as the deposition temperature increases. This gives evidence of the products of reaction and hence the reaction pathway changing with temperature.

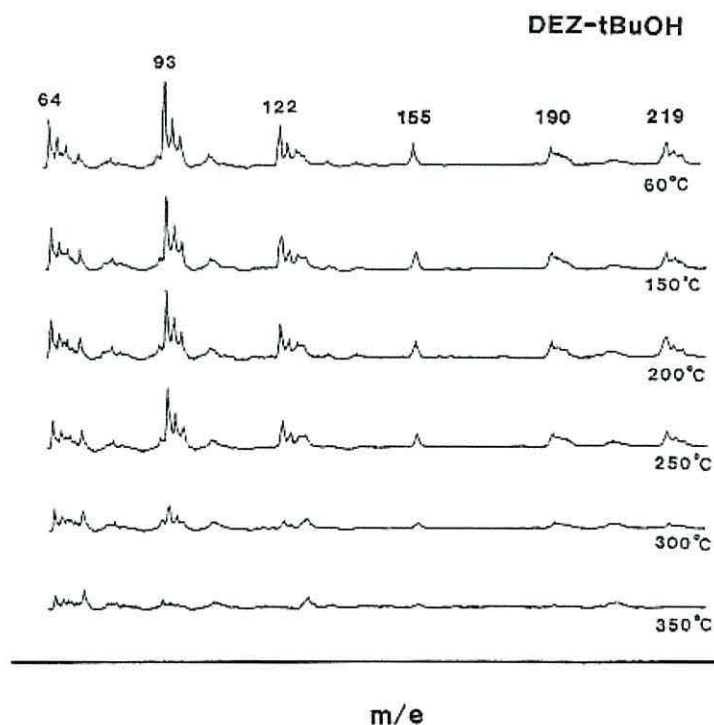


Fig. 5.3.9 Temperature dependant Mass Spectra of a DEZn/t-BuOH system for various deposition temperatures. After Oda *et al.* [3].

The reaction products in figures 5.3.5 and 5.3.6 are easily distinguished. The zinc alkyl product would be most easily distinguished by mass spectrometry. Zinc peaks having a characteristic shape due to the isotopic ratio; $^{64}\text{Zn}:^{66}\text{Zn}:^{68}\text{Zn} = 49:28:19$. Also the ethyl radicals would combine to form butane. It is suggested that both these mechanisms are occurring at the same time with the mono-ethylzinc initiated reaction dominating at higher than equimolar II/VI ratios. Therefore the mass spectrum analysis of the reaction products as a function of precursor concentration would elucidate these competing mechanisms.

As stated in chapter 2.6 there has been little research into the affects of an increasing II/VI value. In this research the transparencies of the thin films, at all deposition temperatures, did not alter significantly in response to high II/VI values or even up to II/VI = 3. Because of the lack of research within the literature and the increased growth rates, the majority of thin films deposited in this research have been with II/VI ratio between 1 and 4.

5.3.2 Photoassisted Growth

A small number of experiments were carried out using the photoassisted method described in chapter 1.10. These few thin films were deposited at II/I ratio of 3 and the UV/Vis light source switched on after the first quarter oscillation in the interferogram. This ensured that there was an absorbing layer of ZnO deposited on substrate before irradiation.

Under these conditions no significant change in growth rate was observed over the pyrolytically deposited films. One consideration for the unaffected growth rate may be that the irradiation at the substrate surface may not have been of sufficient intensity or power over zinc oxides absorption range (see figure 3.5.3 page 77), to stimulate a growth rate increase.

Another consideration is that the increases in growth rate seen in the ZnSe work of Fujita *et al.* [10] and Irvine *et al.* [11] occurred when using hydrogen as carrier gas.

Ahmed et al. [12] showed that in the photoassisted surface reactions, hydrogen radicals arising from the hydrogen carrier gas were the key to the mechanism responsible for growth rate increase (see chapter 2.10). When using a nitrogen carrier gas the hydrogen radical pathway is negated.

5.3.3 The Nucleation Delay

It is possible using the *in situ* interferometry technique to calculate the time taken for the thin film to nucleate on the substrate surface. The following assumptions are made for the data shown in figures 5.3.10 and 5.3.11; first the time taken for the precursors to reach the reaction zone, once switched to flow, is of the order of a few seconds and does not vary. Secondly, the deviation of reflected intensity from the base line is in response to the nucleation of the thin film on the substrate surface.

Figure 5.3.10 is a plot of nucleation delay time (seconds) as a function of substrate temperature ($^{\circ}\text{C}$) for films deposited at $\text{II}/\text{VI} = 3$. This data is taken from the *in situ* interferometry and shows that there is no correlation of delay time with substrate temperature. The nucleation delay times are wide ranging throughout the temperature range, the smallest nucleation delay was 33 seconds at $T_{\text{sub}} 219^{\circ}\text{C}$, and the largest nucleation delay; 716 seconds at $T_{\text{sub}} 260^{\circ}\text{C}$. The average nucleation delay for all temperatures was 267 seconds.

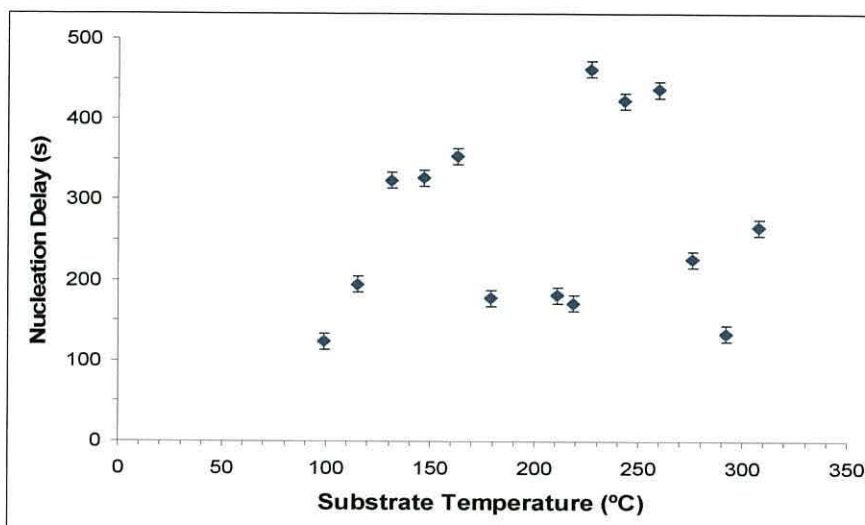


Fig. 5.3.10 a plot of nucleation delay time (seconds) as a function of substrate temperature (°C). For films deposited at $\text{II}/\text{VI} = 3$.

Figure 5.3.11 is a plot of nucleation delay time (seconds) as a function of substrate temperature (°C) for films deposited at $\text{II}/\text{VI} = 1$. There are not enough data points to comment on any correlation between nucleation delay and substrate temperature. The smallest nucleation delay was 117 seconds at $T_{\text{sub}} 243^\circ\text{C}$, and the largest nucleation delay; 1137 seconds also at $T_{\text{sub}} 243^\circ\text{C}$. The average nucleation delay for all temperatures is double that of $\text{II}/\text{VI} = 3$ at 519 seconds.

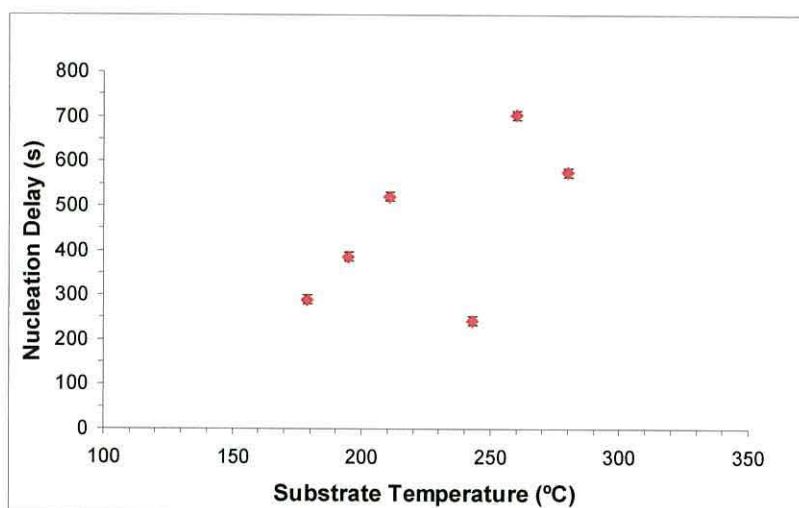


Fig. 5.3.11 a plot of nucleation delay time (seconds) as a function of substrate temperature (°C). For films deposited at $\text{II}/\text{VI} = 1$.

The plot of nucleation delay time versus substrate temperature, figures 5.3.10 and 5.3.11, show a wide scattering of data, for II/VI ratios of 3 and 1 respectively. There is however a doubling average nucleation delay time between II/VI equals 3 (267 seconds) and 1 (519 seconds). This effect may be explained by considering the effective supersaturation of Zn and O. A concentration of Zn and O at the substrate will be created by the reaction of the precursors and this needs to be greater than the equilibrium vapour pressure of Zn and O at the substrate temperature in order for a film to grow.

Under equimolar concentrations of DEZn and n-BuOH where the ZnO formation is governed by the slower step k_A in rate equation 5.3.1 the effective partial pressure of the reactant species and thus the effective supersaturation of Zn and O will be low. In this instance the effects of surface mobility will dominate allowing the adsorbed species to migrate to the lowest energy site for reaction. This selectivity of thin film growth effectively leads to a longer nucleation time and can lead to increased crystallinity.

Under higher partial pressures of DEZn the ZnO formation is governed by the faster step k_B in rate equation 5.3.1. In this instance the effective supersaturation of Zn and O is high and the effect of surface mobility is lessened as deposition takes place essentially at the site where adsorption initially occurs. This leads to the faster nucleation times observed under zinc rich conditions.

5.4 Optical and Electrical Properties

5.4.1 Pyrolytic Deposition

As discussed in chapter 1 the two key properties of a TCO are that they are highly transparent to visible wavelengths and offer minimal resistance to the current produced by the *p-n*-junction. Because TCOs are required to be transparent in the visible region the bandgap must be greater than 3 eV. The visible wavelength range is between 400 and 740 nm, where 400 nm is approximately equal to 3 eV. Thus a material with a bandgap of lower energy than 3 eV will begin to absorb light. The

bandgaps of the ZnO thin films deposited in this research can be seen to fall between 3.16 and 3.4 ± 0.02 eV thus satisfying the above requirement.

A further factor determining the transparency of a likely TCO material is the refraction of light within the material. In a single crystal with a bandgap of higher energy than 3 eV, visible light can be thought of as passing straight through the material being refracted only at the outer surfaces. The light is transmitted by the material in phase. The same scenario is true for an amorphous material which has no ordered atomic structure and hence gives rise to no refraction of transmitted light.

However, as discussed earlier, the zinc oxide thin films employed as TCOs are polycrystalline consisting of numerous grains of many orientations. When light rays pass through a polycrystalline material the light is refracted at each grain boundary. This means that light rays may follow quite different paths through the material and emerge out of phase. As a result of this scattering, transmission of light is reduced.

The transmission of light, in highly doped ZnO films, may also be affected by free carrier absorption. As the level of free carrier's increases, due to doping, the level of light absorbed by the free carriers is increased. The effect on transmission of this absorption by free carriers is clearly shown in figure 2.7.3 (page 35). However, the films deposited in this research were mostly of high resistance. For this reason it was assumed that the levels of free carriers, within the films, were low and would not significantly contribute to a loss in the film transmission.

The transparency of films obtained at $\text{II}/\text{VI} = 1$ (partial pressure 0.2mBar for both precursors) for different substrate temperatures is shown in figure 5.4.1. The spectra are typical of thin film ZnO where the transparency in visible wavelengths is high and the absorption edge, arising from energy absorbed by the thin films bandgap, is around 360 nm (3.3 eV).

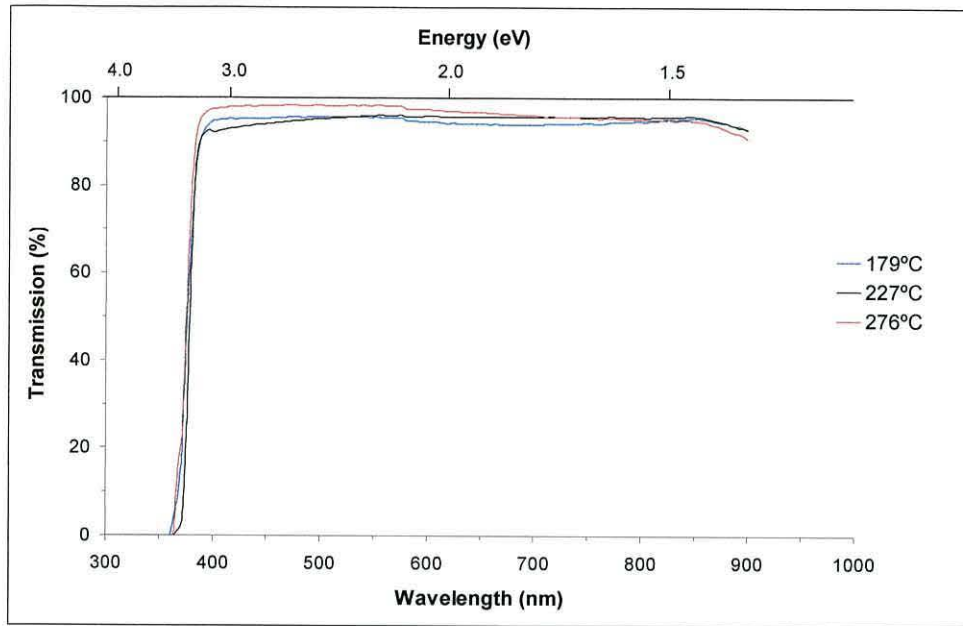


Fig. 5.4.1 Transmission (%) as a function of wavelength (nm) for ZnO thin film samples 034 (179°C) 330 nm thick, 031 (227°C) 500 nm thick and 035 (276°C) 300 nm thick, all deposited at $\text{II/VI} = 1$.

The absorption edges in figure 5.4.1 are very pronounced, allowing high transmission of wavelengths above 380 nm. From table 5.4.1 the average transmission of all three films can be seen to be well above 90%, with the highest substrate temperature resulting in the highest average transparency. The bandgap energies for the same samples are shown in figure 5.4.2 where a plot of $(\alpha E)^2$ versus (E) and the extrapolation of the linear portion of this curve to zero absorption coefficient provides the E_g energy (eV).

The bandgaps do not, within experimental error, vary with substrate temperature. These bandgaps for the 1:1 ZnO thin films are in the region of 3.16-3.19 eV and can be compared with the literature value of 3.3 eV [13] for the ZnO bulk semiconductor.

Sample	T. Sub. (°C)	II/VI Ratio	Ave. % T (400-900 nm)	Bandgap Energy (eV)
034	179 ± 1	1:1	94.8	3.16 ± 0.02
031	227 ± 1	1:1	95.3	3.17 ± 0.02
035	276 ± 1	1:1	96.5	3.19 ± 0.02

Table. 5.4.1 Optical properties of ZnO thin films deposited at II/VI =1, DEZn 0.2 mBar n-BuOH 0.2 mBar partial pressures.

The transparency of films obtained at II/VI = 3 (partial pressure DEZn 0.6 mBar/n-BuOH 0.2 mBar) precursor ratio for different substrate temperatures is shown in figure 5.4.3. The films deposited at 67 and 147°C display a high optical transparency with a distinct absorption edge and average transmission of 95.9 and 98%. The two films grown at 243 and 308°C have less distinct absorption edges and average transmissions of 90.4 and 81.5% respectively. On visual inspection the films revealed a brownish colour when grown at the highest substrate temperatures.

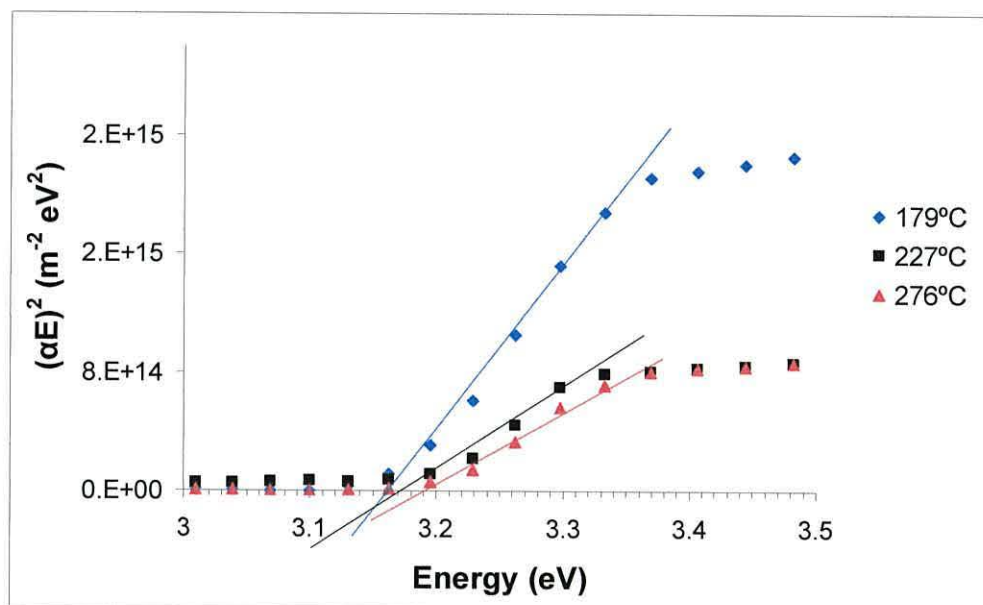


Fig. 5.4.2 Plot of $(\alpha E)^2$ as a function of E (eV) for ZnO thin film samples 034 (179°C), 031 (227°C) and 035 (276°C) deposited at II/VI = 1. The intercept of the energy axis by the straight line portion of the plot gives the optical bandgap energy.

This change in transmission spectra at high substrate temperatures and specifically at 308°C is a result of a change in surface morphology of the thin films. AFM

images for substrate temperature 243°C and 308°C are shown in figure 5.4.4 where a change in surface morphology from smooth to rough can be seen. The decrease in transmission is due to an increase of reflectivity and scattering by the rough films.

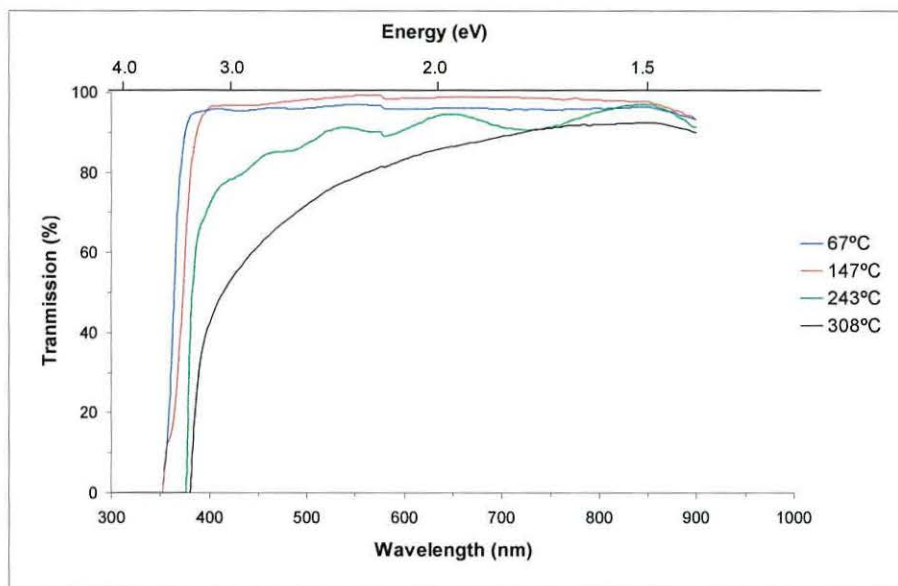


Fig. 5.4.3 Transmission (%) as a function of wavelength (nm) for ZnO thin film samples 093 (67°C), 085 (147°C), 077 (243°C) and 078 (308°C) deposited at II/VI = 3. All films were 500 nm thick.

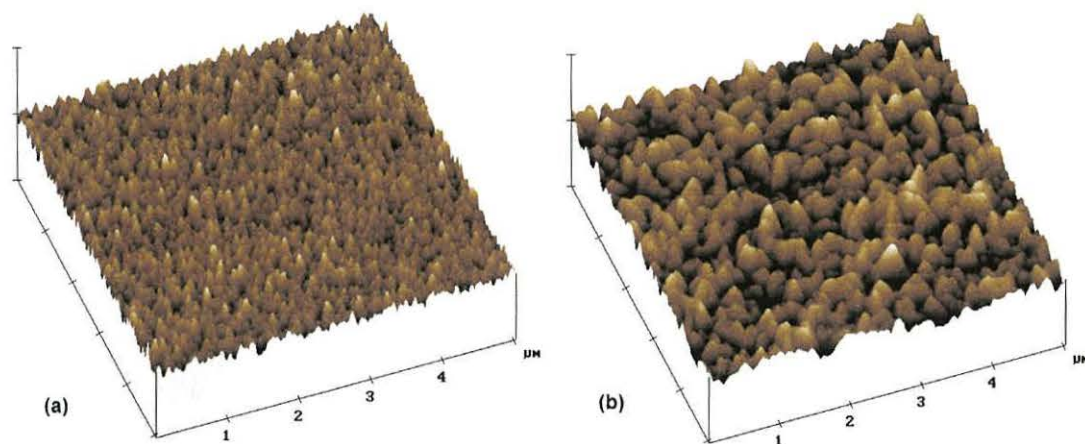


Fig. 5.4.4 AFM images of ZnO thin films 077 and 078 deposited at different temperatures and a II/VI = 3. The AFM was operated in contact mode, the scale bar shows 0-5 μm . (a) sample 077 (243°C). (b) sample 078 (308°C).

Table 5.4.2 displays the optical properties of the ZnO thin films deposited at II/VI = 3 and varying temperatures.

Sample	T. Sub. (°C)	II/VI Ratio	Ave. % T (400-900 nm)	Bandgap Energy (eV)
093	67 ± 1	3:1	95.9	3.41 ± 0.02
085	147 ± 1	3:1	98.0	3.33 ± 0.02
077	243 ± 1	3:1	90.4	3.25 ± 0.02
078	308 ± 1	3:1	81.5	3.20 ± 0.02

Table. 5.4.2 Optical properties of ZnO thin films deposited at II/VI = 3; DEZn 0.6 mBar n-BuOH 0.2 mBar partial pressures.

The bandgaps of the II/VI = 3 films presented in table 5.4.2 are calculated from figure 5.4.5. These are of marked difference to those of the 1:1 films. The bandgap appears to move to lower energies as the substrate temperature increases. The only parameter changing is the deposition temperature. Under the II/VI = 3 conditions a decrease in the bandgap with increasing deposition temperature is shown in figure 5.4.6.

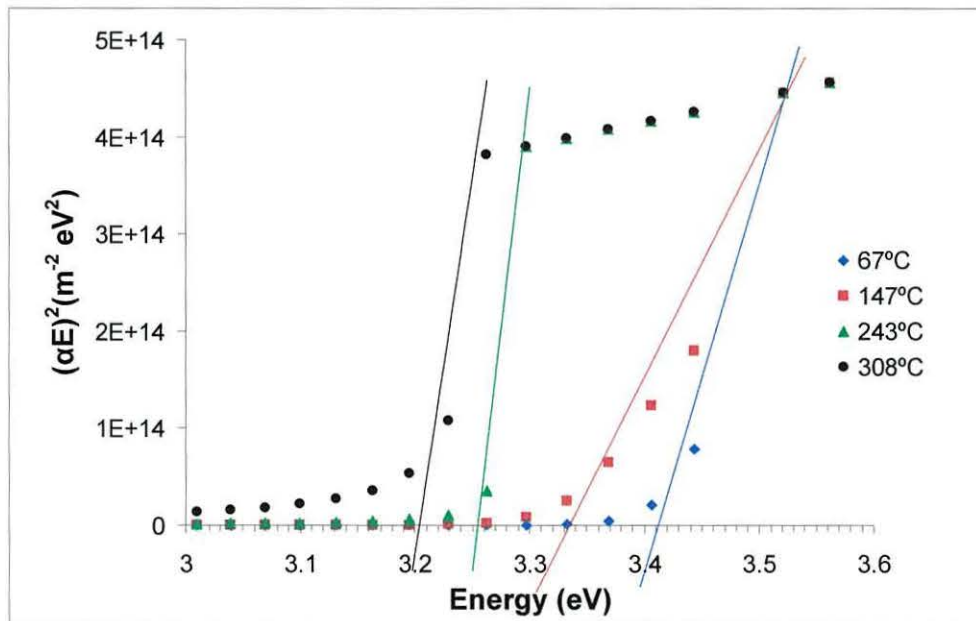


Fig. 5.4.5 Plot of $(\alpha E)^2$ as a function of E (eV) for ZnO thin film samples 093 (67°C), 085 (147°C), 077 (243°C) and 078 (308°C) deposited at a II/VI = 3. The intercept of the energy axis by the straight line portion of the plot gives the optical bandgap energy. All films were 500 nm thick.

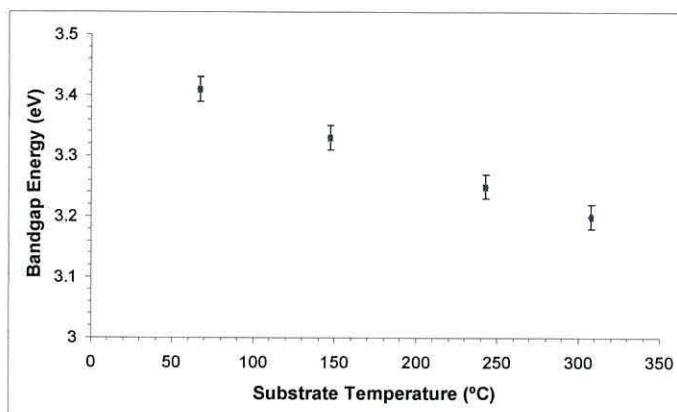


Fig. 5.4.6 Plot of Bandgap energy (eV) as a function of substrate temperature (°C) for ZnO thin film samples 093, 085, 077 and 078 deposited at different temperatures when II/VI = 3.

In figure 5.4.1 the transmission spectra of three films deposited at a II/VI ratio of 1 and three different substrate temperatures is shown. The absorption edge of each film is sharp and arises at the same part of the spectrum. The average transmission in the visible region was high for each film. When compared to figure 5.4.3, where the II/VI ratio was 3, two differences were observed with increasing substrate temperature; firstly the absorption edge became less defined, a phenomenon of scattering, and shifted to shorter wavelengths and secondly the average transmission decreased.

All three ZnO spectra shown in Figure 5.4.1 are ideal for the purpose of a thin film TCO. The wavelength range of transmitted light between 380 and 900 nm and above 90% transmission is well matched to the requirements of thin film photovoltaic materials. This consistency in optical properties, over a range of substrate temperatures, allows more choice of the temperature dependant properties such as growth rate and resistivity. However, the films in figure 5.4.3 are not all ideally optimized for TCOs, the two films deposited at 67 and 147°C are optically similar to those in figure 5.4.1. When moving to the substrate temperatures 243 and 308°C, at II/VI ratio of 3, the thin films become visibly darker in colour and display less favorable optical properties.

These results in figure 5.4.3 are in agreement with the work by Hahn *et al.* [5] where at low VI/II ratios and deposition temperatures of above 300°C, growth rates were high but films were reported to be milky in colour and brown at very low VI/II ratios.

Figures 5.4.2 and 5.4.5 reveal the bandgap energy of the thin films deposited under two different II/VI ratios. For a II/VI ratio of 1 the bandgaps of the three films are the same, within experimental error at around 3.17 eV. However, for the higher II/VI ratio of 3 there was a noticeable shift in bandgap with increasing deposition temperature. The bandgap energy decreased with increasing substrate temperature. A shifting of bandgap energy with deposition temperature is reported in the literature for various thin films.

Wenas *et al.* [14] deposited boron doped ZnO onto glass substrates at 150°C. It was observed that the bandgap of the films grown shifted due to changing the flow rate of the boron dopant source. With an increase in dopant concentration the bandgap shifted to a higher energy. This effect is known as the Burnstein-Moss shift. Wenas *et al.* [14] state that this arises due “in the heavily doped *n*-type semiconductor, the Fermi level is inside the conduction band and the states near the bottom of the conduction band are filled. Therefore, the absorption edge should shift to higher energy”.

In order to investigate whether this change in bandgap may be due to the Burnstein-Moss shift, the electrical properties of these films need to be discussed.

Table 5.4.3 shows the measured resistance, resistivity and sheet resistance for the commercial ITO sample along with the values provided by the manufacturers. Table 5.4.4 presents the electrical data of samples deposited at various temperatures and II/VI = 3. The resistivity is seen to decrease as the substrate temperature increases. There is however, an extremely significant 10^4 fold decrease in

resistivity between 243 and 308°C. Table 5.4.4 shows the best value of resistivity, for the TCO application, is $6.0 \times 10^{-3} \Omega \text{ cm}$ observed at 308°C.

	Sample	d (nm)	R (Ω)	ρ ($\Omega \text{ cm}$)	R_{sheet} (Ω)
Measured properties	ITO	1000	18.8	4.14×10^{-4}	4.14
Manufacturers specification				1×10^{-3}	10 ± 2

Table. 5.4.3 Commercial sample of tin doped indium oxide.

Sample	$T_{\text{substrate}}$ ($^{\circ}\text{C}$)	II/VI	d (nm)	R (Ω)	ρ ($\Omega \text{ cm}$)	R_{sheet} (Ω)
093	67	3	500	1.22×10^7	133.7	2.67×10^6
085	147	3	420	8.34×10^6	77.1	1.83×10^6
077	243	3	500	5.76×10^6	63.4	1.27×10^6
078	308	3	500	548	6×10^{-3}	121

Table. 5.4.4 Electrical properties of ZnO thin films deposited at different substrate temperatures and a II/VI = 3.

The results in table 5.4.4 show a trend of decreasing resistivity with increasing substrate temperature. This could be attributed to an increase in carrier concentration with increasing substrate temperature. Hall Effect measurements would give evidence for this but it was not possible to carry out these measurements. However, any increase in carrier concentration with increasing substrate temperature for these experiments would not be large enough to produce the heavily doped conditions required to produce the Burnstein-Moss shift seen in the work of Wenas *et al.* [14].

Table 5.4.2 shows the bandgap energy decreasing as the substrate temperature increases; the reverse effect to the Burnstein-Moss shift. Therefore the Burnstein-Moss shift effect can be ruled out as an explanation for the change in bandgap of the ZnO thin films. The decrease seen in the resistivity of the thin films with increasing deposition temperature may be a feature of a change in the materials crystalline. It is known that, for ZnO, crystalline quality improves with increasing

substrate temperature. Wenas *et al.* [14] observed a changing resistivity with deposition temperature and attributed it to an altering preferred crystal orientation or grain structure. As discussed in chapter 1.2 the mobility of carriers is increased with increasing crystalline quality and this improvement in electrical transport leads to an expected decrease in resistivity of ZnO with increasing deposition temperature.

This decrease in bandgap energy with increasing substrate temperature may be due to a change in the stoichiometry between zinc and oxygen atoms within the ZnO lattice. Any ratio of Zn to O above 1 will introduce lattice strain and this change in lattice parameter is known to alter the bandgap. Another consideration may be the incorporation of hydrogen into the ZnO lattice and how this may change with substrate temperature.

Undoped ZnO thin films are predominantly *n*-type semiconductors. Traditionally this *n*-type conductivity has been attributed to native defects (Look *et al.* [15]). These include the formation of interstitials and vacancies, of differing degrees, of both zinc and oxygen atoms. The stoichiometry of zinc to oxygen tends to be greater than one leading to zinc interstitials and oxygen vacancies. Only vacancies have been shown to have sufficiently low energies to form during the deposition of ZnO, and both zinc and oxygen vacancies have recently been shown (Kohan *et al.* [16]) to behave as deep acceptors and deep donors respectively. Being deep donors, the oxygen vacancies would not contribute to the *n*-type conductivity of ZnO. These observations lead to an ambiguity as to the nature of the *n*-type conductivity in ZnO.

Van de Walle [17] theoretically suggests that incorporated hydrogen is an excellent candidate for the *n*-type conductivity in ZnO. Firstly it is noted that hydrogen is ever present in the crystal growth techniques employed to deposit ZnO. Hydrogen is known to form a strong bond with oxygen and thus could be expected to be incorporated into the ZnO lattice. Van de Walle [17] states that “the resulting O-H

bonding unit can, in fact, be regarded as a new type of dopant atom, the addition of the proton turning the oxygen into an element behaving much like fluorine". From figure 5.3.5 it can be seen that hydrogen radicals are to be expected as products of reaction and may further be incorporated into the ZnO thin film.

The idea that hydrogen may act as a donor impurity enhancing the n-type properties of ZnO is counterintuitive to hydrogen's behaviour in other semiconductor materials. In all other semiconductors hydrogen is found to act as a compensating centre effectively passivating the existing conductivity of the material. Van de Walle [17] states that in all semiconductors except ZnO "interstitial hydrogen has been shown to act as an amphoteric impurity: in *p*-type material, hydrogen incorporates as H^+ (a donor), and in *n*-type material as H^- (an acceptor)".

Van de Walle [17] shows that, in ZnO, hydrogen occurs only in the H^+ state thus acting as a donor. This fact suggests that intentional incorporation of hydrogen in the ZnO lattice should lead to the material displaying increased conductivity. In a response, to theoretical work by Van de Walle [17], Cox et al. [18] provide experimental evidence that hydrogen interstitial can provide a donor level just below the conduction band in ZnO.

The experiment by Cox *et al.* [18] involved the use of an elementary particle the muon (μ) which, having a mass of 1/9 of a proton and a positive charge, can be treated like a light isotope of hydrogen. The sample was bombarded by pulses of muons which were produced by the decay of protons to pions and then pions to muons within a synchrotron. Inside the sample the muons can pick up an electron and become 'muonium' $Mu (\mu^+e^-)$. When this happens the muonium acts like a light hydrogen atom.

Information about the effects of the local environment of the implanted muonium is then gained from one of its products of decay a positron which is emitted preferentially along the instantaneous direction of the muons spin. Studying a

powder sample of ZnO Cox *et al.* [18] identified muonium acting as a shallow donor some 60 ± 10 meV below the conduction band. Cox *et al.* [18] concluded that hydrogen impurities can play a significant role in the electrical activity of ZnO. If hydrogen incorporation could be shown to be correlated to deposition temperature, within the DEZn/n-BuOH system, the changing resistivity and bandgap energy results of table 5.4.4 and figure 5.4.6 may be explained.

In order to distinguish the mechanism giving rise to a decrease in bandgap energy with increasing substrate temperature, for II/VI ratios of 3, further experiments would need to be carried out. To this end X-ray diffraction (XRD) could be used to give accurate lattice parameters of films displaying a changing bandgap with substrate temperature. The photo-luminescence (PL) spectra of the thin films could provide information on the specific defect centres. Ultra high vacuum secondary ion mass spectrometry (UHV-SIMS) could be used to detect the presence of hydrogen incorporated within the ZnO lattice. Identifying a change in the zinc oxygen stoichiometry of the thin film with substrate temperature would give evidence as to the cause of the observed bandgap shift.

Figure 5.4.7 shows the effect on transmission spectra of increasing the II/VI ratio whilst maintaining a constant substrate temperature. All parameters except II/VI ratio were kept constant. There is clearly an influence on the transmission spectra at different II/VI ratios. At II/VI = 2 the absorption edge is sharp and well-defined and the average transmission is 86.0 %. At II/VI = 3, the absorption edge is again sharp and well-defined and the average transmission is higher at 93.1 %. At II/VI = 4 the absorption edge is well defined but the average transmission is noticeably low at 55.0 %.

Whilst the absorption edge remained sharp for all three samples, a peak in percentage transmission was seen for II/VI equals 3 and a significant decrease in transmission was noted for II/VI equals 4. In the case of the transmission spectra

for II/VI equal to 4 the greater film thickness needs to be taken into account as a possible cause of the decrease in transmission.

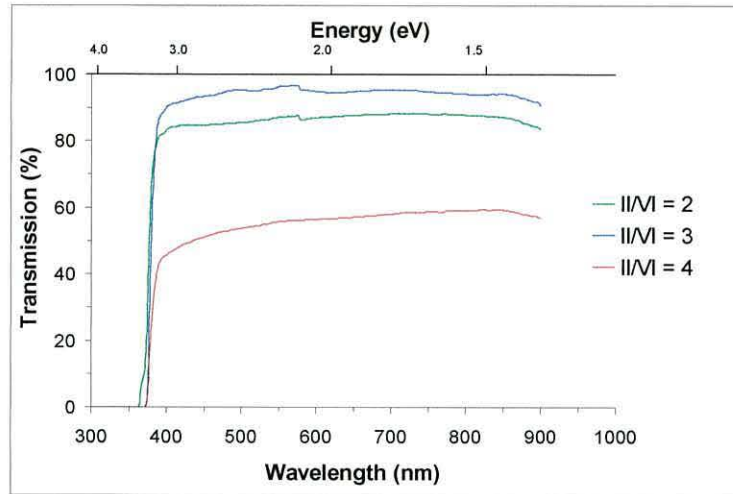


Fig. 5.4.7 Transmission (%) as a function of wavelength (nm) for ZnO thin film samples 045, 072 and 055 deposited at 227°C and varying II/VI ratios from 2 to 4 respectively.

Figure 5.4.8 is a plot of the bandgap energies for the ZnO films deposited at varying II/VI ratios. The bandgap energies of all 3 samples are seen not to vary within experimental error.

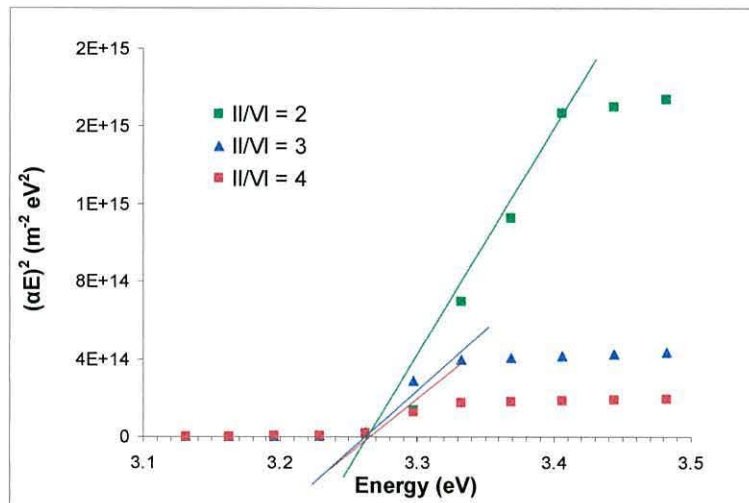


Fig. 5.4.8 Plot of $(\alpha E)^2$ as a function of E (eV) for ZnO thin film samples 045, 072 and 055 deposited at 227°C and varying II/VI ratios from 2 to 4 respectively. The intercept of the energy axis by the straight line portion of the plot gives the optical bandgap energy.

Table 5.4.5 displays the optical properties for the ZnO thin films deposited at varying II/VI ratios.

Sample	Thickness (nm)	T. Sub. (°C)	II/VI	Ave. % T (400-900 nm)	Bandgap Energy (eV)
045	250 ± 18	227 ± 1	2	86.0	3.26 ± 0.02
072	500 ± 35	227 ± 1	3	93.1	3.26 ± 0.02
055	750 ± 53	219 ± 1	4	55.0	3.26 ± 0.02

Table. 5.4.5 Optical properties of ZnO thin films deposited at varying II/VI ratios.

If the shifting of bandgaps was an aspect of varying the II/VI ratio table 5.4.5 would be expected to show some change in bandgap energy between the three samples. In fact table 5.4.5 demonstrates that, at 227°C, the II/VI ratio has no significant influence on the bandgap energy. Due to the limited results for II/VI ratios other than 1 and 3 it can be concluded that:

1. For a II/VI ratio of 3 an increase in substrate temperature decreases the bandgap energy. This may be due to a change in the ZnO stoichiometry or defect incorporation shifting the lattice parameter.
2. Changing the II/VI ratio at a fixed substrate temperature of 227°C does not affect the bandgap energy. At this deposition temperature the aspects responsible for the change in bandgap energy do not alter with increasing zinc partial pressure.
3. The bandgap energy does not change with substrate temperature when II/VI ratio equals 1. The aspects responsible for the change in bandgap energy do not alter with substrate temperature, or are not active, when equimolar partial pressures of DEZn and n-BuOH are present and the reaction follows the slower k_A rate in equation 5.3.1

5.4.2 Photoassisted growth

The transmission of photoassisted (PA) films grown compared to non-photoassisted is shown in figure 5.4.9. The transmission spectra of the films grown at low temperature (67°C) are identical. Both have a sharp absorption edge with a high

average transmission of 95.8% and 95.9% for the PA and non-PA films respectively. The transmission of the samples grown in the optimum growth temperature regime is again very similar.

The average transmission is high for both films at 95.3% and 94.4% for the PA and non-PA films respectively. There is however a noticeable difference in the absorption edge. While the non-PA grown film has a sharp absorption edge, the PA film has a broader more rounded absorption edge. This may be as a result of a change in surface morphology of the PA sample giving rise to increased scattering of the spectrometer beam.

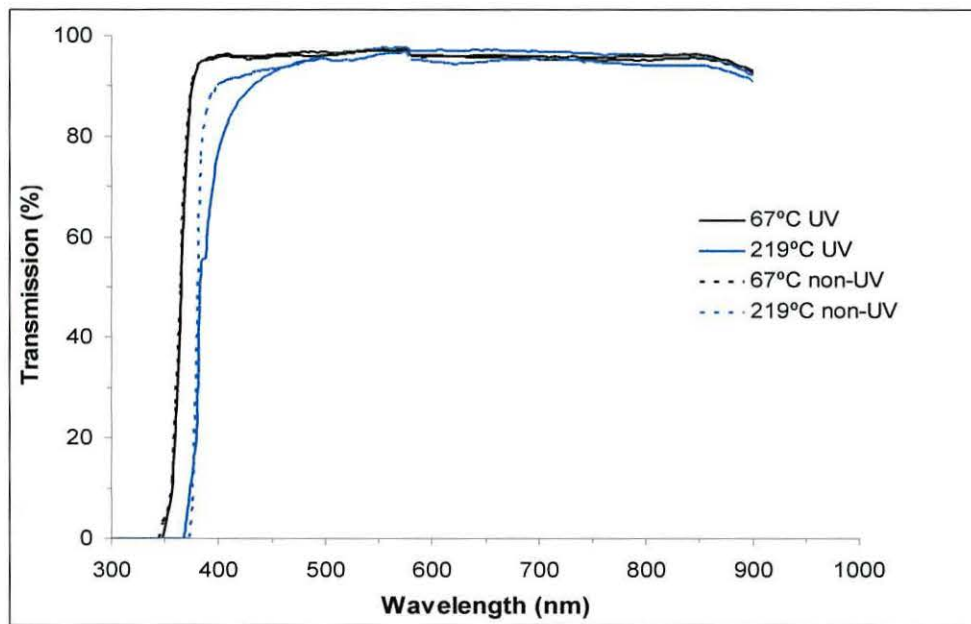


Fig. 5.4.9 Transmission (%) as a function of wavelength (nm). Photoassisted thin film samples 096 (67°C), 068 (219°C) and non-photoassisted samples 093 (67°C), 072 (219°C). All films ca-0.5 μm and deposited at II/VI = 3. UV/Vis lamp power at substrate = 23.6 mW/cm².

The bandgap energies of the samples are calculated from figure 5.4.10 and displayed in table 5.4.6. As seen in the non-PA results there is a marked difference in bandgap energies of films grown at different temperatures exclusive of any PA effects. At low temperature there is no significant effect on the bandgap energy of

PA growth. In the optimum growth temperature regime the effect of PA growth on the bandgap is to slightly raise the energy from 3.28 to 3.32 eV.

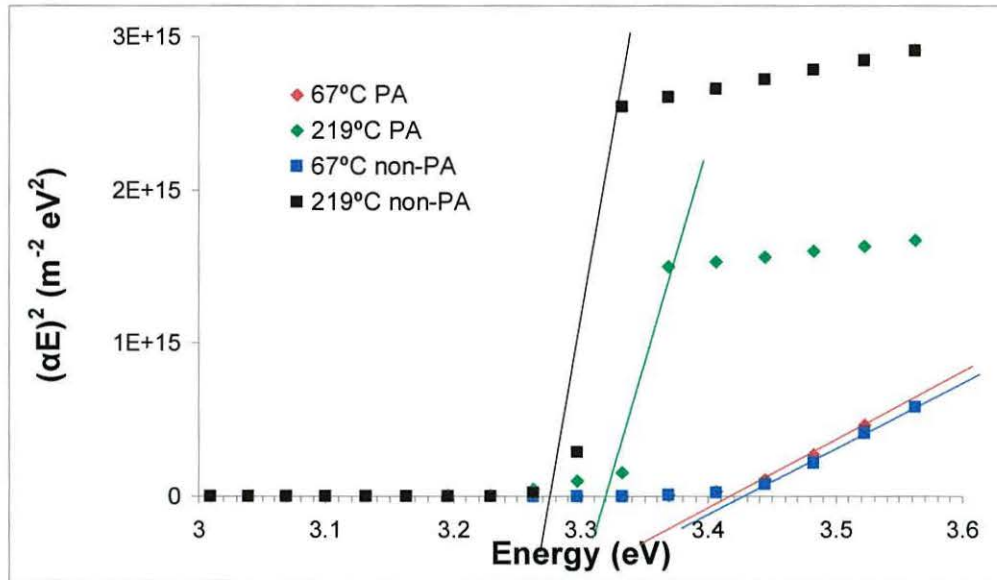


Fig.5.4.10 Plot of $(\alpha E)^2$ as a function of E (eV) for photoassisted thin film samples 096 (67°C), 068 (219°C) and non-photoassisted samples 093 (67°C), 072 (219°C). All films ca~0.5 μm and deposited at II/VI = 3. UV/Vis lamp power at substrate 23.6 mW/cm².

Sample	T. Sub. (°C)	II/VI	Ave. % T (400-900 nm)	Bandgap Energy (eV)
096PA	67 ± 1	3	95.8	3.40 ± 0.02
093	67 ± 1	3	95.9	3.40 ± 0.02
068PA	219 ± 1	3	95.3	3.32 ± 0.02
072	219 ± 1	3	94.4	3.28 ± 0.02

Table. 5.4.6 Optical properties of photoassisted versus non-photoassisted ZnO thin films deposited at II/VI = 3. UV/Vis lamp power at substrate 23.6 mW/cm².

Figure 5.4.10 shows the influence of a UV/Vis (23.6 mW/cm²) source irradiating the growing film at a II/VI ratio of 3 and two different substrate temperatures. The photo-irradiation does not bring about any significant change in bandgap energy or transmission.

Figure 5.4.11 displays the transmission spectra for two films deposited in the high temperature regime. For the PA sample the power of the UV/Vis lamp was

increased by a third to 36.8 mW/cm^2 . The PA film, although in every other way deposited under the same conditions, exhibits a discernible difference in transmission spectra compared to the non-PA deposited film. The absorption edge for the PA sample is sharp and well defined and the average transmission is 84.7%. However, the non-PA deposited film has a broad undefined absorption edge and a lower average transmission of 81.5%.

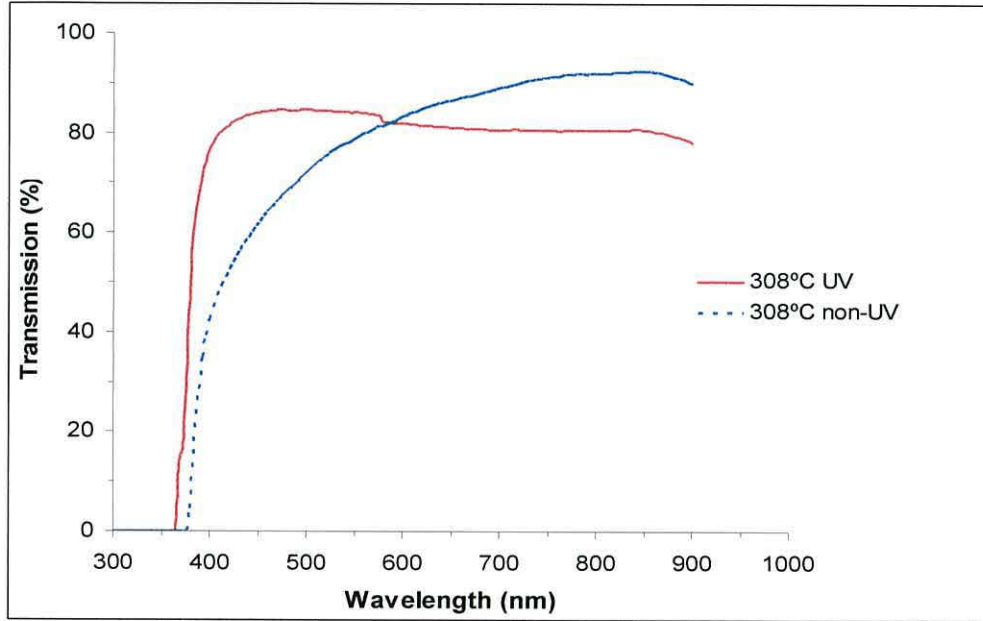


Fig. 5.4.11 Transmission (%) as a function of wavelength (nm). Photoassisted $0.8 \mu\text{m}$ thin film sample 110 (308°C) and non-photoassisted $0.5 \mu\text{m}$ sample 078 (308°C). Both films deposited at $\text{II/VI} = 3$. UV/Vis lamp power at substrate = 36.8 mW/cm^2 .

The bandgap energies of the two films are calculated in figure 5.4.12 and shown in table 5.4.7. The PA film has a significantly higher bandgap energy of 3.37 eV compared to the non-PA films 3.24 eV . 3-Dimensional AFM images of the two samples are shown in figure 5.4.13. These reveal a difference in surface morphology between the non-PA and PA films.

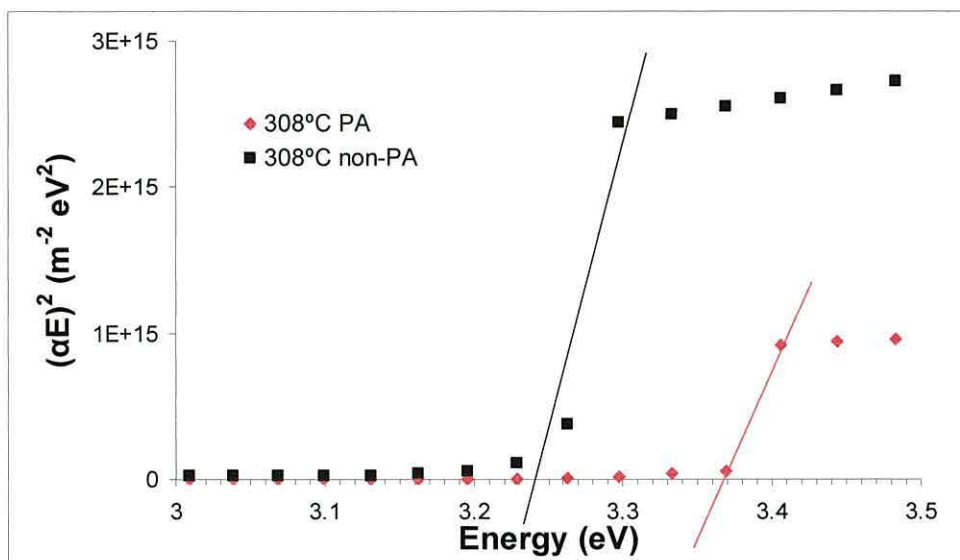


Fig. 5.4.12 Plot of $(\alpha E)^2$ as a function of E (eV) for photoassisted 0.8 μm thin film sample 110 (308°C) and non-photoassisted 0.5 μm sample 078 (308°C). All films ca~0.5 μm and deposited at II/VI = 3. UV/Vis lamp power at substrate = 36.8 mW/cm².

Sample	T. Sub. (°C)	II/VI	Ave. % T (400-900 nm)	Bandgap Energy (eV)
110PA	308 ± 1	3	84.7	3.37 ± 0.02
078	308 ± 1	3	81.5	3.24 ± 0.02

Table. 5.4.7 Optical properties of photoassisted versus non-photoassisted ZnO thin films deposited at II/VI = 3. UV/Vis lamp power at substrate 36.8 mW/cm².

From these results there is now a fourth conclusion to be drawn on the shifting bandgap energy within these ZnO thin films.

- 4 At 308°C the irradiation by UV/Vis energy, on the growing film, increases the bandgap energy.

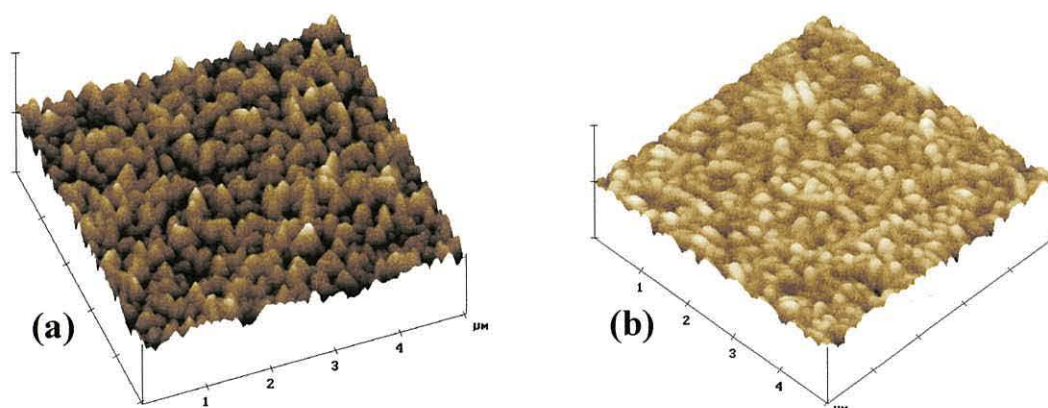


Fig. 5.4.13 AFM images of ZnO thin films 078 (non-photoassisted) and 110 (photoassisted) deposited at $\text{II/VI} = 3$. The AFM was operated in contact mode, the scale bar shows 0-5 μm . (a) sample 078 (308°C). (b) sample 110 (308°C).

Film (a) in figure 5.4.13 was deposited via the non-PA method and the 5 μm^2 AFM sample area gave a roughness (r.m.s.) of 24.1 nm. Film (b) was deposited using the PA method and the 5 μm^2 AFM sample area gave a roughness (r.m.s.) of 25.5 nm. These values are very similar and would not account for the differences noted from the transmission spectra. However, image (a) shows a peaky surface with an average grain size of 239 nm whereas image (b) shows a hilly surface with an average grain size of 250 nm.

Table 5.4.8 presents the electrical data of samples deposited at various temperatures and $\text{II/VI} = 1$. The resistivity is seen to slightly increase as the substrate temperature increases. The lowest value of resistivity, 51.7 $\Omega \text{ cm}$ at 179°C, is seen to be 10^5 higher than that of the ITO sample.

Table 5.4.9 presents the electrical data of samples deposited at various II/VI values and a constant substrate temperature 227°C. The lowest value of resistivity, 5.8 $\Omega \text{ cm}$, is obtained at $\text{II/VI} = 4$. However, at 227°C, there appears to be no discernable trend in the resistivity values for different II/VI ratios.

Sample	T _{substrate} (°C)	II/VI	d (nm)	R (Ω)	ρ (Ω cm)	R _{sheet} (Ω)
034	179	1	330	7.12 x 10 ⁶	51.7	1.57 x 10 ⁶
031	227	1	550	4.3 x 10 ⁶	52.0	9.46 x 10 ⁵
035	276	1	330	1.7 x 10 ⁷	123.4	3.74 x 10 ⁶

Table. 5.4.8 Electrical properties of ZnO thin films deposited at different substrate temperatures and a II/VI = 1.

Sample	T _{substrate} (°C)	II/VI	d (nm)	R (Ω)	ρ (Ω cm)	R _{sheet} (Ω)
031	227	1	550	4.3 x 10 ⁶	52.0	9.46 x 10 ⁵
045	227	2	250	2.8 x 10 ⁷	154	6.16 x 10 ⁶
072	227	3	500	5.25 x 10 ⁶	57.8	1.16 x 10 ⁶
055	227	4	750	3.5 x 10 ⁵	5.8	7.7 x 10 ⁴

Table. 5.4.9 Electrical properties of ZnO thin films deposited at 227°C substrate temperature and increasing II/VI ratios.

The results in table 5.4.4 (page 128) are in line with those of Hahn *et al.* [5] who deposited undoped ZnO thin films by MOCVD using DMZn and t-BuOH. The thin films resistivities were shown to decrease with increasing deposition temperature with the lowest figure of $7 \times 10^{-2} \Omega \text{ cm}$ at 360°C. The results in table 5.4.4 compare favourably with the work of Hahn *et al.* [5]; a lower resistivity of $6 \times 10^{-3} \Omega \text{ cm}$ was found at a lower deposition temperature of 308 °C.

Oda *et al.* [3] deposited undoped ZnO by MOCVD again from DEZn and t-BuOH giving resistivities, at 300°C, of around 1 Ω cm. Again it was noted that as the deposition temperature decreased the resistivity increased, at 150°C the resistivity was 100 Ω cm. Oda *et al.* [3] in 1985 proposed that the low resistivities, for undoped films, may be caused by a degenerated donor level resulting from oxygen vacancies. This train of thought is contrary to the recent work of Kohan *et al.* [16] who describe oxygen vacancies to behave as deep donors and therefore not contribute to the majority carriers.

Natsume *et al.* [19] deposited ZnO by MOCVD using the precursors zinc acetylacetonate (ZnAA) and water. The minimum resistivity of 2.2 Ω cm was found at 550°C. The resistivity was seen to increase at temperatures above and below this value. The films had a preferred 002 orientation, Natsume *et al.* [19] noted that the width of the 002 peak at 500 and 600°C did not change and therefore the electron mobility was not influenced by grain size. The changes in resistivities were attributed to be from changes in carrier concentrations of the films. It was also stated by Natsume *et al.* [19] that “the decomposition of ZnAA at higher temperatures and its subsequent oxidation is more active. Hence more perfect polycrystalline films are formed which do not include the defects producing donor levels causing lower resistivity”.

This work, although using alternative precursors, gives information on the electrical properties of ZnO thin films formed at higher temperatures than typically reported in this thesis. It is seen that although resistivity generally decreases with deposition temperature a minimum will be reached where moving to higher temperatures leads to an increase in resistivity.

The decrease in resistivity in table 5.4.4 is in agreement with the work of Oda *et al.* [3]. However, the explanation involving oxygen vacancies must be treated with caution following the work of Kohan *et al.* [16] described previously. Two factors which are related to substrate temperature are suggested for the improvement of resistivity:

1. Resistivity can increase with improved crystallinity in the undoped ZnO thin film.
2. Resistivity can increase with increased carriers that result from defects more likely to form at higher temperatures.

In table 5.4.8 the resistivity of the films deposited at II/VI ratio of 1 and various substrate temperatures were seen to be similar to each other not following the deposition temperature dependant trend shown by the data in table 5.4.4. This may be due to any change in resistivity not being apparent over the smaller temperature range measured. If these results are not just a feature of the small temperature range they may indicate that only when deposition takes place in zinc-rich conditions does the resistivity decrease with increasing substrate temperature.

Evidence for this hypothesis is seen in table 5.4.9 where at a fixed substrate temperature the influence of zinc-rich growth on resistivity was investigated. The resistivity decreased from 154 Ω cm at a II/VI of 2, to 57.8 Ω cm at II/VI of 3, and 5.8 Ω cm at a II/VI of 4. Under zinc-rich conditions the thin film grows via the fast radical mechanism identified in figure 5.3.6. It may be as a result of this increased growth rate with increased zinc concentration that the films crystalline and therefore electrical properties are modified.

Table 5.4.10 shows the electrical properties of ZnO thin films deposited by photoassisted MOCVD with UV/Vis power at the substrate = 23.6 mW/cm². For comparison table 5.4.11 displays the properties of ZnO thin films deposited under the same conditions except without photoassistance. The resistivity of photoassisted deposited films decreases as substrate temperature increases. The lowest resistivity value of 1.5×10^{-2} Ω cm, at 308°C, was 10^4 fold lower than that at 219°C. Sample 035PA gives a resistivity that is only 10 times higher than that of the commercial ITO sample.

In figure 5.4.14 the resistivities of the films deposited via photoassisted and non-photoassisted at different substrate temperatures are compared. The photoassisted films have a factor of approximately 3 times higher resistivities than the films deposited by purely thermal MOCVD.

Sample	T _{substrate} (°C)	II/VI	d (nm)	R (Ω)	ρ (Ω cm)	R _{sheet} (Ω)
096PA	67	3	500	3.19 x 10 ⁷	351	7.02 x 10 ⁶
068PA	219	3	660	1.69 x 10 ⁷	245	3.71 x 10 ⁶
035PA	308	3	835	805	0.015	177

Table. 5.4.10 Electrical properties of ZnO thin films deposited by photoassisted MOCVD at different substrate temperatures and a II/VI = 3. UV/Vis lamp power at substrate = 23.6 mW/cm².

Sample	T _{substrate} (°C)	II/VI	d (nm)	R (Ω)	ρ (Ω cm)	R _{sheet} (Ω)
093	67	3	500	1.22 x 10 ⁷	133.7	2.67 x 10 ⁶
072	219	3	500	5.25 x 10 ⁶	57.8	1.16 x 10 ⁶
078	308	3	500	548	6.0 x 10 ⁻³	120.6

Table. 5.4.11 Electrical properties of ZnO thin films deposited at different substrate temperatures and a II/VI = 3.

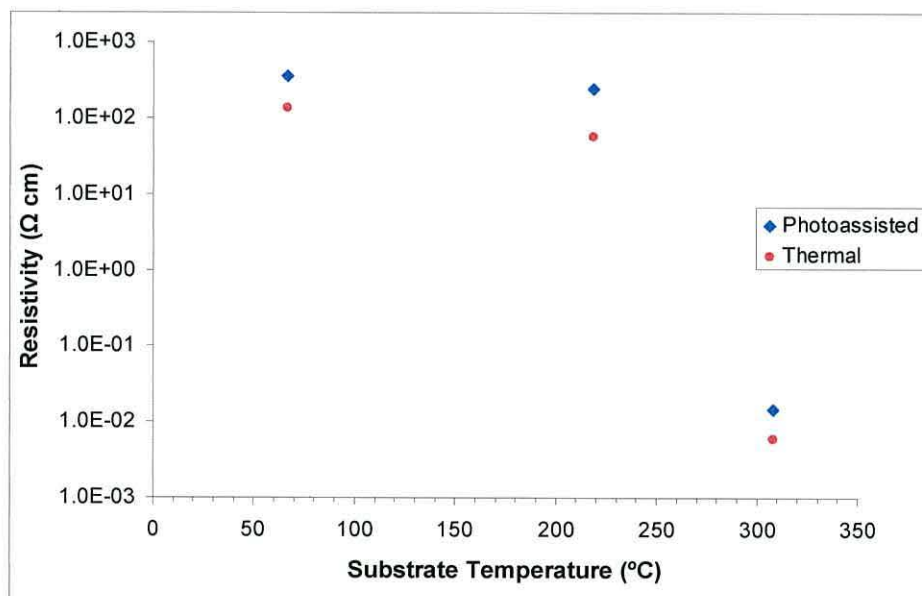


Fig. 5.4.14 A plot of resistivity (Ω cm) as a function of substrate temperature (°C) for films deposited by both thermal and photoassisted MOCVD. UV/Vis lamp power at substrate = 23.6 mW/cm².

Table 5.4.10 gives the electrical properties of the films deposited by the photoassisted method. A comparison in resistivity was made with films deposited under the same conditions but without photoassistance; the photoassisted films displayed a higher resistance at all three substrate temperatures. Figure 5.4.14 shows that at all three temperatures there was approximately a three fold increase in resistivity for the photoassisted method.

5.5 Thin Film Morphology

5.5.1 Pyrolytic Growth

Figure 5.5.1 is a plot of the root mean square (r.m.s.) roughness taken from $5\ \mu\text{m}^2$ AFM images of ZnO samples deposited at $\text{II}/\text{VI} = 3$; blue data and $= 1$; red data. For both, $\text{II}/\text{VI} = 1$ and 3, the roughness increases with increasing substrate temperature. At $\text{II}/\text{VI} = 1$ the roughness increases rapidly over the temperature range of 180-260°C.

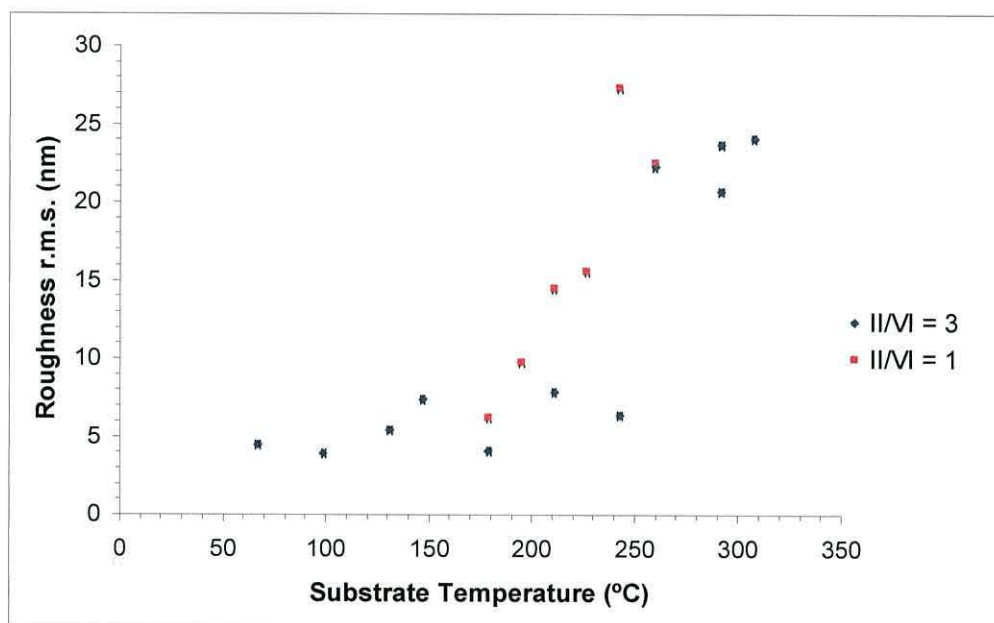


Fig. 5.5.1. Film roughness rms (nm) versus substrate temperature (°C). Data for films deposited at $\text{II}/\text{VI} = 3$ and 1 is plotted.

Figure 5.5.1. shows roughness (rms) increasing with deposition temperature. This corresponds well with the observations that, as an effect of scattering from this

increased roughening, the transmission of the films decreased with increasing deposition temperature. The step change in surface roughness seen between 240 and 260°C, when II/VI = 3, is a feature of a change in surface morphology which is clear in figures 5.5.2 and 5.5.7.

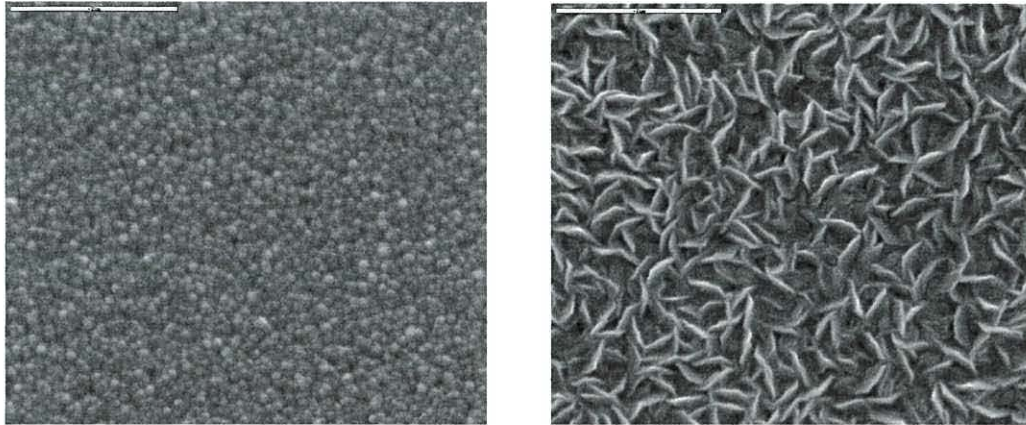


Fig. 5.5.2 SEM images of ZnO thin films. Left hand film deposited at 243°C and II/VI = 3. Right hand image deposited at 324°C and II/VI = 3. Scale bars = 2 μ m.

Up to 243°C the surface morphology has a macro-smooth appearance with grains having a conical shape normal to the substrate surface. At 276°C the surface morphology takes on a macro-rough appearance; the grains displaying a more ridge-like rough shape.

To understand the change in surface morphology with deposition temperature the underlying crystallinity needs to be considered. Figure 5.5.3 gives the XRD spectra of II/VI = 3 films deposited over a range of substrate temperatures; a transition in grain orientation from 243 to 308°C is clear.

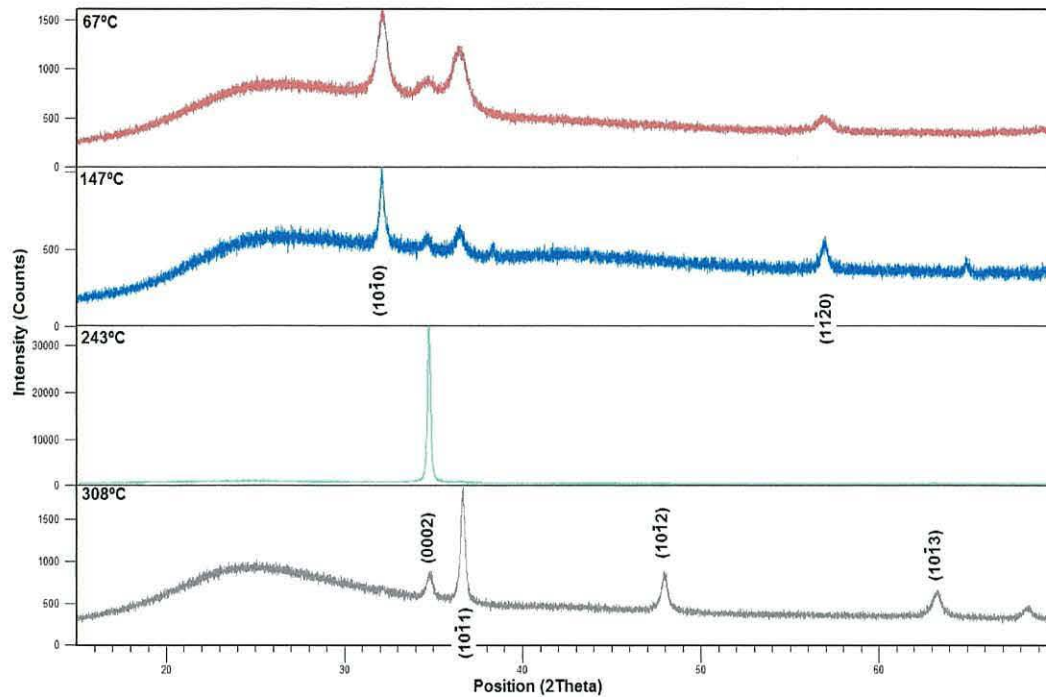


Fig 5.5.3 Intensity (counts) versus 2θ ZnO thin films deposited at II/VI ratio =3 and various substrate temperatures.

The films move from a predominantly (0002) preferred orientation at 243°C to predominantly the (10-11), (10-12) and (10-13) orientations at 308°C. This transition is further highlighted in figures 5.5.4. and 5.5.5. where films at both 219 and 243°C exhibit the (0002) orientation and those at both 276 and 292°C the (10-11), (10-12) and (10-13) orientations. The change in crystalline structure, between smooth and rough, for ZnO thin film deposited under these conditions is between 243 and 276°C.

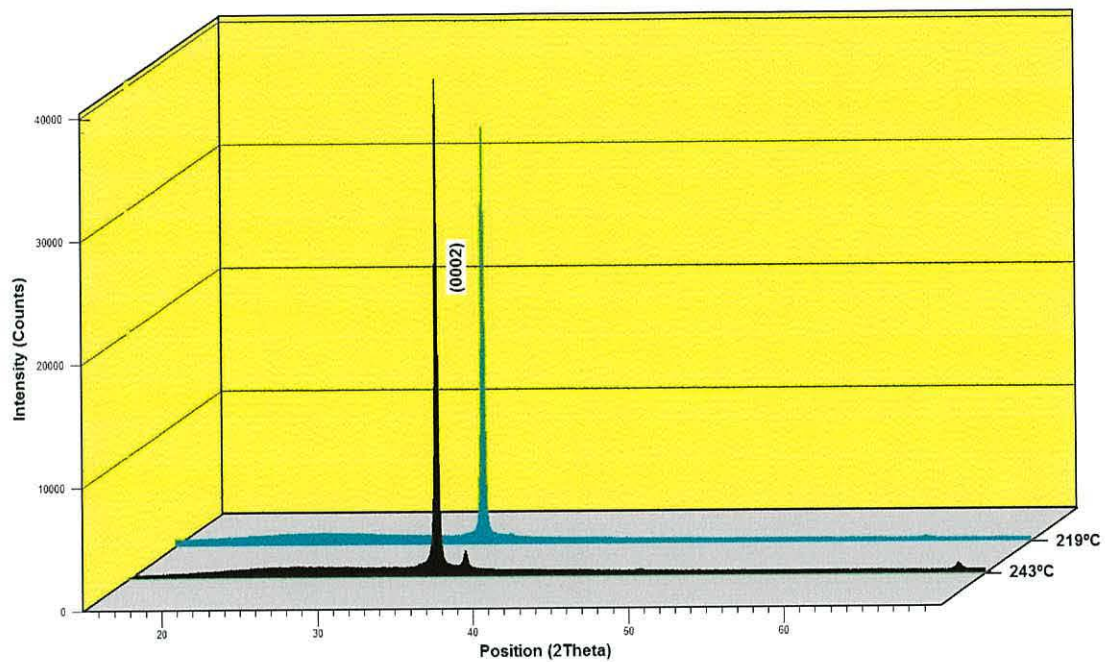


Fig 5.5.4 Intensity (counts) versus 2θ for ZnO thin films deposited at II/VI ratio = 3 and substrate temperature of 219 and 243°C.

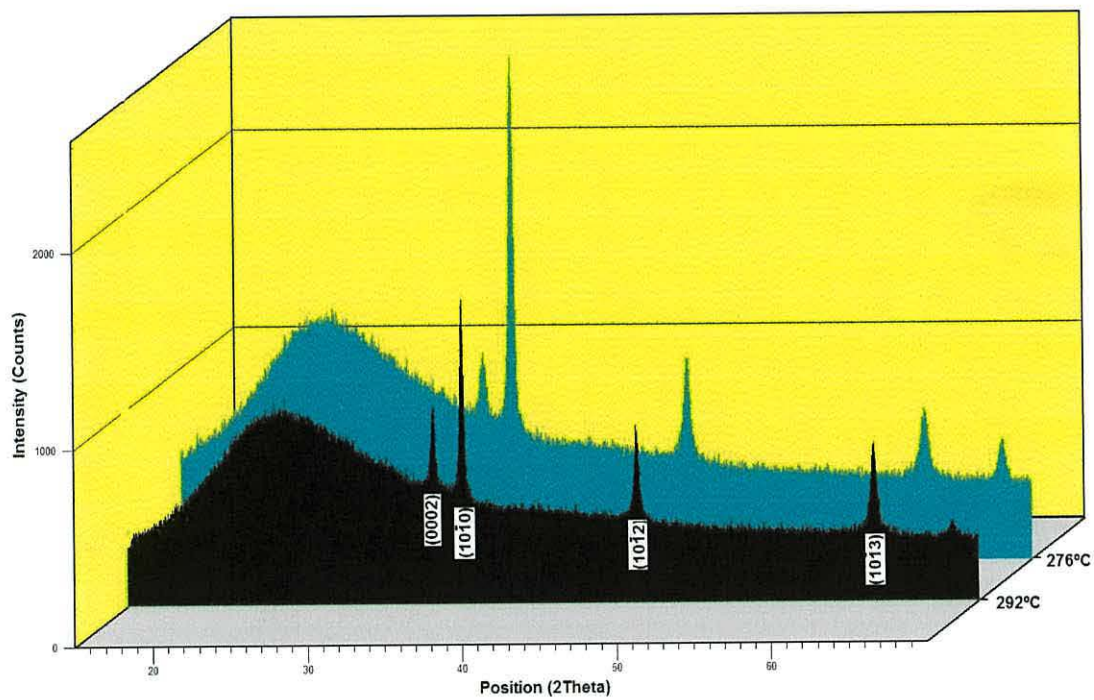


Fig 5.5.5 Intensity (counts) versus 2θ for ZnO thin films deposited at II/VI ratio = 3 and substrate temperature of 276 and 292°C.

The (0002) grain orientation represents the predominant growth direction being one where the c -axis of the hexagonal lattice is perpendicular to the substrate surface. This mode of growth results in a columnar-like structure to the thin film which is observed in figure 5.5.2(a) and gives the macro-smooth surface shown in figure 5.5.2(left). Where the dominant orientation is the (10-11), (10-12) and (10-13) group the c -axis can be thought as lying at one of three angles less than 90° to the substrate surface. These grain orientations result in the rough ridge-like grains observed in figure 5.5.2 (right).

These results on the identification and thus control of this change in crystallinity become important when considering the role these ZnO thin films play within the photovoltaic cell. The application of TCOs for thin film photovoltaics such as the CdTe/CdS system requires a smooth highly transparent layer. The TCO is effectively the template onto which the p - n junction is deposited and as such the morphology of the TCO is effectively replicated or magnified all the way through to the rear contact. However, when considering other photovoltaic systems such as CuInSe₂ (CIS) and amorphous silicon (α -Si) there is a requirement for the TCO to be rough.

Frammelsberger *et al.* [20] outline the advantages of a rough ZnO TCO for α -Si solar cells. They state that “in the case of superstrate cell structures, where illumination enters through the glass/TCO substrate, the texture is needed to raise the light absorption and thus to facilitate thinner absorber layers”. This increase in light absorption is as a result of a reduction in the incident light loss by reflection at the ZnO interface, and an increase in light scattering and trapping within the absorber layer.

The (0002) mode of growth is predominant at the maximum growth rate deposition temperature when effective supersaturation of Zn and O is highest. Also at maximum growth rate temperature the intensity of counts in the XRD spectra is high; relative to films grown at temperatures outside of the maximum growth rate

regime. This suggests that under the zinc rich condition ($\text{II}/\text{VI} = 3$), where k_B of equation 5.3.1. Dominates, the films grow with a high degree of preferred orientation in the (0002) plain.

At deposition temperatures higher than the maximum growth rate regime the (10-11), (10-12) and (10-13) group are observed. The surface energy is higher due to higher deposition temperature and the growth rate much reduced. For the application of TCO the crystallinity is shown to influence the electronic and optical properties of the thin films in conflicting ways.

1. At high deposition temperatures the resistivity decreases making the transport of photocurrent from the p - n junction more efficient.
2. At high deposition temperatures surface roughness increases reducing the optical transmission to the p - n junction.
3. At high deposition temperatures growth rate is low making large area production less economical.

Figure 5.5.6. is a plot of average grain size calculated from $5\ \mu\text{m}^2$ AFM images. The grain size for films deposited under $\text{II}/\text{VI} = 1$ conditions shows no clear dependence on deposition temperature but is generally larger than equivalent $\text{II}/\text{VI} = 3$ films. This increased grain size, when equimolar precursor partial pressures are employed, may be as a result of the 10 fold decrease in growth rate shown in figure 5.3.2. Often in crystal growth techniques the slower the formation of the crystallites or grains the larger they can become.

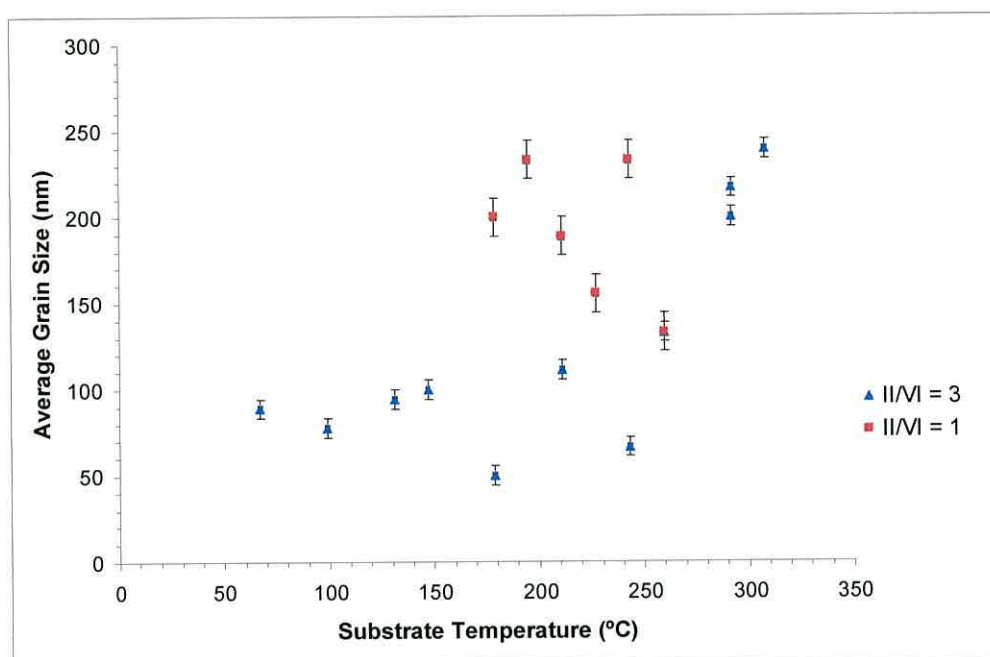


Fig. 5.5.6 Average grain size (nm) as a function of substrate temperature (°C). Data for films deposited at II/VI = 3 and 1 is plotted.

For II/VI = 3 the grain size is seen to make a step increase in the same deposition range that was observed for surface roughness. This is proposed to be a similar phenomenon as above, where the move to the slow growth rate at higher temperatures, seen in figure 5.3.1, leads to larger grains. Following this argument larger grains may be expected when the growth rate is slow at low deposition temperatures. However,, these effects of slow growth rate on crystallite size are negated, in the low temperature regime, due to a lack of surface mobility of the atoms to support larger grain size formation.

Figure 5.5.7 shows AFM images of 6 films deposited at a II/VI ratio of 3 and an increasing substrate temperature. A change in surface morphology from a macro-smooth appearance up to 243°C to a much rougher appearance at higher deposition temperatures is observed.

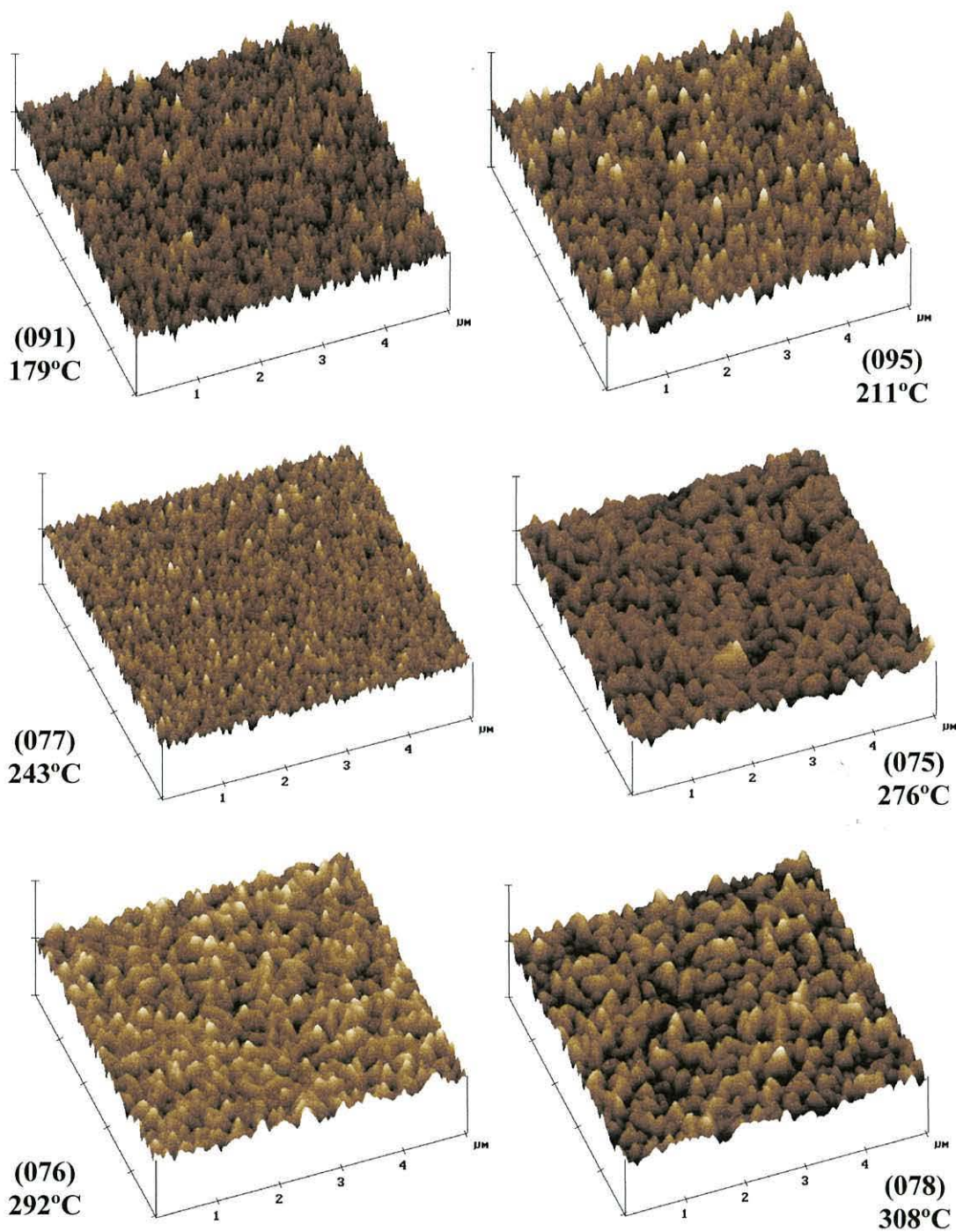


Fig. 5.5.7 AFM images revealing the changing surface morphology with increasing substrate temperature. Films deposited at II/VI ratio of 3.

5.5.2 Photoassisted Growth

A comparison of the surface morphology between ZnO films deposited under purely pyrolytic conditions and those deposited with the addition of UV/Vis

illumination was investigated using AFM. Figure 5.5.8 compares the roughness r.m.s. (nm) of pyrolytic and photoassisted films at different substrate temperatures. There is no significant difference in roughness at 67 and 308°C, however at 219°C there is a 2 fold increase in roughness. The AFM images of the 219°C films are shown in figure 5.5.9. Taking into account the difference in z-axis between the two AFM images (068PA z-axis = 100 nm/div and 072 = 200 nm/div) the surface of 068PA does appear rougher than 072.

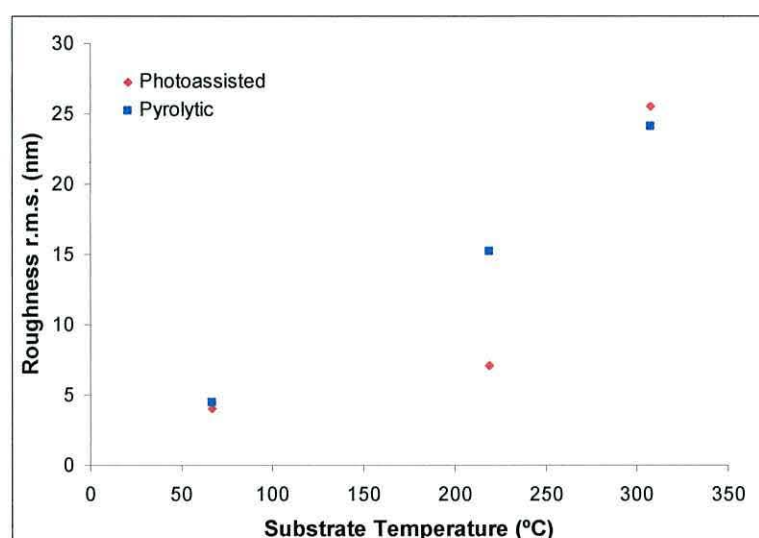


Fig. 5.5.8 Film roughness r.m.s. (nm) versus substrate temperature (°C) for both photoassisted and purely pyrolytically grown films. All films deposited at II/VI = 3. UV/Vis lamp power at substrate 23.6 mW/cm².

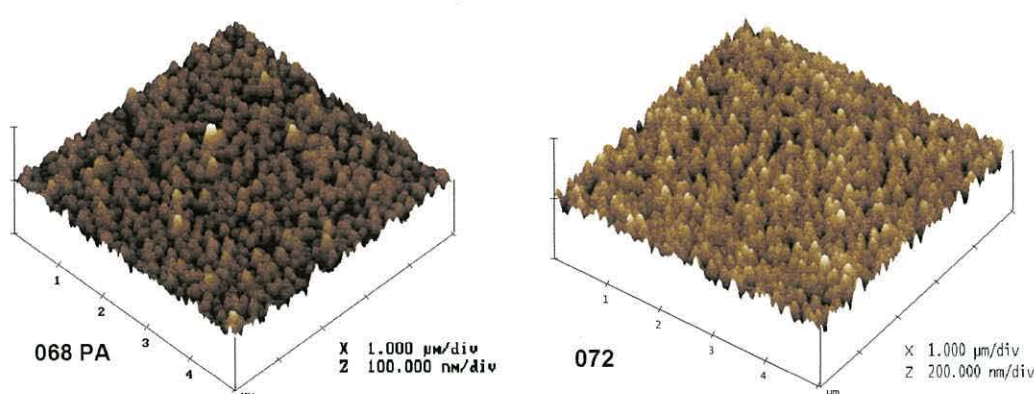


Fig. 5.5.9 AFM images of 068PA and 072 deposited at 219°C and II/VI = 3. The UV/Vis lamp power at substrate for 068PA was 23.6 mW/cm².

Figure 5.5.8 shows that at both the low and high substrate temperature there is no modification in surface roughness when the growing film is irradiated by the UV/Vis lamp (23.6 mW/cm^2). At 219°C there is a 2 fold increase in surface roughness when employing the photoassisted method. Evidence for this change in surface roughness is gained from figure 5.5.10 where the XRD spectra of the two films are presented. The photoassisted film has two additional reflections, the (10-10) and 11-20) planes. This along with a decrease in peak intensity and an increase in peak broadening shows that the photoassisted method has modified the thin film crystallinity reducing grain size and increasing the number of grain orientations

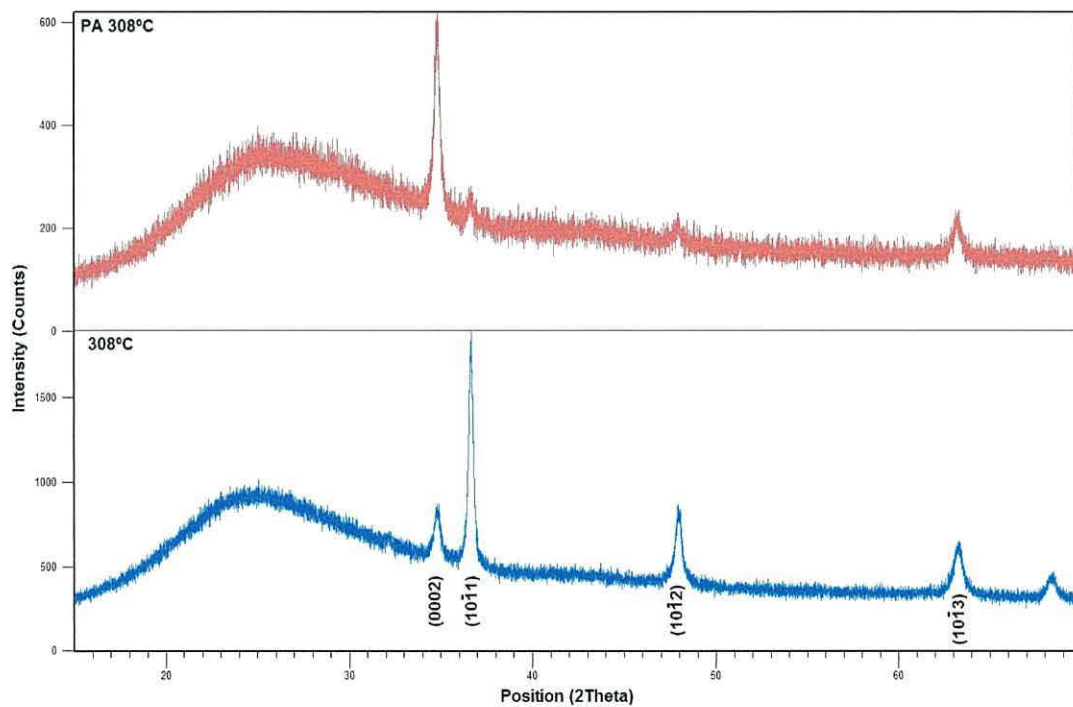


Fig 5.5.10 Intensity (counts) versus 2θ for ZnO thin films deposited at II/VI ratio = 3 and substrate temperature of 308°C . The top spectra was deposited under photoassisted conditions of UV/Vis lamp power at substrate of 23.6 mW/cm^2 .

Figure 5.5.11. compares the average grain size (nm) of pyrolytic and photoassisted films at different substrate temperatures. There is no significant difference in grain

size at 219 and 308°C, however at 67°C there is almost a 2 fold increase in grain size. The AFM images of these films are shown in figure 5.5.12.

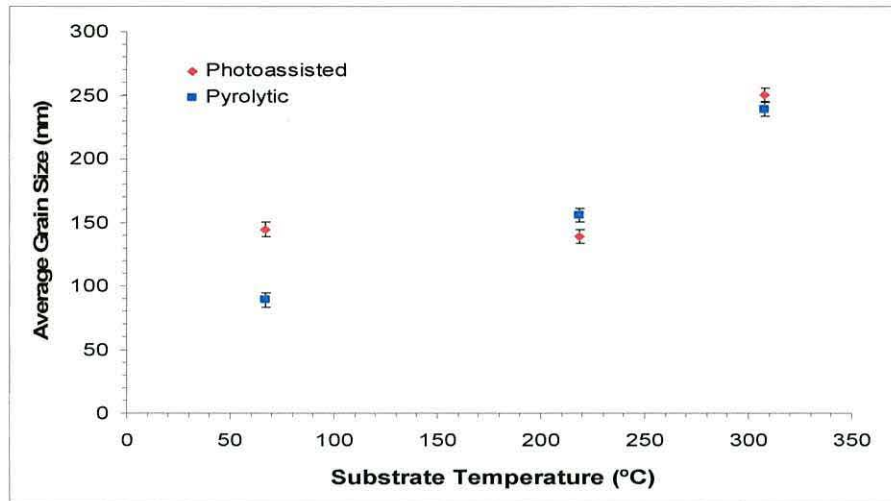


Fig. 5.5.11 Average grain size (nm) versus substrate temperature (°C) for both photoassisted and purely pyrolytically grown films. All films deposited at II/VI = 3. UV/Vis lamp power at substrate 23.6 mW/cm².

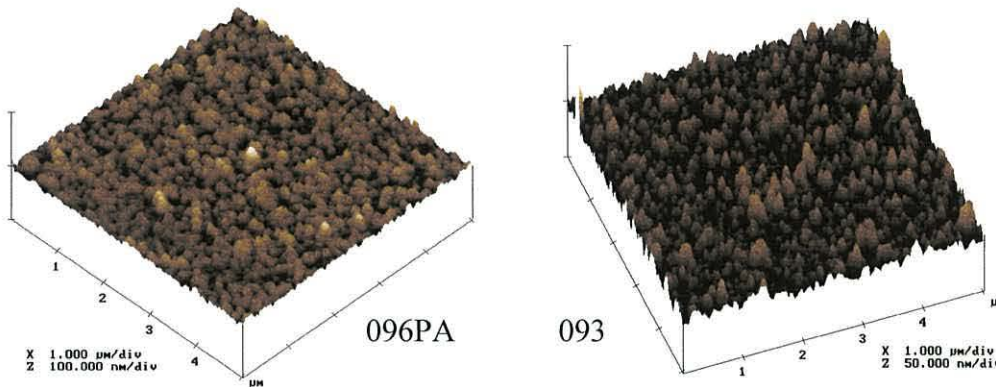


Fig. 5.5.12. AFM images of 096PA and 093 deposited at 67°C and II/VI = 3. The UV/Vis lamp power at substrate for 096PA was 23.6 mW/cm².

When considering photoassisted MOCVD of ZnO (see chapter 2.11) there have been no significant reports of enhanced growth rate in the literature. In all cases no attempt has been made to filter the light source, from wavelengths inducing gas-phase photolysis of the precursors. As discussed in chapter 3.5, the photoassisted experiments carried out in this research were, through the use of a filter, designed only to irradiate with ZnO band gap energy or below. Along with this, any photo-

thermal energy raising the substrate temperature by irradiation was negligible. These facts negated any possibility of the effects, observed in the photoassisted experiments, resulting from photolysis or photo-thermal effects. Therefore the changes observed in bandgap, resistivity and grain orientation when employing photoassisted growth may be surmised to be resulting from a surface photo-catalytic reaction.

5.5.3 Substrate Surface

As stated in chapter 3.5 the choice and preparation of substrate material is essential in thin film deposition. The substrates used for these ZnO thin films were aluminosilicate glass prepared by; cutting to size, ultra sonic agitation in deionized water, rinsing with methanol and drying with nitrogen. The SEM images shown in figure 5.5.13 demonstrate the effectiveness of this cleaning procedure.

The left hand image is an unprepared substrate having a greasy film and particulate matter covering the surface. The right hand image is that of a prepared substrate, the greasy film and most of the particulate matter has been removed by the cleaning process. The ‘archipelago like’ particles on the bottom right corner are evidence of a drying mark and a more thorough rinsing procedure was employed to overcome this effect.

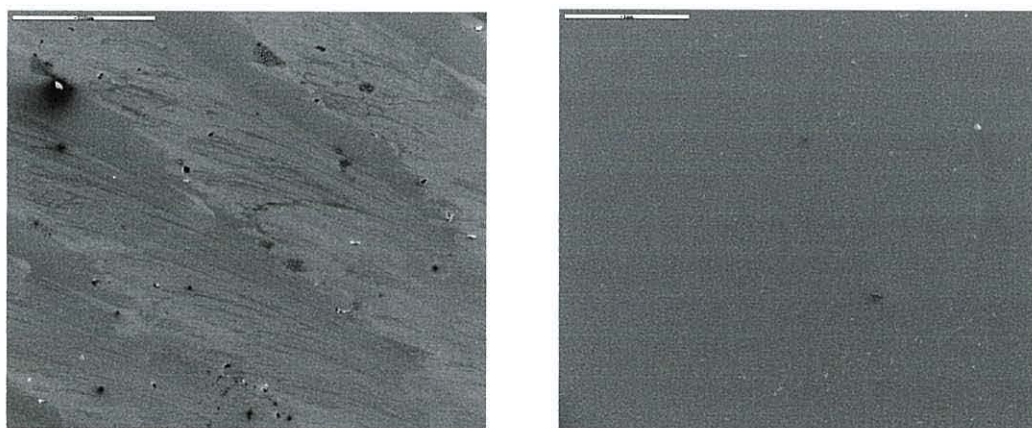


Fig. 5.5.13 SEM images of gold coated aluminosilicate substrate. Left hand image is unprepared substrate scale bar = 500 μm . Right hand image is prepared substrate scale bar = 1000 μm .

5.5.4 EDAX of ZnO

The EDAX spectra shown in figure 5.5.14 and 5.5.15 give qualitative information on elemental composition. In figure 5.5.14 the zinc and oxygen peaks of the ZnO film are observed along with small aluminium and silicon peaks arising from the substrate.

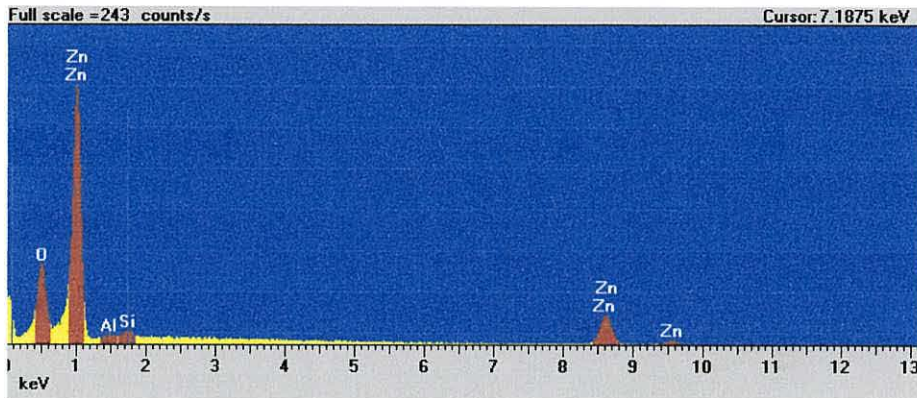


Fig. 5.5.14 EDAX spectrum of 1.2 μm thick ZnO thin film deposited at substrate temperature of 219°C and II/VI ratio = 4.

The zinc and oxygen peaks of the ZnO film are again observed in figure 5.5.15 however, the aluminium and silicon peaks are more intense. There are also calcium and barium peaks which probably derive from the substrate. The influence of the substrates elemental composition is more apparent in figure 5.5.15 due to the film being thinner. The electron beam penetrates further into the thinner film revealing more of the substrate elements in the EDAX spectrum.

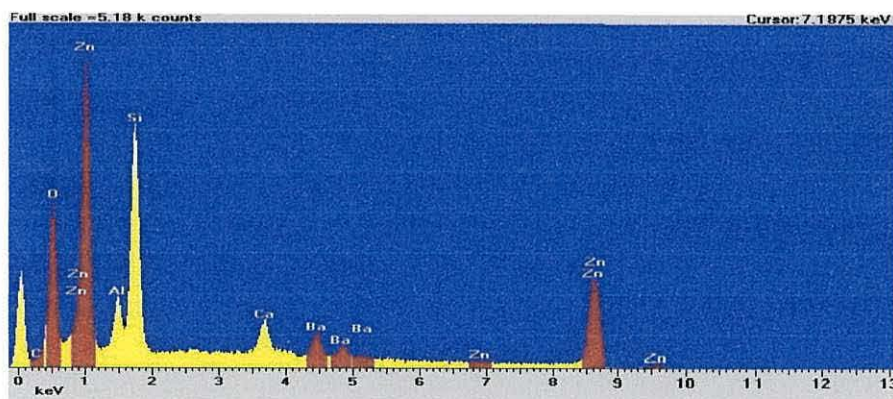


Fig. 5.5.15. EDAX spectrum of 0.5 μm thick ZnO film deposited at substrate temperature of 276°C and II/VI ratio = 3.

5.6 References

- [1] M. R. Leys, *Chemtronics* **2** (1987) 155-16.
- [2] V. Sallet, C. Thiandoume, J. F. Rommeluere, A. Lusson, A. Riviere, J. P. Riviere, O. Gorochoy, R. Triboulet and V. Munoz-Sanjose, *Mat. Letters* **53** (2002) 126-131
- [3] S. Oda, H. Tokunaga, N. Kitajama, J. Hanna, I. Shimizu and H. Kokado, *Jap. J. App. Phys.* **24**, 12, (1985) 1607-1610.
- [4] B. Hahn, G. Heindel, E. Pschorr-Schoberer and W. Gebhardt, *Semicond. Sci. Technol* **13** (1998) 788-791.
- [5] C. Kirchner, T. Gruber, F. Reuss, K. Thonke, A. Wang, C. Giessen and M. Heuken, *J. Cryst. Growth* **248** (2003) 20-24.
- [6] G. E. Coates and D. Ridley, *J. Chem. Soc.* (1965) 1870-1877
- [7] J. Auld, D. J. Houlton, A. C. Jones, S. A. Rushworth, M. A. Malik, P. O'Brien and G. W. Critchlow, *J. Mater. Chem* **4** (1994) 1249-1253
- [8] E. C. Ashby, G. F. Willard and A. B. Goel, *J. Org. Chem.* **44** (1979) 1221-1232.
- [9] J. Kim, K. Kim and K. Yong, *J. Vac. Sci. Technol. A* **29**(5) (2002) 1582-1586.
- [10] S. Fujita, A. Tanbe, T. Sakamoto, M. Isemura and S. Fujita, *J. Cryst. Growth* **93** (1988) 259.
- [11] S. J. C. Irvine, M. U. Ahmed and P. Prete, *J. Electron. Mater* **27** (1998) 763.
- [12] M. U. Ahmed and S. J. C. Irvine, *J. Elect. Mat.* **29** (2000) 169-172.
- [13] N. Oleynik, M. Adam, A. Krtshil, A. Dadgar, F. Bertram, D. Forster, A. Diez, A. Greiling, M. Seip, J. Christen and A. Krost, *J. Cryst. Growth* **248** (2003) 14-19.
- [14] W. W. Wenas, A. Yamada and K. Takahashi, *J. Applied Phys.* **70** (1991) 7119-7123.
- [15] D. C. Look, J. W. Hemsky and J. R. Sizelove, *Phys. Rev. Lett.* **82** (1999) 2552.
- [16] A. F. Kohan, G. Ceder, D. Morgan and C. G. van de walle, *Phys. Rev. B* **61**, (2000) 15019.
- [17] C. G. Van de Walle, *Phys. Rev. Lett.* **85** (2000) 1012.
- [18] S. F. J. Cox, E. A. Davis, S. P. Cottrell, P. J. C. King, J. S. Lord, J. M. Gil, H. V. Alberto, R. C. Vilao, J. Piroto Duarte, N. Ayres de Campos, A. Weidinger, R. L. Lichti and S. J. C. Irvine, *Phys. Rev. Lett.* **86** (2000) 2601.
- [19] Y. Natsume, H. Sakata and T. Hirayama, *Phys. Stat. Sol.*, **148** (1995) 485
- [20] W. Frammelsberger, R. Geyer, P. Lechner, H. Rubel and H. Schade, 16th European Photovoltaic Solar Energy Conference, (1-5 May 2000) 389-392.

Chapter Six: Conclusions

6.1 Introduction

This chapter surmises all the major findings of the research. The opportunities for further experimental work are discussed, along with analysis techniques that would elucidate further some of the thin film properties.

6.2 Conclusions

A research level MOCVD system was designed and built and ZnO thin films were successfully deposited using DEZn and a previously unreported oxygen precursor n-BuOH. No prereaction was observed using these precursors. The n-BuOH precursor was suggested to be a viable alternative to the more commonly used alcohol t-BuOH having the process-simplifying advantage of being liquid at room temperature. The study carried out in this thesis, using n-BuOH, adds to a growing body of evidence that alcohol precursors offer multiple advantages, over conventional oxygen precursors, for ZnO deposition.

The films deposited were found to be non-uniform and a wedge shape profile was identified. This profile was ascribed to the fact that the substrate was non-rotating leading to a precursor concentration gradient from the inlet side to the exhaust side.

The growth rates were measured using *in situ* interferometry and found to be II/VI ratio dependant as well as temperature dependant. ZnO thin films were deposited at temperatures as low as 67°C. Depositing a polycrystalline thin film of ZnO at these low temperatures will allow the possibility of using flexible substrates, such as plastics, opening up new opportunities in device application.

The growth kinetics under different precursor partial pressure ratios was studied. It was found that increasing the II/VI ratio led to a pseudo-first order growth rate model and, increasing VI/II ratio resulted in a decrease in growth rate. The optimum growth rate temperature for both II/VI = 1 and 3 was found to be 240°C.

A rate equation was proposed which identifies two rate constants; the first, k_A a slow step that relates to the decomposition of the alkylzinc alkoxide via a radical mechanism, and the second faster step k_B that occurs under higher than equimolar II/VI ratios. The mechanism proposed in the second step identifies mono-ethylzinc radicals, physisorbed on the surface, as initiators for the decomposition of the alkylzinc alkoxide. It is proposed that when deposition takes place at above equimolar VI/II ratios excess n-BuOH acts as a site blocking molecule lowering the thin film growth rate.

The nucleation delay in film growth was measured via *in situ* interferometry. This delay was found to be non-substrate temperature dependant but did decrease two fold when moving from equimolar partial pressures to zinc rich conditions. This factor was attributed to an increased selectivity of adsorption sites when the slower reaction rate k_A dominated.

A rapid change in surface morphology was noted between macro-smooth, below 260°C, to a rough rough film above 260°C. Control of this change in surface morphology will be of great benefit for the α -Si and CIGS photovoltaic systems where a rough TCO layer is desirable. The average transmission in the visible wavelengths for the macro-smooth films was shown to be above 90%. From the transmission data a generally, well defined and sharp absorption edge was shown to begin at around 360 nm. The films generally displayed high transmission of wavelengths from 360 nm and through the visible spectrum, allowing a large range of energy (3.3 eV or lower) through to a *p-n* junction.

The grain size, for zinc rich conditions, as measured by AFM was shown to increase 2 fold when moving from the macro-smooth to rough-rough surface morphology, at around 260°C. Supporting this, the XRD results identified a shift in dominant grain orientation in the same temperature region.

For zinc rich conditions a shift to lower bandgap energies was observed as deposition temperature increased indicating the possibility of a change in stoichiometry within the thin film. The resistivities of the films grown under zinc rich conditions decreased significantly when moving to high deposition temperatures, the best value being $6 \times 10^{-3} \Omega \text{ cm}$ at 308°C . These two factors indicate a change in the electrically active effects, when growth is governed by the k_B rate constant, of the films with substrate temperature.

When depositing ZnO under equimolar conditions, where the slower k_A rate constant dominated, no change in bandgap or resistivity was found. The resistivities of the films were generally too high for TCO applications, high resistivities are expected for ZnO deposited without electrically active dopants.

The previously unreported use of, ZnO bandgap energy specific, UV irradiation designed to stimulate a photo-catalytic reaction in the growing film was studied. The photoassisted results showed no improvement in growth rates or surface morphology. However when operating at the highest power setting available (36.8 mW/cm^2), in zinc rich conditions and in the high temperature regime (308°C), a significant change in bandgap and resistivity was noted. The bandgap shifted from 3.24 eV non-photoassisted to 3.37 eV photoassisted and the resistivity increased from 6.0×10^{-3} to $1.5 \times 10^{-2} \Omega \text{ cm}$. This indicates that the UV irradiation is acting to suppress the change in stoichiometry, identified as being responsible for the decrease in both bandgap energy and resistivity, when following the k_B dominated reaction pathway.

7.3 Further work

There are a number of areas that could benefit from further research these include; modifications to the MOCVD apparatus to give a wider variation in temperatures, precursor ratios, UV/Vis lamp intensity and doping capability. A capability, to utilise a wider range of measurement techniques would help to clarify further some of the mechanisms leading to the thin film properties observed. Improvements in

the uniformity of the thin films could be made by modifying the reaction tube and studying the flow dynamics of the carrier gas.

The deposition temperatures under which the thin films were grown was limited by the resistance heater to a maximum of around 330°C. Thus it was not possible to explore the deposition characteristics and thin film properties at high temperatures. Also a large proportion of experimental time was taken up in heating the substrate to a uniform temperature. An improvement to the range and speed of temperature control could be made by heating via an infrared lamp. The range of precursor ratios were also limited by the capacity of the MFCs (sccm) and the control of vapour pressure within the bubblers. Placing the bubblers in temperature controlled chiller units would have allowed adjustment of the precursor vapour pressure and hence a wider range of ratios to be studied.

For both the non-photoassisted and photoassisted thin film deposition the study of different carrier gases could help elucidate the reaction mechanisms. In the case of the photoassisted work the use of a hydrogen carrier gas may, via hydrogen radicals, give results similar to those in the ZnSe systems discussed in chapter 2.11.

A change in the photoassisted experiments was observed when moving from 23.6 mW/cm² to the maximum available 36.8 mW/cm². Further experiments using higher power, and possibly shorter wavelength, irradiation (as discussed in chapter 2.10) may result in further photoassisted thin film modifications.

The introduction of a third precursor line to the MOCVD system would allow doping of the ZnO thin film. This further work on improving the electrical properties would allow the already; low temperature, high transparency films to be incorporated into photovoltaic devices.

Further investigation into different alcohol precursors and their effects on growth rates and film properties will lead to an additional understanding of the chemistry

behind the ZnO MOCVD technique. The use of mass spectrum analysis of reactor exhaust gases along with isotopic labeling of precursor moieties has been identified as future work for elucidating growth rate mechanisms.

Photoluminescence measurements, identifying vacancies belonging to either zinc or oxygen, may allow the zinc/oxygen stoichiometry within the thin film to be recognized, thus providing a correlation with the observed change in bandgap energy. In addition, precision lattice parameter measurements using XRD may indicate changes in lattice strain with change in composition. A correlation would give sustenance to the argument put forward in chapter 5.4. that the change in bandgap with deposition temperature is related to changes of zinc/oxygen stoichiometry.

Further work, utilizing the growth kinetics and related thin film properties identified within this thesis may include the study of; alloys of ZnO incorporating Sn, ZnO nanorods and ZnO based photodetectors among others.

Appendix



Growth properties of thin film ZnO deposited by MOCVD with *n*-butyl alcohol as the oxygen precursor

D.A. Lamb, S.J.C. Irvine*

Department of Chemistry, University of Wales, Bangor, Gwynedd LL57 2UW, UK

Received 17 May 2004; accepted 27 August 2004

Communicated by J.B. Mullin

Abstract

A study of the deposition of thin film ZnO from diethylzinc (DEZn) and a novel oxygen precursor *n*-butanol (*n*-BuOH), using atmospheric metal organic chemical vapour deposition (MOCVD), has been carried out. The purpose-built MOCVD reactor incorporated in situ monitoring of the thin film growth via interferometry. Growth rates of up to 0.6 nm/s were achieved at temperatures below 250 °C and precursor ratio II/VI = 4. The II/VI precursor ratio was found to strongly influence the growth rate of the zinc oxide films. At low ratios the growth rate was slow and increased linearly as the ratio increased. Increasing the *n*-BuOH to DEZn ratio had the opposite effect and acted to suppress the growth rate. The films showed high optical transparencies when deposited at temperatures below 250 °C and displayed high electrical resistance.

© 2004 Elsevier B.V. All rights reserved.

PACS: 68.55.Ac; 68.55.Jk; 68.60.Wm; 68.47.Gh; 68.37.Ps

Keywords: A1. Crystal morphology; A3. Metalorganic chemical vapor deposition; B1. Oxides; B1. Zinc compounds; B2. Semiconducting II–VI materials; B3. Solar cells

1. Introduction

ZnO is a wide bandgap (3.4 eV) n-type II–VI semiconductor and has recently attracted much attention because of its wide applications for

various optoelectronic devices. Many groups have reported highly conductive optically transparent ZnO thin films deposited by techniques such as metal organic chemical vapour deposition (MOCVD) [1–3], sputtering [4], spray pyrolysis [5], sol–gel [6] and electrodeposition [7]. In the MOCVD of ZnO dimethylzinc (DMZn) and diethylzinc (DEZn) are the most commonly used zinc sources with some

*Corresponding author. Tel.: +44-1248-382383; fax: +44-1248-370528.

E-mail address: sjc.irvine@bangor.ac.uk (S.J.C. Irvine).

attention now being focused on single source precursors [8].

These organometallics have traditionally been pyrolysed in the presence of oxygen precursors such as H_2O and O_2 . However, severe premature reactions invariably occur and, the use of less reactive oxygen sources including CO_2 , N_2O [9] and oxygen containing heterocycles [10] have been investigated. This paper follows the approach first employed by Oda et al. [11], who proposed alcohols as more controlled oxidizing agents. Oda et al. [11] deposited ZnO thin films using DEZn with methanol, ethanol, tertiary butanol and H_2O (as a standard) using low pressure MOCVD.

It was shown that of the three alcohols tertiary butanol provided defect-free and highly oriented films. In response to this Hahn et al. [12] applied tertiary butanol and DMZn at atmospheric pressure to deposit ZnO thin films and reported that no premature reactions were observed. The Cl-doped films deposited had resistivities as low as $7.6 \times 10^{-4} \Omega/\text{cm}$ with an electron mobility of $60 \text{ cm}^2 (\text{V/s})$. More recently Sallet et al. [13] successfully applied the tertiary butanol approach to atmospheric pressure MOCVD of ZnO onto sapphire (0001) substrates.

In this paper, ZnO thin films were deposited onto glass substrates by atmospheric pressure MOCVD using DEZn and a previously unreported oxygen precursor for this application *n*-butyl alcohol ($\text{C}_4\text{H}_9\text{OH}$). *t*-BuOH with its melting point of 26°C requires a heated bubbler and lines to maintain the liquid phase needed for vapour transport to the reaction zone. *n*-BuOH, an isomer of *t*-BuOH, is a liquid at room temperature and so avoids the need for heated bubbler and lines. Therefore, *n*-BuOH could be a more attractive precursor than *t*-BuOH for applications such as transparent conducting oxides (TCOs) for solar cells. The deposition rates of the thin films were studied using in situ laser interferometry.

2. Experimental procedure

ZnO thin films have been deposited at atmospheric pressure in a purpose-built horizontal

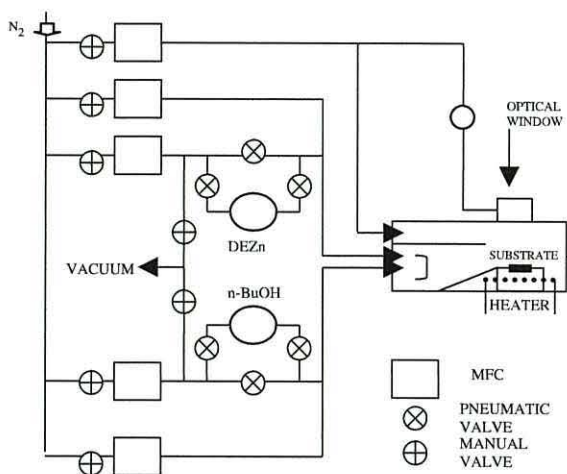


Fig. 1. Schematic diagram of the MOCVD apparatus.

single-wafer MOCVD reactor. Fig. 1 shows a schematic of the deposition system. Diethylzinc and *n*-butanol were used respectively as zinc and oxygen sources, contained in bubblers, the DEZn being kept at 0°C and the *n*-BuOH at room temperature, 20°C . The carrier gas used was high purity nitrogen. The substrate was heated by a resistance heater and temperature controlled by a thermocouple located in a graphite susceptor. Due to the thermocouples location, within the susceptor, there was an uncertainty as to the actual temperature at the substrate surface.

An experiment to measure actual substrate temperature was carried out by measuring the melting points of two metals on the substrate. Using the room temperature as a third point of reference it was possible to produce a calibration curve of the actual substrate surface temperature versus the thermocouple temperature. All temperatures quoted have been corrected using this calibration curve.

The amount of DEZn and *n*-BuOH transported to the reactor was set by controlling the flow rates of the carrier gas through the bubblers. The zinc oxide was deposited onto Corning 1737 aluminosilicate glass substrates; ultra-sonically cleaned in deionised water before being rinsed with methanol and dried with nitrogen.

The growth rates were calculated by in situ laser interferometry employing a 635 nm diode laser.

Surface morphology and grain size were analysed by scanning electron microscopy (SEM) and atomic force microscopy (AFM). The transmission and absorption spectra were performed on a ATI UNICAM UV/Vis spectrometer scanning between 190 and 900 nm.

3. Results and discussion

3.1. Growth results and mechanisms

The deposition rate as a function of substrate temperature for two different II/VI ratios is shown in Fig. 2. No prereaction was observed over these deposition temperatures. For both II/VI ratios the growth rate steadily increases with increasing temperature reaching a maximum around 240 °C. This increase in growth rate is attributed to the decomposition of the precursors being thermally activated. Above 240 °C the growth rate decreases rapidly possibly as a result of thermal cracking of precursors before reaching the reaction zone or desorption of unreacted precursors. For II/VI = 1 the growth rates are seen to be approximately 5 times lower than II/VI = 3 but following the same general trend.

Fig. 3a shows the growth rate of the ZnO films as a function of the partial pressure of DEZn when *n*-BuOH partial pressure was fixed over three different substrate temperatures. At all three temperatures an increase in DEZn concen-

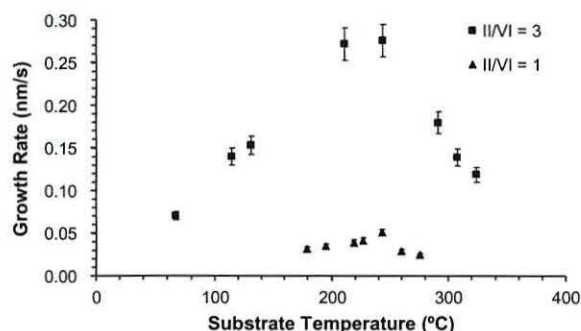


Fig. 2. Growth rate ($\mu\text{m/h}$) as a function of substrate temperature ($^{\circ}\text{C}$) for ZnO thin films deposited at II/VI = 3 and 1.

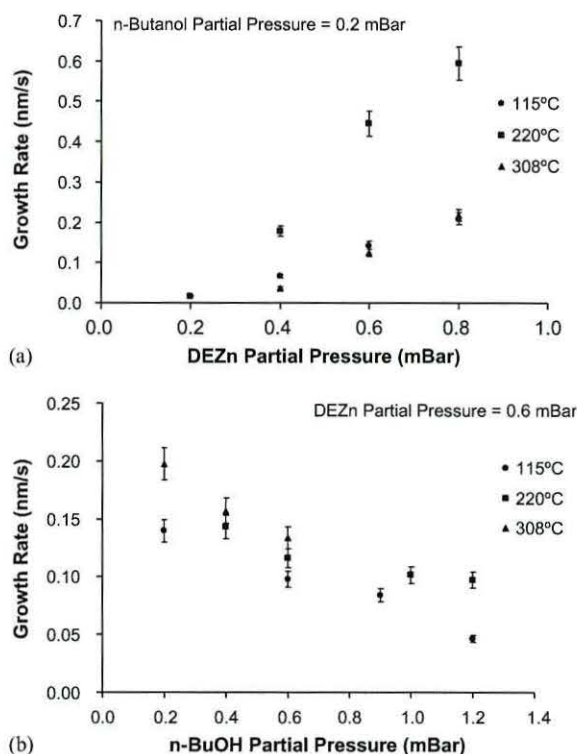


Fig. 3. (a) Growth rate (nm/s) versus DEZn partial pressure (mBar) with *n*-BuOH fixed at 0.2 mBar substrate temperature 270 °C. (b) Growth rate (nm/s) versus *n*-BuOH partial pressure (mBar) with DEZn fixed at 0.2 mBar substrate temperature 270 °C.

tration, whilst maintaining a constant *n*-BuOH concentration, leads to a linear increase in growth rate (above the II/VI = 1 ratio). This is in marked difference to Fig. 3b which shows that increasing the *n*-BuOH concentration whilst maintaining a constant DEZn concentration leads to a decrease in the growth rate for both the low and high temperature regimes.

From work by Coates and Ridley [14] it is known that when DMZn and R-OH are mixed the result is the formation of an alkylzinc alkoxide with little displacement of the second alkyl group. Furthermore this alkylzinc alkoxide was also shown to exist as a tetrameric oligomer. Auld et al. [8] proved that the alkylzinc alkoxide ($\text{MeZn}(\text{O}i\text{Bu})$) proved sufficiently volatile to be used as a single source precursor for the growth of ZnO

by MOCVD. Auld et al. [8] stated that the $\text{MeZn}(\text{OBu}^t)$ 'is decomposed into ZnO either in the hot boundary layer above the substrate, or more likely, during heterogeneous pyrolysis of the alkylzinc alkoxide on the substrate surface'. The decomposition of this alkylzinc alkoxide 'active precursor' follows a cyclic six-centred transition state shown in Fig. 4 [15]. The ZnO thin film is formed on the surface when a β -hydrogen of the alkoxy moiety is abstracted by the methyl group of the zinc.

However, the cyclic arrangement of the n -BuOH alkoxide is not known and may not lead to such an easy decomposition path as for the t -BuOH oligomer. The lack of premature reaction in the mixer and entrance region of the reactor would support that the $\text{EtZn}(n\text{-BuOH})$ does not readily decompose. This is supported by the kinetic results in Fig. 3a which show very low growth rates for low concentrations of DEZn. It is only when concentrations of DEZn exceed those of the n -BuOH that higher growth rates are achieved. It is likely that excess DEZn will dissociatively adsorb on the surface, releasing ethyl radicals that can assist in the decomposition of the surface alkoxide.

The results in Fig. 3a demonstrate that at these temperatures the kinetics are pseudo-first order with respect to DEZn partial pressure, i.e. the linear rate dependence on concentration does not go through the origin but is offset by the concentration of the n -BuOH (0.2 mBar). When DEZn partial pressure moves below 0.2 mBar (where $\text{II}/\text{VI}=1$) the growth rate decreases more slowly. The rate equation (1) describes the growth rate data for ZnO from Fig. 3a where; $[\text{EtZn}(\text{O-Bu}^n)]$ is the concentration of alkylzinc alkoxide and $[\text{DEZn}] - [n\text{-BuOH}]$ represents an excess of

DEZn (above the $\text{II}/\text{VI}=1$ ratio).

$$\text{Growth rate} = k_A[\text{EtZn}(\text{OBu}^n)] + k_B([\text{DEZn}] - [n\text{-BuOH}]), \quad (1)$$

where $k_A \ll k_B$.

This kinetic expression can lead to speculation about alternative and competitive reaction mechanisms in the formation of the ZnO film from these precursors. Details of the structure of the alkoxide and possible decomposition paths are not known but the evidence from the growth rate kinetic data is that this must be slow. A comparison also needs to be made with the decomposition of the t -BuOH alkoxide where the mechanism may be different. It is also important to know something of the possible radical reactions on the surface and whether ethyl radicals or the monoethylzinc are the active intermediates. From the growth rate kinetic data it is clear that this must be a fast step. Further work is being carried out on comparing the detailed kinetics with t -BuOH as the oxygen source and in mass spectrometer analysis of the exhaust gases to gain further evidence based on the stable reaction products.

Fig. 3b shows the effects on growth rate when moving from zinc rich conditions to alcohol rich conditions. It should be noted that the equimolar portion of the graph occurs at an n -BuOH partial pressure of 0.6 mBar in this case. From Fig. 3a it was seen that the growth rate of ZnO was extremely low at DEZn/ n -BuOH partial pressures of 0.2 mBar. Therefore for the investigation into high VI/II ratios the partial pressure of the DEZn was fixed at 0.6 mBar enabling reasonable growth rates for data collection.

Taking the above into context the first section of the graph in Fig. 3b, n -BuOH partial pressure 0.2–0.6 mBar, represents moving from zinc rich to

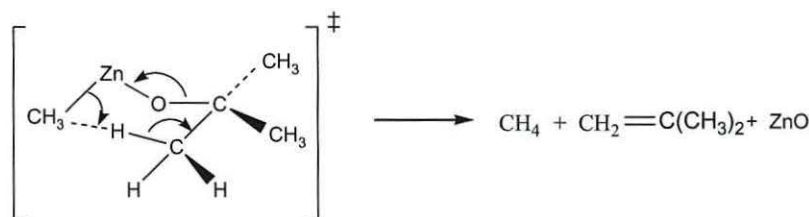


Fig. 4. Cyclic six-centre transition state for $\text{MeZn}(\text{OBu}^t)$ alkylzinc alkoxide. After E.C. Ashby et al. (1979) [15].

equimolar conditions. This may be treated as a different experiment to Fig. 3a as it is the DEZn partial pressure that remains fixed throughout. However, the behavior of this section of the graph is similar to that seen in Fig. 3a where the growth rate increases with increasing II/VI ratio, thus supporting the proposed surface radical mechanism. The alcohol rich conditions occur where the *n*-BuOH partial pressure moves from 0.6 to 1.2 mBar. In this part of the graph, for the maximum growth rate at a temperature of 220 °C, the growth rate decreases initially, appearing to level out at the highest VI/II ratio. In the lower growth rate regime 115 °C the growth rate decreases more rapidly as the VI/II ratio increases.

The suppression of the growth rate, when moving to higher VI/II values, could be explained by surface site blocking by the excess *n*-BuOH in a Langmuir–Hinshelwood type mechanism. This argument may be supported by the evidence in Fig. 3a that at the lower temperature (115 °C), where the *n*-butanol will be more strongly adsorbed, the reduction in growth rate is the greatest. Whereas, at the higher temperature (220 °C), where site blocking would be less effective due to increased thermal energy, there is little or no reduction in growth rate.

Evidence for this site blocking by the excess alcohol is given by Kim et al. [16], who reported that isopropanol chemisorbed into isopropoxy and atomic hydrogen on the surface of Si (100) between 277 and 377 °C. *n*-BuOH could reasonably be expected to behave in a similar manner on the aluminosilicate substrates used in this research. If the *n*-BuOH was preferentially adsorbed, over the alkylzinc alkoxide, onto the substrate it would block sites on the substrate surface. The rate of reaction would then be determined by how many sites were available for the alkylzinc alkoxide to adsorb onto the substrate and further decompose to ZnO. Therefore, the higher the partial pressure of *n*-BuOH at the substrate surface, the lower the likelihood of the alkylzinc alkoxide finding a free surface site and hence the lower the growth rate. Further work is planned to investigate the *t*-BuOH/DEZn by the same approach undertaken with *n*-BuOH.

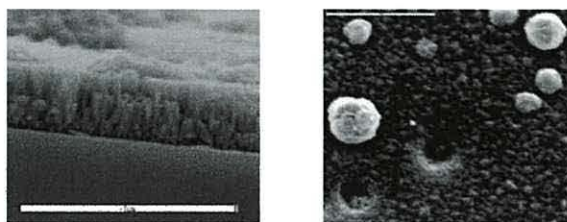


Fig. 5. SEM images of ZnO thin films deposited at 220 °C and II/VI=4. The cross-section of the cleaved film shows a columnar grain structure. The top view shows macro-structures and holes in the film. Scale bars = 5 μm.

3.2. ZnO film characterisation

Fig. 5 shows SEM images of a ZnO film (1.5 μm thick) grown with DEZn and *n*-BuOH on a glass substrate at 220 °C. In the cross-sectional image on the left an observed columnar structure normal to the substrate indicates *c*-axis orientation of the film. The right-hand image shows the surface of the same ZnO film with an average grain size of 250 nm.

The large macro-structures and holes distributed across the film may be further evidence of the surface catalysed growth mechanism whereby morphological defects and impurities on the substrate surface not removed during preparation have acted as preferential nucleation sites leading to a faster growth rate than the rest of the film. The holes may be explained in the same manner whereby impurities on the substrate surface have inhibited the growth of the ZnO.

There is a change in surface morphology of the thin films at temperatures above approximately 260 °C. AFM images demonstrating this change are shown in Fig. 6 where films below 260 °C have a macro-smooth appearance and, those above 260 °C have a much rougher appearance. This change in surface morphology is also demonstrated in Fig. 7 where RMS roughness (nm) is plotted against substrate temperature for precursor ratios II/VI=3. There is little change in RMS roughness below 243 °C with a fourfold increase in surface roughness above 260 °C. These factors indicate a change in preferred orientation of the films with substrate temperature. Further analysis is planned using XRD to resolve these findings.

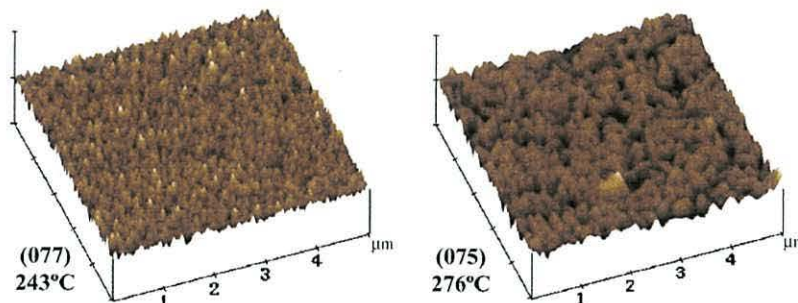


Fig. 6. AFM images of sample 077-smooth (243 °C) and 075-textured (276 °C). Both deposited at II/VI = 3 both 500 nm thick. Scale $5 \mu\text{m}^2$.

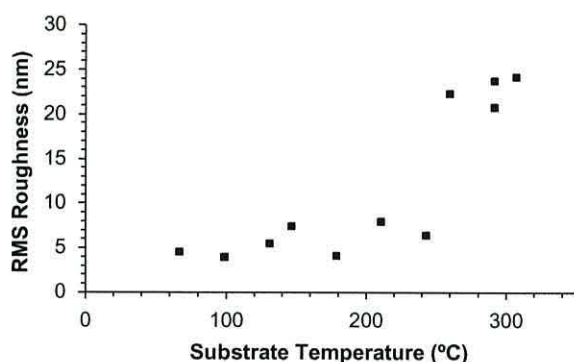


Fig. 7. ZnO film RMS roughness (nm) versus substrate temperature (°C) from AFM studies of samples deposited at II/VI = 3, on glass substrates.

The transmission spectra of films obtained for II/VI = 3 and different substrate temperatures is shown in Fig. 8. The spectra are typical of thin film ZnO where the transparency in visible wavelengths is high and the absorption edge, arising from energy absorbed by the thin films bandgap, is around 360 nm (3.3 eV). The absorption edge is very sharp for the low-temperature films allowing high transmission of wavelengths above 380 nm. The bandgap energies for the same samples are shown in the insert, Fig. 8, where a plot of $(\alpha h\nu)^2$ versus $(h\nu)$ and the extrapolation of the linear portion of this curve to zero absorption coefficient provides the E_g energy (eV).

The optical gap is around 3.4 eV for a substrate temperature of 67 °C and II/IV = 3 this value is in line with the standard literature ZnO bandgap. The bandgap is shown in Fig. 8 to decrease as the substrate temperature increases. This effect may be

due to a change in stoichiometry between zinc and oxygen as a result of the substrate temperature increase. This shift in bandgap with substrate temperature is not observed when II/VI = 1. Further studies into stoichiometry of the films will hopefully clarify these results.

4. Conclusion

ZnO was successfully deposited using DEZn and *n*-BuOH at atmospheric pressure in a purpose-built MOCVD system. No prereaction was observed using these precursors. The growth rates were measured using in situ interferometry and found to be II/VI ratio-dependant as well as temperature-dependant. Increasing II/VI ratio led to a pseudo-first-order growth rate model, increasing VI/II ratio resulted in a decrease in growth rate. The optimum growth rate temperature for both II/VI = 1 and 3 was found to be 240 °C.

A rate equation has been proposed which identifies two rate constants; the first, k_A a slow step that relates to the decomposition of the alkylzinc alkoxide, and the second faster step k_B that occurs under higher than equimolar II/VI ratios. For the mechanism proposed in the second step it is suggested that radicals released from DEZn, physisorbed on the surface, act as initiators for the decomposition of the adsorbed alkylzinc alkoxide. It is proposed that when deposition takes place at above equimolar VI/II ratios excess *n*-BuOH acts as a site blocking molecule, according to a Langmuir–Hinshelwood mechanism, lowering the thin film growth rate.

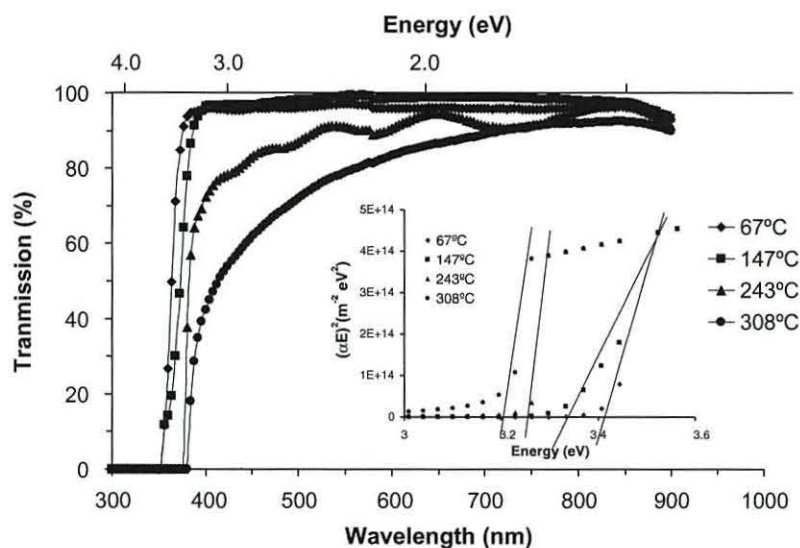


Fig. 8. Transmission (%) as a function of wavelength (nm) for ZnO thin film samples deposited at different substrate temperatures and $\text{II}/\text{VI}=3$. All films were 500 nm thick. Insert plot of $(\alpha/h\nu)^2$ as a function of $h\nu$ (eV) for the same ZnO samples.

A rapid change in surface morphology was noted between macro-smooth, below 260 °C, to a rough textured film above 260 °C. The average transmission in the visible wavelengths for the macro-smooth films was shown to be above 90%. A shift to lower bandgap energies was observed as deposition temperature increased indicating the possibility of a change in stoichiometry within the thin film. The conductivities of the films were generally low; further work to improve the electrical properties including doping may allow these low temperature, high transparency, films to find applications such as TCOs for solar cells.

Acknowledgements

The authors wish to gratefully acknowledge the financial support of the Engineering and Physical Sciences Research Council (EPSRC). We are indebted to the technical staff of UWB; Steve Jones, Mike Lewis and John Cambridge. We thankfully acknowledge the assistance given by the late John Sambrook who will be greatly missed.

References

- [1] S. Oda, H. Tokunaga, N. Kitajama, J. Hanna, I. Shimizu, H. Kokado, *Jpn. J. Appl. Phys.* 24 (12) (1985) 1607–1610.
- [2] M. Yoshino, W.W. Wenas, A. Yamada, M. Konagai, K. Takahashi, *Jpn. J. Appl. Phys.* 32 (1993) 726–730.
- [3] S.Y. Myong, S.J. Baik, C.H. Lee, W.Y. Cho, K.S. Lim, *Jpn. J. Appl. Phys.* 36 (1997) L1078–L1081.
- [4] J.F. Chang, M.H. Hon, *Thin Solid Films* 386 (2001) 79–86.
- [5] T.Y. Ma, S.S. Lee, *J. Mater. Sci.–Mater. Elec.* 11 (2000) 305–309.
- [6] Y.S. Choi, C.G. Lee, S.M. Cho, *Thin Solid Films* 289 (1996) 153–158.
- [7] E.A. Dalchiale, P. Giorgi, R.E. Marotti, F. Martin, J.R. Ramos-Barrado, R. Ayouchi, D. Leinen, *Sol. Energy Mater. Sol. Cells* 70 (2001) 245–254.
- [8] J. Auld, D.J. Houlton, A.C. Jones, S.A. Rushworth, M.A. Malik, P. O'Brien, G.W. Critchlow, *J. Mater. Chem.* 4 (1994) 1249–1253.
- [9] C.K. Lau, S.K. Tiku, K.M. Lakin, *J. Electrochem. Soc.* 127 (1980) 1843.
- [10] B.E. Warren, *X-ray Diffraction*, Addison-Wesley, Reading, MA, 1969.
- [11] S. Oda, H. Tokunaga, N. Kitajama, J. Hanna, I. Shimizu, H. Kokado, *Jpn. J. Appl. Phys.* 24 (12) (1985) 1607–1610.
- [12] B. Hahn, G. Heindel, E. Pschorr-Schoberer, W. Gebhardt, *Semicond. Sci. Technol.* 13 (1998) 788–791.
- [13] V. Sallet, J.F. Rommeluere, A. Lusson, A. Riviere, S. Fusil, O. Gorochov, R. Triboulet, *Phys. Stat. Sol.* 229 (2002) 903–906.
- [14] G.E. Coates, D. Ridley, *J. Chem. Soc.* 1965, 1870.
- [15] E.C. Ashby, G.F. Willard, A.B. Goel, *J. Org. Chem.* 44 (1979) 1221–1232.
- [16] J. Kim, K. Kim, K. Yong, *J. Vac. Sci. Technol. A* 29 (5) (2002) 1582–1586.